行政院國家科學委員會補助專題研究計畫成果報告

※ ※※※※※※※※※※※※※※※※※※※※※※※※※※※※※※※※

※　微機電技術製作之化學微推進系統之研究發展-子計畫四:應用光　※

※　　　　　　　診測技術研究微米燃燒室之流場特性　　　　　　　※

※　　　　　　　　　　　　　　　　　　　　　　　　　　　　　　※

※※※※※※※※※※※※※※※※※※※※※※※※※※※※※※※※※

計畫類別：□個別型計畫　　■整合型計畫
計畫編號：NSC90-2212-E-216-019, NSC91-2212-E-216-010, NSC92-2212-E-216-001
執行期間：90 年 08 月 01 日至 93 年 07 月 31 日

計畫主持人：鄭藏勝　教授
共同主持人：趙怡欽　教授、袁曉峰　副教授、呂宗行　助理教授
計畫參與人員：吳志勇、李約亨、陳志鵬、李國源、張智銘、張智國、
莫國笙、張維麟、蕭名傑

成果報告類型(依經費核定清單規定繳交)：□精簡報告■完整報告

本成果報告包括以下應繳交之附件：
□赴國外出差或研習心得報告一份
□赴大陸地區出差或研習心得報告一份
□出席國際學術會議心得報告及發表之論文各一份
□國際合作研究計畫國外研究報告書一份

處理方式：除產學合作研究計畫、提升產業技術及人才培育研究計畫、
列管計畫及下列情形者外，得立即公開查詢
□涉及專利或其他智慧財產權，□一年□二年後可公開查詢

執行單位：中華大學機械工程學系

中　華　民　國　93　年　10　月　31　日

中文摘要

本子計畫之主要研究內容乃是改良現有之紫外光拉曼散射及雷射誘發預解離螢光系統，使其具有更佳之空間解析度，以量測微管噴流火焰，進而瞭解觸媒微管及微型火焰之特性，作為研發微推進系統之參考。利用準分子雷射所誘發之自發振盪的拉曼散射與雷射誘發 OH 螢光量測技術，針對三種口徑(d = 0.2、0.48、1 mm)之氫氣擴散火焰，進行溫度及 O_2、N_2、H_2O、H_2、OH 組成份濃度的定量量測，以建立資料庫供燃燒理論模式比對用。除了實驗量測之外，本研究亦使用兩種不同化學反應模式進行數值模擬，第一種化學模式為 Miller 及 Bowman [39]所建議內含 9 個組成份及 20 個可逆反應步驟之氫–氧反應機制，第二種化學模式為 Gutheil 等人[29]所建議內含 9 個組成份與 21 個可逆反應步驟之氫氣–空氣化學反應模式。第一種化學模式用於管徑 1 mm、雷諾數 330 及 30 火焰之模擬，計算結果顯示，溫度及組成份濃度的預測與實驗數據非常接近，這也顯示 Miller 及 Bowman 之氫–氧化學反應機制可成功的預測一般層流擴散火焰。第二種化學模式用於管徑 0.2 及 0.48 mm、雷諾數 30 兩種火焰之模擬，計算結果顯示，溫度及組成份濃度的分布趨勢與實驗結果相似，但數值計算預測較寬的火焰及較高的溫度與 OH 濃度，此結果顯示數值模擬無法預測空氣捲入以致低估噴流中心之 O_2 及 N_2 濃度，同時使用的化學反應機制及簡化傳輸模式似乎無法正確模擬微型火焰。因此，在模擬微火焰時較輕組成份之熱擴散以及其他化學反應機制與傳輸資料或許必須加以考慮。

關鍵詞：微噴流火焰、拉曼散射、雷射誘發螢光、數值模擬

Abstract

The objective of this research is to improve the spatial resolution of UV Raman scattering and laser-induced predissociative fluorescence (LIPF) system for the study of microjet hydrogen diffusion flames. Non-intrusive, simultaneous, quantitative, point measurements of temperature, major species (O_2, N_2, H_2O, H_2) and OH concentrations are made in hydrogen diffusion flames produced from various diameter (d = 0.2, 0.48, and 1 mm) tubes. In addition to experimental measurements of the flames, numerical simulations are also performed to test chemical kinetic mechanisms. Two types of reaction mechanisms are used in the model; one is the relevant H_2/O_2 reactions proposed by Miller and Bowman [39] including 9 species and 20 reversible reactions, the other including 9 species and 21 reversible reactions is proposed by Gutheil et al. [29]. The first type of reaction mechanism is used to simulate d = 1 mm flame with Re = 30 and 330. The calculated radial and axial profiles of temperature and species concentrations are in good agreement with the measured data. Comparisons of the experimental measurements and numerical simulations indicate that the relevant H_2/O_2 reactions in GRI-MECH 3.0 can properly predict laminar hydrogen diffusion flames. The second type of reaction mechanism is used to simulate d = 0.2 and 0.48 mm flames with Re = 30. Comparisons between the predicted and measured data indicate that the trends of temperature, major species, and OH distributions are properly modeled. However, the code does not properly predict the air entrainment and pre-heating enhanced thermal-diffusive effects. The inability of the numerical simulations to correctly predict flame structure in diffusion H_2 microflames, where air entrainment and thermal-diffusive effects are dominant, suggests that a more detailed investigation of the chemical kinetic mechanism and molecular transport data is warranted.

Keywords: Microjet diffusion flames, Raman Scattering, Laser-Induced Predissociative Fluorescence (LIPF), Numerical simulation.

目錄

圖表目錄

第一章 緒論

1-1 簡介

自從理查費曼(Richard Feynman, Nobel Laureate in Physics, 1965)在 1960[1]及 1983 年[2]兩次演講中提到極微小機械(Infinitesimal Machinery)的概念之後，四十年來隨著半導體科技的進步，微機械在各種不同領域(諸如生物、醫學、光學、航太、機械與電機工程)的應用已對我們的日常生活產生重大的影響，然而，在這微米(Micron)世界裡的很多物理現象至今仍是成謎。國外的一些研究報告顯示，微米世界的一些物理現象偏離傳統的定律[3]，以微馬達(Micro Motor)為例，研究發現介於轉子(Rotor)與基材 Substrate)之間的摩擦力與其接觸面積有關，而表面的摩擦力亦大部分來自於轉子與基材之間的表面作用力，這個研究結果卻偏離了傳統的摩擦定律($f = mN$)，傳統的摩擦力(f)與正向力(N)成正比，而正向力與物體重力有關與接觸面積無關。其他例子如氣體流經微米槽(Micro Channel)及微噴嘴(Micro Nozzle)，實驗結果顯示氣體流經微米槽之質量流率高於傳統假設非滑動邊界條件(Non-slip Boundary Condition)所計算的結果[4]，同時氣體流經口徑小於 35 μm 之微噴嘴時其壓力降亦比傳統假設之計算結果高[5]，這些研究報告說明了微機械不但是新的科技同時也是值得深入研究的學術領域。

近幾年來國內在微機電系統(Micro-Electro-Mechanical Systems: MEMS)的研究正蓬勃發展，研究的方向主要還是在 IC 的設計與製造以及其相關之冷卻問題，至於在航太領域中以 MEMS 為基礎之化學微推進系統則尚未有研究報告出現。由於發展人造衛星的應用與研究乃國家的既定政策，而微衛星(Micro-Satellite)因其體積與重量皆比一般衛星要少很多，不論其軌道運行空間或是其發射成本考量皆優於目前使用的一般衛星，因此在發展衛星科技的同時，微衛星相關的科技研究是值得重視的課題。目前美國 NASA[6]正極力推展 1-10 公斤等級微衛星的研發，其將微衛星分成三個等級，第一種等級介於 5-10 公斤，直徑約 30 公分(相當於籃球大小)，其姿態控制(Attitude Control)所需之推力可利用 4.5 mN 之冷氣體推進器(Cold Gas Thruster)，或是利用直徑 5-10 公分之離子引擎(Ion Engine)。第二種等級約 1 公斤，直徑約 10 公分(相當於棒球大小)，其姿態控制所需之推進器就必須結合 MEMS 技術重新設計，因為低於微米大小的噴嘴喉部必須依靠 MEMS 技術才能製造。第三種等級低於 1 公斤，直徑約 1-3 公分(相當於五元硬幣大小)，體積如此小之微衛星其推進器將比第二種等級還要小，那麼如何將系統整合便成為關鍵技術，也就是說把所有的零組件整合在一片晶片上(System-on-a-Chip)。第三種等級目前僅止於概念階段，尚未真正投入研發，目前美國 NASA 真正投入研發的微推進系統也僅止於第一及第二種等級的應用。第一種等級的微衛星（如圖 1 所示）約 7 公斤，體積如鞋盒子大小，目前由噴射推進實驗室(JPL)負責研發，其姿態控制系統係由反應控制飛輪及冷氣體(GN2)推進系統所組成，為了降低質量與尺寸，冷氣體推進器將使用由 Redwood 系統公司所負責研發的 MEMS 閥。第二種等級的的微衛星（如圖 2 所示）約 1 公斤，目前由 AeroAstro 公司及美國空軍負責研發，其功能著重在遙測、通訊中繼傳送、

太空科學與天文物理的研究。

對微推進系統而言，其需求不外乎已超越目前傳統尺寸的推進技術就是必須從目前已具有的技術去作更先進的改良，目前有幾個概念已被提出並進行可行性研究，如美國噴射推進實驗室提出以 MEMS 為基礎之相變化推進器(Phase Change Thruster)，如昇華固體微推進器(Subliming Solid Micro-Thruster)和汽化液體微推進器(Vaporizing Liquid Micro-Thruster)（如圖 3 所示），固體推進劑為氨鹽(Ammonia Salts)，液體推進劑為水、氨(Ammonia)或聯氨(Hydrazine)。其他還有可提供高比衝之晶片型離子推進器（如圖 4 所示），或是目前正在構思的射頻(Radio-Frequency)和冷陰極(Cold cathode)推進器。此外，NASA Lewis 研究中心[7]亦提出研發高性能、無毒性之單推進劑(Monopropellant)系統以取代目前所使用的聯氨(N2H4) 單推進劑，唯耐高溫觸媒的開發是此高性能、無毒性之單推進劑系統是否能成功的關鍵。其他一些化學推進系統亦被考慮，如(1)利用氫、氧和惰性氣體(氮或氦)混合物之溫氣體推進系統以取代冷氣體推進系統，(2)熱解固體和混合物燃料之推進系統，(3)電解水以提供推進及電力雙重功能之推進系統，(4)以微渦輪機械(Microturbomachinery)為基礎之推進系統。

在研發微推進器的同時下列幾點因素必須加以考慮:(1)質量與體積：對第二及第三種等級的微衛星而言，其推進系統零組件之質量與體積必須降低 1 至幾個冪次以符合需求，對第一種等級而言，或許目前已具有之最小聯氨推進器或質量與體積都很小的離子引擎就可用來作姿態控制，（本整合型計畫之另一子計畫主持人袁曉峰教授曾研究過 1 磅推力之聯氨推進器，並經過實體驗證），但冷氣體推進器並不適合，因為氣體洩漏的考量。(2)氣體洩漏(Gas Leakage)：對微衛星的姿態控制而言，小型冷氣體推進器因為可提供小又精確的衝量，因此常被考慮作為姿態控制推進器，但是經由閥門而洩漏的冷氣體通常是目前衛星的致命傷，大部分失去聯絡的衛星皆因用來做推進劑的冷氣體提早洩漏所致，冷氣體的洩漏問題對微衛星而言衝擊將更大，因為負載的推進劑將隨著衛星質量和體積的縮小而減少很多，同時以 MEMS 技術所開發的閥亦因較小密封力(Sealing Forces)的問題尚未通過驗證，這方面亦需要更進一步的研發。(3)過濾和污染(Filtration and Contamination):由於推進系統中經常發現有微小固體顆粒(通常是由儲存槽的壁面所造成)，此微小固體顆粒在流經小尺寸的通道或噴嘴喉部時亦引起阻塞，以 MEMS 技術所製造的過濾網也許可濾掉大部分的微小固體顆粒，但仍須進一步研發。(4)高動量(高速度差)：一般尺寸或微衛星若需要高速度差的操作通常需要大量的推進劑或是使用高比衝的推進系統，尤其微衛星因受到質量的嚴重限制，高比衝推進系統的研發便顯的更形重要。(5)流場物理特性：當推進劑流經微推進系統的微小通道時，通常被考慮到的問題是流體是否轉換至分子流領域(Molecular Flow Regime)，美國噴射推進實驗室(JPL)及麻省理工學院(MIT)的研究群曾針對第一及第二種等級的應用進行評估，他們發現噴嘴喉部既使降至 1 微米非連續流仍未發生，轉換至分子流領域或許在尚未進行研發的第三種等級推進系統中發生，但其影響如何仍有待更深入的研究。

由於以 MEMS 技術為基礎之微推進器不但可整合感測器、致動器、以及控制電路

於單一晶片上，推進器的組成也單純化，所需能源也相對降低很多，這些都是國內發展微推進系統的優點及前景，可見其具有發展的重要性與前瞻性。綜觀國外正致力於以 MEMS 為基礎研發微推進系統的同時，在我們國內卻仍未起步，因此，我們延續過去六年共同使用研究設備與人力資源，共同執行整合型計畫所建立的研發能量，再結合具有 MEMS 背景的研究人員，共同提出此為期三年的整合型計畫，進行以 MEMS 為基礎之化學微推進系統研發。除了以 MEMS 為基礎之化學微推進系統研發之外，微噴流火焰亦被考慮為微推進系統之動力來源之一，因此在本整合型計畫中，本人將負責微系統光學診測系統的開發，並應用於微噴流擴散火焰的量測。

1-2 研究目的

近幾年來隨著對微衛星(Microsatellite)及微飛行器(Micro Aerial Vehicle)的需求與日俱增，驅動這些微系統之微動力來源的需求也隨著增加 [8]，而這些微系統更需要高密度動力來源來提供長時間的運轉與操作。通常碳氫燃料的能量密度約為一般電池的一百倍以上，既使考慮從燃料轉換成能源過程中的熱損失，微尺度之燃燒系統已被建議為替代電池的有效方法之一，惟要研發此燃燒系統，微型火焰的物理特性則必須更進一步的了解。

對於微型火焰的研究而言，目前已有一些實驗、理論或數值的分析報告出現。Ban 等人[9]曾針對對流－擴散控制之層流微型火焰進行實驗及理論研究，以探討擴散－傳輸對微型火焰結構之影響，他們發現浮力效應在微尺度火焰中可以忽略，但軸向擴散卻變得相對重要。Ida 等人[10]曾利用顯微照相及 CH* 自然放射螢光技術研究微型擴散火焰的熄滅極限，他們發現熄滅區域在靠近火焰底部，同時所推導之熄滅曲線可用雷諾數與噴嘴口徑的乘積表之。Matta 等人[11]亦曾利用照相和自然螢光量測技術以及理論分析研究微型擴散火焰的熄滅過程，他們發現理論預測之火焰熄滅及跳升熄滅極限與實驗結果相當吻合，因此認為微型擴散火焰的行為可用層流噴流擴散火焰的理論來描述之。除了實驗與理論研究之外，Nakamura 等人[12-14]亦利用數值模擬方法結合一步驟及多步驟化學反應機制，針對微型擴散火焰進行一系列的研究，探討燃燒器口徑對微型火焰結構的影響，他們發現所預測之 CH 分部與實驗結果相當吻合。

由以上的文獻回顧得知，對於微型擴散火焰的熱力及物理性質實驗量測則從未有報告出現。因此，實驗量測微型擴散火焰之溫度及組成份濃度不但可讓吾人對微型擴散火焰的物理特性及結構有更進一層的了解，同時所量測之實驗數據亦可提供數值模擬燃燒模式之驗證。

1-3 研究方法

過去針對微米槽(Micro Channel)之流力、熱傳、及流體傳輸現象的實驗研究大都利

用預埋入微米槽內之壓力或溫度感測器(Sensor)量測壓力[15]或溫度[16]分佈，但使用壓力或溫度感測器一次只能量測一種資訊，至於使用光學診測方法量測微米槽內或其出口處之溫度或組成份濃度分佈則尚無研究報告出現，因此本計畫將改良已建立之紫外光拉曼散射(Raman Scattering)及雷射誘發預解離螢光(Laser-Induced Predissociative Fluorescence)技術來研究微噴流擴散火焰之特性。

為了能同時取得微型噴流擴散火焰之溫度及組成份濃度分佈，具時間及空間解析之雷射診測技術則是必須的。而本計畫針對兩種不同口徑(d = 0.2 and 0.48 mm)之微噴流氫氣擴散火焰量測結果不但是世界首次，同時亦與日本名古屋大學 Nakamura 教授合作，由其進行數值模擬比對，研究成果已在第 30 屆國際燃燒會議發表，並即將刊登在該學會之 SCI 期刊(詳見附錄) 。此外，針對口徑 1 mm 兩種不同雷諾數之噴流火焰目前亦已完成不同化學反應機制的模擬，研究成果即將投稿 SCI 之 Combustion and Flame 或 Combustion Theory and Modeling 期刊發表。茲就本計畫之進行步驟詳述如下：

1. 改良已建立之紫外光雷射系統，使其量測體積足以解析微型火焰，而雷射能量又不致造成空氣及反應物離子化，並能降低 H_2O 解離。
2. 量測 CO_2 及 CH_4 冷噴流之拉曼散射光譜，以了解不致造成離子化之最低雷射能量及雷射解析度。
3. 利用改良後之雷射系統，針對層流平面氫氣火焰進行拉曼散射及 OH 螢光光譜量測，以校正雷射系統。
4. 利用校正後之雷射系統，針對不同口徑(d = 0.2, 0.48 and 1 mm)之微管噴流氫氣火焰進行溫度及組成份濃度的定量量測及火焰結構觀測，以瞭解對流－擴散控制機制對層流微型火焰結構之影響。
5. 提供實驗量測兩種不同口徑(d = 0.2 and 0.48 mm)之微噴流氫氣擴散火焰之數據予日本名古屋大學 Nakamura 教授，由其進行數值模擬比對，以瞭解化學反應模式是否正確。

第二章 雷射誘發螢光及拉曼散射之理論背景

2-1 雷射誘發螢光之濃度量測

傳統雷射誘發螢光技術是利用雷射光激發低能階粒子至高能階，激發後的高能量粒子可由自然螢光或是其他粒子的撞擊而喪失其多餘的能量回到低能階的穩定狀態。若下標 1 表示低能階，下標 2 表示高能階，則螢光強度 I[17]：

$$I = C(T,P)N_1 \frac{F}{F+Q} I_n B_{12} f_B(T) \qquad (2\text{-}1)$$

其中 C 是與溫度、壓力有關的實驗光學校正常數，N_1 是激發前低能階粒子濃度，F 是螢光速率亦即是愛因斯坦放射係數 A_{21}，Q 為冷卻速率，I_n為雷射光之譜線強度，B_{12} 為愛因斯坦吸收係數，$f_B(T)$是波茲曼分率。重要的是 B_{12} 與 F 或 A_{21} 均是不與溫度、壓力有關的分子性質常數，Q 卻是隨著溫度、壓力、組成成份等等而不同，甚難估算。

當在低壓狀態下，$Q << F$，此時 Q 可忽略不計，可由螢光訊號的強弱，經實驗校正結果計算粒子濃度 N_1，但是不準度卻是會隨 Q 值得升高（如壓力提高）而增加。如果從低能階躍遷至高能階的某一個特殊震動能級，則可能會跑到先分解曲線(Predissociative curve)然後分解。此時分子在高能階除了存在有螢光速率 F、冷卻速率 Q 之外尚有先分解速率 P，若 $P >> Q$，則螢光強度[18]：

$$I = C(T,P)N_1 \frac{F}{F+Q+P} I_n B_{12} f(T) \approx CN_1 \frac{F}{P} I_n B_{12} f_B(T) \qquad (2\text{-}2)$$

因為 F、P 是僅與所激發的分子有關，而與壓力等等無關，故 LIPF 技術可降低冷卻效應的影響，更可應用在高壓環境中得到合理精確度的定量分析。但是應用 LIPF 技術有兩個條件；一是必須激發至冷卻速率與先分解速率相較下可忽略的能階，否則誤差會相當大；另一是因為躍遷至此種能階的機率相當小，必須使用高功率雷射作為激發光源。

實驗光學校正常數 $C(T, P)$包含了一些實驗設備上與理論上均會影響螢光訊號的因素。譬如說光學設備方面的鏡片，其穿透率及反射率皆會直接影響觀測點位置的雷射光能量強度與觀察的螢光訊號，不過這些因素是不會隨著溫度、壓力而有所變化。除此之外，$C(T, P)$亦包含一個會隨著溫度、壓力的因素，這個因素即是 Voigt Profile。Voigt Profile 描述譜線寬度隨著溫度、壓力的變化，在激發的過程中，表示的是吸收程度，在相同的

雷射光波長波形下，Voigt Profile 下的整個面積就是控制吸收程度強弱的其中一個關鍵因素。

應用 LIPF 技術量測濃度需要量測 OH 分子的某個能階($A_2 \rightarrow A_1$)的螢光訊號，然後經過一系列的校正步驟，再利用電腦模擬計算的濃度與其做比較，即可從中找出校正常數(calibration factor)。假若 C_F 表示校正常數，則：

$$N_{OH} = Signal_{corrected} \times C_F \tag{2-3}$$

2-2 拉曼散射之溫度及濃度量測

在自然振盪的拉曼散射系統中，雷射光被聚焦成一小體積，這個小體積的位置就是火焰中所要量取資料的點，火焰中不同的分子會吸收一小部份雷射光的能量而造成分子內能的增加，這些高內能的分子會躍升至生命期很短的虛能階(Virture state)，由於能量守恆的原理，這些虛能階的分子會瞬間放出光能以降低其內能，當放射光的波長和入射光(即雷射光)的波長相同時即為彈性散射(Elastic Scattering)，學名稱為芮里散射(Rayleigh Scattering)。若放射光的波長和入射光的波長不同則稱為拉曼散射。

拉曼散射光的強度比芮里散射光的強度要弱很多，同時拉曼散射的過程中包含著分子內能的改變，亦即分子振動能量階的改變。當最末的振動量子數(Vibrational quantum number)比最初的要大，$\Delta V = +1$，則這個過程稱為史托克斯(Stokes)拉曼散射，若 $\Delta V = -1$，則稱為反史托克斯(Anti-Stokes)拉曼散射。在散射過程中，由於能量守恆的原理，所以史托克斯散射光會出現在波長比雷射光波長要長的方向，而反史托克斯散射光則會出現在短波長的方向。振動的拉曼散射由三個分支(Branch)所組成，即 Q、O 及 S，它們的轉動量子數 J 之變化分別為 $\Delta J = 0, -2$ 及 $+2$，Q 分支的散射強度比 O 和 S 還強。為了利用 Q 分支的波段來量測火焰的溫度與濃度，它的散射強度、光譜形狀及光譜出現的位置則必需詳加研究。

對於雙原子的分子而言，它的能量項值(Term value)$G(v, J)$包含諧振子(Harmonic oscillator)與非諧振子(Anharmonic oscillator)項，剛性與非諧轉動項及振—轉交互作用項[19]，同時可由下列式子表示之:

$$G(v,J) = \frac{E(v,J)}{hc} = w_e(v+\tfrac{1}{2}) - w_e x_e(v+\tfrac{1}{2})^2 + w_e y_e(v+\tfrac{1}{2})^3$$
$$+ B_0 J(J+1) - D_0 J^2(J+1)^2 - a_e v J(J+1)$$
$$- b_e J^2(J+1)^2 + \cdots \tag{2-4}$$

其中 $E(v, J)$是(v, J)階的能量，$?_e$，$?_e x_e$ 及 $?_e y_e$ 是振動的常數，同時 $?_e y_e << ?_e x_e << ?_e$，$B_0$ 為最低振動階$(v = 0)$的剛性轉動常數，D_0 為最低振動階的剛性非轉動常數，a_e 與 $ß_e$ 為振動與轉動的交互作用常數，h 為普郎克常數(Planck constant)，c 為光速。對基本的振動波段$(? J = 0, ? V = 1)$而言，其拉曼頻移(Raman shift)可由(2-4)式而得:

$$\Delta G(v+1, J \leftarrow v, J) = w_e - 2w_e x_e(v+1) + w_e y_e(3v^2 + 6v + {}^{13}\!/_{4})$$

$$- a_e J(J+1) - b_e J^2(J+1)^2 + \cdots \qquad (2\text{-}5)$$

因為 $ß_e$ 比 a_e 小很多，所以可忽略不計。為了瞭解 Stokes Q 分支的轉變，吾人可假設波茲曼分佈(Boltzmann distribution)及利用 Placzek 的偏光理論(Polarizability theory)來探討其輻射通量(Radiant flux) $S(v, J)$[20]：

$$S(v, J) \propto \frac{g_I(2J+1)(v+1)v_s^{\,4}A_{\Delta J=0,J}}{Q_{rot}Q_{vib}}\exp\{\frac{[-G_0(v) - F_v(J)]hc}{kT}\} \qquad (2\text{-}6)$$

在(2-6)式中，g_I 為核自旋常數，對整數值(lntegral values)的核自旋 I 而言，其又可分為對稱型分子階(Symmetric molecular levels) $g_I = (2I + 1)(I + 1)$，及反對稱型(Anti-symmetric)分子階 $g_I = (2I + 1)\, I$。對奇半數值(odd-half-integral values)I 而言，其對稱型分子階之自旋常數為 $g_I = (2I+1)$，而反對稱型分子階之自旋常數為 $g_I = (2I + 1)(I + 1)$，Q_{rot} 及 Q_{vib} 分別為轉動的及振動的配分函數(Partition function)，v_s 為史托克拉曼偏移頻率(Stokes Raman shift frequency)，$A_{\Delta J=0,J}$ 為受轉動量子數影響之 Placzek-Teller 係數，這個值可由計算而得，但對較高的轉動量子數而言其影響通常可以忽略不計。而在指數項內之 $G_0(v)$ 及 $F_v(J)$則是將(2-1)式分成振動的及轉動的能量項值，$G_0(v)$代表基態(Ground state)的振動項值，$F_v(J)$則是轉動的項值，k 為菠茲曼常數，T 為溫度。

由(2-6)式可知，在不同的溫度下，對不同的分子而言，其輻射通量會有變化，拉曼散射即利用此原理並選擇特定分子以量取溫度。因此溫度的量測可由光譜的量測而得。通常光譜之取得是經光譜儀之掃描而得，但以此所得之溫度並非瞬時量測，同時亦僅能應用於層流火焰溫度的量測，若要取得漩渦紊流火焰溫度則必須以其他方法為之。同時為了取得單脈衝各組成份濃度的量測，(2-6)式可簡化為：

$$Q_i = K_i Q_l [N_i] f_i(T) \qquad (2\text{-}7)$$

在(2-7)式中，$[N_i]$為某組成份 i 之濃度，Q_l 為雷射光之能量，K_i 為跟拉曼散射截面積、

幾何形狀及光學效率有關之比例常數，$f_i(T)$為與溫度有關之波寬係數(Bandwidth factor)。K_i及$f_i(T)$可組合成一校正常數，只要從平面火焰得到校正常數，則漩渦紊流火焰之各組成份的濃度便可由(2-7)式而得。同時由於本研究之部份預混漩渦火焰係在一大氣壓下燃燒，因此火焰之溫度可由量測之組成份總濃度依理想氣體狀態方成式$P = \sum n_i kT$而得。

2-3 系統之量測分析

在拉曼量測系統中，為了能有較佳的解析度(Spatial resolution)，其雷射光被聚焦成一小體積，而小的取樣體積所產生的拉曼散射信號亦較弱，因此拉曼量測系統之信號測不準(Signal uncertainty)主要乃由探測器發射光電子之機率自然性所致之發射雜訊(Shot noise)。在使用有光陰極板(Photocathode)探測器之拉曼量測系統中，其散射信號是以帕松統計(Poisson statistics)為之[17]。因此，史托克斯或者是反史托克斯信號之相對標準偏差(Relative standard deviation)可以下式表之:

$$\frac{s}{N} = \frac{1}{\sqrt{N/k}} \tag{2-8}$$

s 為相對標準偏差，N 為探測光子平均數，k 為 ICCD 照相機之雜訊係數。

第三章 實驗設備

本實驗的整體設備包括燃燒器、流量控制系統、二維定性雷射誘發螢光量測系統、拉曼散射及定量雷射誘發螢光量測系統，茲簡介如下：

3-1 燃燒器

本計畫執行時是使用兩種不同形式的燃燒器，一是出口面積為 25.4 mm x 25.4 mm 的平焰爐(Hencken Flat Flame Burner)，用來產生不同當量比的層流火焰，以供拉曼散射及 LIPF-OH 量測技術校正用，並求得濃度與量測訊號兩者之間的關係式；另一種是微管燃燒器，用來產生微型火焰以供本研究，微管燃燒器的外形及裝置如圖 5 所示。

3-2 流量控制系統

為了能準確的控制供應燃燒器之燃料及空氣流量，本研究空氣流量之流量控制系統係採用 Teledyne-Hastings 之質量流量計(Mass flowmeter)，質量流量計之最大流率為 500 SLPM，準確度為流量的 ±1%。燃料之流量控制系統係採用 Brooks 之質量流量計，燃料質量流量計之最大流率分別為 20 及 30 SLPM，準確度皆為流量的±1%。

3-3 二維雷射誘發螢光(2D LIF)量測系統

本實驗所使用之二維雷射誘發螢光量測系統如圖 6 所示，對二維雷射誘發預解離 OH 螢光量測來說，窄波可調式之準分子雷射(Narrowband tunable KrF excimer laser)其波長被調至 248.46 nm 以激發 A-X(3，0)躍遷之 P_2(8)轉動線(Rotational line)，並利用焦距為 1000 mm 之柱狀鏡(Cylindrical lens)將雷射光束聚成高 25 mm 厚 0.2 mm 之薄片以垂直切過火焰中心。OH 螢光訊號係由相機鏡片收集並將影像存放至 ICCD 相機之晶片上，在相機鏡片之前方並置有一液體濾光鏡以濾掉 Rayleigh 光。雖然 Stokes 拉曼散射光亦會進入相機，但由於 OH 螢光比拉曼散射光要強很多(1000/1)，因此，拉曼散射光對 OH 螢光訊號的干擾非常微小，同時 ICCD 相機之匣閥時間被設定為 100 ns 以排除火焰之 OH 自然放射螢光進入相機。

3-4 拉曼散射量測系統

用於量測微管氫氣火焰之拉曼散射(Raman Scattering)結合雷射誘發預解離螢光(Laser-induced Predissociative Fluorescence, LIPF)量測技術已經被開發完成[21]並將其改良後用於此次的實驗研究，整個雷射光學量測系統如圖 7 所示。本研究所使用之雷射光源為德國 Lambda-Physik LPX-250T 之窄波可調式(指可調波長)氟化氪(KrF)準分子雷射(Excimer laser)，此型雷射之波長可調範圍約為 1 nm(248-249 nm)，脈寬約為 30 ns，最大重覆率(Repetition rate)為 50 Hz，若使用氦氣為緩衝氣體(Buffer gas)，則每脈衝之最大能量約為 250 mJ，若使用氖氣為緩衝氣體則每脈衝之最大能量可達 450 mJ，雷射光之發散率約為 0.2×10^{-3} rad。此型雷射是由一個振盪器(Oscil1ator)與一個放大器(Amplifier)所組成，在振盪器一端之稜鏡(Prism)及光柵(Grating)是用來將振盪器輸出之雷射光變窄之後反射回振盪器然後由另一端輸出，並經由兩面反射鏡將窄波導入放大器之後再由放大器將光源輸出。通常伴隨窄波輸出之光源仍有一部份為寬波，窄波之強度與寬波之強度比則稱為鎖定效率(Locking efficiency)，其中雷射混合氣體之使用長久、雷射腔之氣體壓力以及雷射光學鏡片之調整是否恰當等等因素皆將影響鎖定效率。此型雷射之鎖定效率依出廠規格應大於 90%，愈高之鎖定效率愈能提供較佳之拉曼量測，此乃因較高之鎖定效率其放射波帶較窄，如此可將雷射波長調至離開 OH 振動線(Rotational lines)之位置，以避免直接激發 OH，進而造成 OH 螢光干擾拉曼散射光，這就是為何使用窄波段可調式雷射而不使用寬波段雷射之主要原因。

雷射波長係調至 248.623 nm 以量測氫氣火焰中之主要組成份(O_2、N_2、H_2O、H_2)及次要組成份(OH)的濃度並避免激發太強的 O_2 及 OH 螢光進而干擾拉曼散射訊號，同時亦可避免激發 H_2O 吸收譜線，降低雙光子解離 H_2O。從焦距 200 mm 聚焦鏡片上所散射的光係由一光電增倍管量測以做為雷射脈衝能量之相對參考，雷射光被聚焦到平焰爐或漩渦燃燒器的上方，螢光及拉曼散射光是經由兩個 Cassegrainian 反射鏡聚焦並通過 10 mm 厚之液體濾光片之後進入配有 ICCD 照像機之光譜儀；SPEX 500M 光譜儀係用來量測 O_2、N_2 之拉曼訊號，而 Spectra Pro-275 光譜儀係用來量測 H_2O、H_2 之拉曼訊號及 OH 之螢光訊號。為了要確保兩個光譜儀是量測到相同的點，吾人係將 100 μm 的金屬線置於量測點的中心以作為校正之用。經由 ICCD 照像機所取得之資料乃儲存於個人電腦，以便日後作進一步資料處理。

由於所使用之準分子雷射其雷射光發散率約為 0.2×10^{-3} rad，若以焦距 2000 mm 之聚焦鏡片聚焦，則其理論焦點之最小尺寸約為 0.4 mm，那麼如果使用此解析度來量測 1 mm 甚至微米尺寸之微管，則解析度不夠。因此，本實驗採用 200 mm 之聚焦鏡聚焦，其焦點之最小理論尺寸約為 0.04 mm，但高度 20 mm 寬度 5 mm 之雷射光束經由焦距 200 mm 之球狀鏡聚焦單發打在感光紙之後，經顯微鏡量測其焦點截面積約為 $0.02 \times 0.04\ mm^2$ (如圖 8 所示)，其中 0.04 mm 為平行於噴流方向之焦點高度，但使用如此短焦距之聚焦鏡片必須降低雷射之輸出脈衝能量，否則因單位體積的雷射能量太高將造成氣

體離子化(Ionization)現象，同時由於所量測之體積亦比使用焦距為 2000 mm 之聚焦鏡片縮小 10 倍，因此散射光之強度也將大大的降低，這對使用拉曼散射技術量測微米流場之組成份濃度將有極不利之影響。由於光譜儀之入口隙縫係與雷射光垂直，依光譜儀入口隙縫寬度(100 μm)及卡塞格侖反射鏡之放大倍(M = 2.34)率推算，所收集之雷射光長度為 0.04 mm，因此，本雷射系統之取樣體積約為 0.02 × 0.04 × 0.04 mm^3，本系統之空間解析度與前人之單點[22-24]或多點[25，26]量測系統大約小 10 倍以上，在如此小之量測體積下若使用高脈衝雷射能量則非常容易造成空氣離子化，因此量測微管氫氣火焰之前除了必須降低雷射輸出能量之外，雷射光路亦必須利用多片反射鏡及分光鏡加以調校，以確保空氣及 H_2O 不致離子化及解離。而本系統之時間解析度係雷射之脈寬 30 ns。

3-5 系統校正與數據處理

對組成份的濃度量測而言，由某組成份 i 所產生之拉曼散射訊號經由 ICCD 照像機蒐集並積分之後所得之總訊號 Q_i 可由(2-7)式表之[22]。對雙原子分子而言，其波寬因子可由理論計算而得，但對三原子分子而言，由理論計算而得之波寬因子並不可靠，因此，將 K_i 及 f_i 集合成校正係數 $C_i = 1/K_i f_i$ 並由平面火焰校正而得。本量測系統係以 12 個不同當量比之氫氣/空氣與 12 個不同當量比之氫氣平面火焰加以校正，對每個火焰而言，火焰溫度是由量測之 N_2 Stokes 光譜與理論計算的光譜相比較而得[21]，量測的火焰溫度與質量流率可用來計算化學反應平衡時之組成份濃度並校正拉曼及 OH 螢光訊號。

對 OH 的濃度量測而言，吾人利用雷射誘發 OH 預解離螢光將 $A^2\Sigma \leftarrow X^2\Pi$ 系統之 OH 分子從 $v'' = 0$ 激發至 $v' = 3$ 能階[27]，然後量測 $v' = 3$ 至 $v'' = 2$ 之螢光，其波長出現在 297 nm，量測波長出現在 297 nm 之 OH 螢光之好處係此螢光可用來修正 OH 對 H_2O 拉曼訊號的干擾，Chen 和 Mansour [28]及 Chen 等人[26]曾在研究 H_2/Ar 與 CH_4 火焰時量測出現在波長 272 nm 之 OH 螢光，以作為 OH 濃度量測，唯若量測波長 272 nm 之 OH 螢光便無法對 H_2O 拉曼訊號的干擾做修正，如此若量測點之火焰接近完全混和分率(Stoichiometric mixture fraction)則會造成很大的 H_2O 濃度量測誤差[25，28]。

過去對氫氣-空氣火焰的研究顯示，在貧油火焰時雷射誘發 O_2 螢光出現在 258, 268, 278，288 及 298 nm 之波長，而僅出現在波長 288 nm 之 O_2 螢光未受其他訊號干擾，因此可用來修正雷射誘發 O_2 螢光對 O_2 (258 nm)及 H_2 (277 nm)拉曼訊號及 OH 螢光訊號的干擾。除了必須修正雷射誘發 O_2 螢光對其他訊號的干擾之外，拉曼訊號之間的相互干擾亦必須加以修正。除此之外，吾人亦量測波長在 260 nm 及 283 nm 之訊號以作為背景雜訊和 PAH 量多寡之監測參考。

因為利用拉曼散射量測溫度係將所有量測之組成份濃度之總和加起來之後，利用理想氣體狀態方程式求得，而訊號間相互的干擾以及螢光干擾的修正將影響溫度的決定，

因此溫度係由疊代方式求得。本研究所使用之拉曼/LIPF-OH 影像量測系統係為點量測(Point measurement)，並利用平面火焰校正，通常對每個校正火焰雷射擊發 200 次以求其平均值，圖 9 是利用氫氣/空氣層流平面火焰校正拉曼/LIPF-OH 量測系統之溫度與組成份莫爾分率對混和分率(ξ_H)之校正結果，對每個校正火焰而言，平均值和 RMS 變化值係以符號及誤差棒表示並和理論計算之絕熱平衡曲線相比較。混和分率(Mixture fraction)的變化與組成份之濃度有關並如下式所示：

$$x_i = \frac{Y_i - Y_{i,o}}{Y_{i,f} - Y_{i,o}} \tag{3-1}$$

其中 Y_i 為量測體積內 i 原子之質量分率(i = H，C，O，N)，$Y_{i,f}$ 為燃料中 i 原子之質量分率，$Y_{i,o}$ 為氧化物中 i 原子之質量分率。單脈衝量測時其誤差主要來自陰極板光電放射過程所產生之雜訊，而圖 9 所顯示之誤差亦包含其他儀器之雜訊以及火焰之擾動。本實驗系統之誤差為量測 2190 K 時其溫度誤差約 12%，量測高溫時之主要組成份濃度誤差約介於 6-15%之間，次要組成份(OH)濃度誤差約介於 15-25%之間，實驗誤差在此範圍與其他紫外光拉曼系統相當[25-26]，校正後之拉曼/LIPF-OH 量測系統就可用來研究微噴流氫氣火焰。

第四章 數值模擬

為了模擬微管氫氣擴散火焰，本研究採用兩種不同計算軟體及化學反應模式，但其統御方程式皆包括質量守恆、動量守恆、能量守恆、及組成份守恆，並假設軸對稱計算區域及利用有限體積與交錯網格計算。第一種數值模擬程式係利用國家高速網路與計算中心之 CFDRC 計算軟體，並使用內含 9 個組成份及 20 個氫－氧可逆反應步驟[39]及完整傳輸性質的計算，此外亦可加入氫氣熱擴散效應之模擬，此模擬程式用於管徑 1 mm 之兩種不同雷諾數(Re = 330 及 30)火焰之計算。

第二種數值模擬程式係由日本名古屋大學中村佑二教授所開發，並與其合作進行管徑 0.2 及 0.48 mm 兩種火焰之計算，其計算模型如圖 10 所示。此計算假設 Poiseuille 流之氫氣往上噴入靜止之大氣，由圖 10 可見，微管係置於計算區域之內，因此在微管內外之性質皆可計算，同時可考慮組成份擴散回管內之效應。管壁之邊界條件為不滑動、無觸媒反應及常溫(T = 300 K)狀態，並考慮重力為外力。微管內徑、管壁厚度及氫氣體積流率皆設定與實驗條件吻合，並採用完整的傳輸性質計算及內含 9 個組成份與 21 步驟之氫氣－空氣化學反應模式[29]，組成份之熱力學性質係使用 CHEMKIN 資料庫[30]，傳輸性質則使用 Smooke 之簡化模式計算[31]，H_2O 之輻射熱損失係使用簡化之薄光學模式計算[32]。在數值運算方面，通量分離採用中央差分法，時間積分採用尤拉隱式法，並於疊代過程中每個時間步階採用過度鬆弛法，並使用 SIMPLE 法則[33]解 Navier-Stokes 方程式之壓力項。總網格數為徑向 81 格軸向 141 格，最小網格為接近噴嘴處之 $D/10$，隨著往外邊界移動而加大網格。程式開始計算之時間步階為 1.0×10^{-4} 秒，並計算至達到穩態為止。

第五章 結果與討論

在未針對微管氫氣擴散火焰進行量測之前，吾人先對 D = 1 mm 微管(如圖 5 所示)出口未反應氣體進行拉曼散射光譜量測，1 mm 微管係固定在微調精度為 1 μm 之雙軸移動平台之上。準分子雷射波長調至 248.623 nm 以避免直接激發 OH 及 O_2 而造成其螢光干擾拉曼訊號，雷射輸出能量為 160 mJ/pulse，SpectraPro-275 光譜儀波長設定在 270 nm，入口隙縫設為 100 μm 以收集足夠的散射光作光譜分析又不致造成譜線太過寬廣而造成不同訊號之譜線相互干擾，由於光譜儀之入口隙縫係與雷射光垂直，依光譜儀入口隙縫寬度(100 μm)及卡塞格侖反射鏡之放大倍(M = 2.34)率推算，所收集之雷射光長度為 0.04 mm。

5-1 CO_2及 CH_4冷噴流光譜量測

本研究係將未反應氣體（CO_2 及 CH_4）由微管噴出，並在離微管出口高度 x/D = 1，2，3 處量測其拉曼散射光譜。首先吾人將 CO_2 氣體由微管噴出，並在離微管出口高度 x/D = 1 處進行拉曼散射光譜量測，其拉曼譜線如圖 11 所示。吾人發現在雷射輸出能量為 160 mJ/pulse 時，CO_2 很容易被離子化(Ionization)，因此造成寬廣而無法確認 CO_2 之譜線出現。依本實驗所使用之雷射波長(248.623 nm)推算，CO_2 之拉曼譜線應出現在 257 nm 處，惟尚無法確認之峰值卻出現在 283 nm 處，造成如此寬廣譜線的可能反應步驟如下：

$$CO_2 + h\nu \rightarrow CO_2 + CO_2^+$$
$$CO_2 + h\nu \rightarrow C + O_2 + C^+ + O_2^+$$
$$CO_2 + h\nu \rightarrow CO + O + CO^+ + O^+$$

由於離子化後之 CO_2 拉曼譜線無法確認，同時在不同徑向位置 CO_2 之離子化程度亦不一樣，造成量測上的困難，因此必須將雷射光能量降低以避免將 CO_2 氣體離子化。

經過一連串降低雷射光能量測試之後，吾人發現當雷射光能量為 60 mJ/pulse 時，CO_2 不再離子化。因此，將量測點移至離微管出口 x/D = 3 處，並在徑向位置 r/D = 0.2 及 0.7 處進行量測，其量測結果與無 CO_2 噴流時所量測之光譜如圖 12 所示。圖 12a 為無 CO_2 噴流時所量測之室內空氣拉曼光譜，O_2、N_2 及 H_2O 之拉曼光譜各出現在 258.4、263.7 及 273.2 nm 處。當 CO_2 由微管噴出並將量測點移至接近噴流中心時(r/D = 0.2)，很強的 CO_2 拉曼訊號出現在 256.6 及 257.3 nm 處，由圖 12b 可見微量的外界空氣已捲入 CO_2 噴流中。但若量測點接近噴流與外界空氣之交會處(r/D = 0.7)，則 CO_2 與 O_2 之譜線相互重疊而造成訊號分辨上的困難(如圖 12c 所示)，由此可見 CO_2 氣體並不適合用來測試雷射系統之解析度。

接著吾人利用未燃之 CH_4 氣體來測試，吾人發現當雷射光能量為 60 mJ/pulse 時 CH_4 不但不會被離子化或點燃，其拉曼散射訊號亦非常強且其譜線亦未與其他譜線相互干擾(如圖 13 所示)，因此，吾人將 CH_4 流量固定在 2.1 lit/min，微管出口速度為 44.6 m/s，雷諾數為 2700，在離微管出口 x/D = 1、2、3 處沿著徑向方向(每次移動 0.1 mm)進行光譜量測，每一量測點雷射激發 200 次，平均後之光譜再經積分後 CH_4 之濃度分布如圖 14 所示。由圖 14 可見，CH_4 在三個不同高度之濃度呈高斯分布(Gaussian distribution)，由於 CH_4 噴流的密度比周圍空氣的密度為低，理論上當 CH_4 噴出微管時會造成浮力效應(Buoyancy effect)，但因本噴流為層流(Re = 2700)，且量測高度之區域受噴流動量所主控，以致像無浮力噴流(Non-buoyant jet)一樣，其濃度及速度呈高斯分布[34]。由於雷射量測系統之解析度為 0.04 mm，同時每隔 0.1 mm 量測一點，因此 1 mm 內便有具高度解析之 10 個量測點。反之，若解析度為 0.5 mm，既使每隔 0.1 mm 量測一點，也會因解析度不夠而造成量測誤差。

雖然本研究並未量測噴流之速度分布，但利用所量測之濃度分布(如圖 14 所示)及噴流之相似性(Similarity)可推算出噴流流場之速度分布。吾人可利用 x/D = 1、2、3 處所量之濃度得到濃度分布半徑(Half-radius of concentration)，在 x/D = 1、2、3 處之濃度分布半徑分別為 R_f = 1.2、1.24 及 1.26，將各個高度之濃度除以噴流中心之濃度及將噴流半徑除以濃度分布半徑之後，其結果如圖 15 所示。由圖 15 可見此噴流具有自似性(Self-similar)，同時由於速度及濃度分布在噴流中存有相似性，因此，速度分布可由下列公式表之：

$$\frac{U}{U_c} \cong \frac{f}{f_c} = \exp\left[-3.25\left(r / R_f\right)^2\right] \qquad (5\text{-}1)$$

其中 U_c 為噴流中心線速度。對圓管噴流而言，在無浮力效應區域之中心線速度可由下列公式表之[34]：

$$U_c = 6.2\left(\frac{r_0}{r_a}\right)^{1/2}\left(\frac{x}{D}\right)^{-1} U_0 \qquad (5\text{-}2)$$

其中 r_0 為噴流出口流體之密度，為 r_a 周圍空氣之密度，U_0 為噴流出口速度。以 CH_4 噴流而言，r_0/r_a = 0.544，U_0 = 44.6 m/s，則在 x/D = 1、2、3 處之中心線速度分別為 20.4、10.2、6.8 m/s，由式(5-1)所推算出之速度分布如圖 16 所示。

由實驗結果可知，經改良後之雷射系統其解析度足以解析 1 mm 之微管，未來本雷射系統可應用於寬度 1 mm、長度 20 mm 及不同深度之微槽出口的量測[35]。微槽係以微機電技術內鍍白金薄膜而成之微反應系統，白金係觸媒的一種，其可用來降低燃氣之反應活化能，在開發微米燃燒器的過程中扮演重要的角色。為了對微槽內觸媒燃燒反應有更進一步的瞭解，微槽內或其出口處之溫度或組成份濃度分布必須取得。惟若要使用

雷射光學系統量測微槽內之溫度或組成份濃度則必須考慮微槽視窗是否足以承受雷射光強度及微槽內壁面光反射的問題，因此，在微槽出口處量測是較佳的選擇。利用雷射拉曼散射技術量測燃燒流場雖可同時取得溫度及組成份濃度之資訊，但拉曼散射訊號隨著溫度的升高而降低，同時量測微槽時之取樣體積亦非常微小，因此量測用來推算反應效率之 H_2O 時，其拉曼散射訊號是否足夠將影響量測之準確性。克服此困難之解決方法分別為利用 N_2 光譜吻合法(Spectrum-fit method)量測溫度。

5-2 管徑 1 mm 之噴流氫氣火焰照相觀測

在未針對更細之微管噴流火焰進行量測之前，吾人先對管徑 1 mm 所產生之氫氣噴流火焰進行量測。為了能正確計算噴流出口速度以及提供管徑尺寸及厚度給數值模擬比對之用，吾人利用顯微鏡所量測之微管內徑為 1 mm，厚度為 0.17 mm，如圖 17 所示。氫氣經由微管噴出之後，與靜止之大氣進行燃燒，形成一層流擴散火焰。微管長度至少 5 cm 以上，長度/口徑比大於 50，因此微管噴流微全展(Fully developed)噴流，兩種不同雷諾數(Re = 330 and 30)之噴流火焰操作條件如表 1 所示。Re = 330 之火焰其噴嘴出口體積流率為 1696.5 cc/min，質量流率為 2.336 mg/s，速度為 36 m/s，火焰照相圖如圖 18 所示，左邊之火焰為全火焰，右邊為火焰底部之放大照相圖，由右圖可看出火焰由噴嘴出口往下包覆，包覆長度約為 0.52 mm，由於火焰包覆管子，因此火焰會熱傳至管壁進而加熱管壁，利用紅外線照相機量測火焰包覆管子之溫度為 703 K。當雷諾數降為 30 時，火焰隨著縮小成雞蛋形狀，其噴嘴出口體積流率為 155.37 cc/min，質量流率為 0.214 mg/s，速度為 3.3 m/s，火焰照相圖如圖 19 所示，由圖中可看出，火焰不但由噴嘴出口往下包覆同時亦將管子加熱成紅色，紅外線照相機量測火焰包覆管子之溫度為 803 K。

5-3 管徑 1 mm 之噴流氫氣火焰二維 OH 激發螢光量測

為了要瞭解真正的火焰結構，吾人利用二維雷射誘發螢光技術(如圖 6 所示)量測兩種不同雷諾數(Re = 330 and 30)之噴流火焰 OH 分布，如圖 20 及 21 所示。為了降低管子壁面所造成之 Mie 散射，雷射光切面保持離管子出口 1 mm 處開始量測，圖 20 為 Re = 330 時之單脈衝 OH 螢光分布圖，由於在火焰的前緣 OH 強度達到最大值，因此，二維之 OH 影像量測代表火焰之瞬時反應區。由圖中可看出反應區出現在燃料與外界空氣之混合層，OH 最大值分布於混合層之中心，並由噴嘴出口 r = 3 mm 處沿著下游往外擴張，在高度 x = 30 mm 處火焰最寬，超過此高度之後火焰逐漸往內縮，而由 OH 分部所量測之火焰長度約為 70 mm。當 Re = 30 時，所量測之 OH 呈現雞蛋形狀，同時火焰長度縮短度約 6 mm(如圖 21 所示)。由圖中可看出此火焰之反應區寬度約為 2 mm，在中心高度約為 1.5 mm 以後 OH 擴散至噴流中心，以致行成雞蛋形火焰。

5-4 管徑 1 mm 噴流氫氣火焰之熱物性質

5-4.1 雷諾數 330 火焰之實驗與計算模擬比較

為了取得兩種不同雷諾數噴流火焰之熱力及物理性質，吾人利用拉曼散射及 LIPF-OH 量測技術沿著火焰徑向及軸向方向進行溫度及組成份濃度之定量量測，並對每個量測點取 200 發雷射量測。對於每單發雷射而言，其可提供火焰溫度及組成份之資訊，其他性質如密度與混合分率亦可經由量測資訊計算而得。圖 22-25 為 Re = 330 時四個不同高度(x = 1, 5, 25, 50 mm)之量測與數值模擬平均溫度及組成份濃度(O_2, N_2, H_2O, OH)徑向分布比較圖，量測數據係以符號表示，而計算結果則以線條表之。圖 22 為高度 x = 1 mm 處之實驗與計算平均溫度、主要組成份及 OH 質量分率徑向分布比較圖，由圖中可見火焰溫度從未燃之冷勢流低溫快速提升至 2051 K 並平坦的通過反應區，而且火焰最高溫度與 OH 濃度最大值同時出現在 r = 3 mm 處，也就是 H_2 及 O_2 完全燃燒處。而在此高度因仍處噴流勢流錐，故噴流中心之 H_2 尚未開始反應。由實驗量測與數值計算之結果相互比較，吾人發現計算之溫度及組成份濃度分布趨勢與實驗結果非常吻合，只是計算結果得到較窄的反應區。

圖 23 為高度 x = 5 mm 處之實驗與計算平均溫度、主要組成份及 OH 質量分率徑向分布比較圖，在此高度 N_2 已擴散到噴流中心，同時最高溫度及 OH 最大值的位置亦往徑向移至 r = 4.4 mm 處，此處之火焰最高溫度為 2247 K，且其出現的徑向位置與 OH 的峰值重合。由實驗量測與數值計算之結果相互比較，吾人發現計算之溫度及組成份濃度分布趨勢與實驗結果非常吻合，只是計算結果得到較窄的反應區。

圖 24 為高度 x = 25 mm 處之實驗與計算平均溫度、主要組成份及 OH 質量分率徑向分布比較圖，在此高度噴流中心溫度已達到 1274 K，同時 H_2 之質量分率亦已降低至 0.08，最高溫度及 OH 最大值的位置亦往徑向移至 r = 5 mm 處，此處之火焰最高溫度為 2321 K，且其出現的徑向位置與 OH 的峰值重合。由實驗量測與數值計算之結果相互比較，吾人發現計算之溫度及組成份濃度分布趨勢與實驗結果非常吻合。

圖 25 為高度 x = 50 mm 處之實驗與計算平均溫度、主要組成份及 OH 質量分率徑向分布比較圖，在此高度噴流中心溫度已達到 1970 K，同時 H_2 之質量分率亦已降低至 0.006，最高溫度及 OH 最大值的位置由外往噴流中心移至 r = 3.4 mm 處，此處之火焰最高溫度為 2043 K，且其出現的徑向位置與 OH 的峰值重合。由實驗量測與數值計算之結果相互比較，吾人發現計算之溫度及組成份濃度分布趨勢與實驗結果非常吻合。

圖 26 為沿著噴流中心之實驗與計算平均溫度、主要組成份及 OH 質量分率軸向分布比較圖，實驗量測之最高溫度及 OH 最大值發生在高度約 55 mm 處，這個位置非常接近火焰完全燃燒之高度，同時除了計算之 OH 濃度稍微偏低之外，其他如溫度及主要組

成份濃度之計算結果與實驗數據相當吻合。

由以上的實驗與數值模擬比較結果可知，數值模擬所採用之 Miller 及 Bowman 之化學反應機制結合完整的分子傳輸性質計算以及考慮較輕分子的熱擴散可準確的預測 Re = 330 之層流氫氣擴散火焰，接下來吾人將針對 Re = 30 之較小火焰進行討論。

5-4.2 雷諾數 30 火焰之實驗與計算模擬比較

當微管出口雷諾數降為 30 時，火焰形狀呈現雞蛋型且高度也降至約 7 mm (如圖 19 所示) 。圖 27-29 為 Re = 30 時三個不同高度(x = 0.1, 1, 3 mm)之量測與數值模擬平均溫度及組成份濃度(O_2, N_2, H_2O, OH)徑向分布比較圖，量測數據係以符號表示，而計算結果則以線條表之。圖 27 為高度 x = 0.1 mm 處之實驗與計算平均溫度、主要組成份及 OH 質量分率徑向分布比較圖，由圖中可見噴流中心之溫度已因火焰包覆微管出口而預熱燃料溫度至約 500 K，之後火焰溫度提升至 1910 K，而且火焰最高溫度與 OH 濃度最大值同時出現在 r =2 mm 處，也就是接近 H_2 及 O_2 完全燃燒處。而在此高度因仍處噴流勢流錐，故噴流中心之 H_2 尚未開始反應，而稍微消耗之 H_2 乃是因為微管預熱而造成 H_2 快速往徑向方向擴散所致。由實驗量測與數值計算之結果相互比較，吾人發現計算之溫度及組成份濃度分布趨勢與實驗結果非常吻合，只是計算結果得到較窄的反應區。

圖 28 為高度 x = 1 mm 處之實驗與計算平均溫度、主要組成份及 OH 質量分率徑向分布比較圖，在此高度 N_2 已擴散到噴流中心，同時最高溫度及 OH 最大值的位置亦往徑向移至 r = 2.4 mm 處，此處之火焰最高溫度為 2024 K，且其出現的徑向位置與 OH 的峰值重合。而噴流中心之溫度亦以提升至 832 K，同時 H_2 的消耗以及 H_2O 的增加顯示噴流中心已開始燃燒。由實驗量測與數值計算之結果相互比較，吾人發現計算之溫度及組成份濃度分布趨勢與實驗結果非常吻合，只是計算結果得到較窄的反應區。

圖 29 為高度 x = 3 mm 處之實驗與計算平均溫度、主要組成份及 OH 質量分率徑向分布比較圖，在此高度噴流中心溫度已達到 1780 K，同時 H_2 亦已接近消耗完畢，最高溫度及 OH 最大值的位置亦往徑向方向內移至 r = 1.2 mm 處，此處之火焰最高溫度為 2078 K，且其出現的徑向位置與 OH 的峰值重合。由實驗量測與數值計算之結果相互比較，吾人發現計算之最高溫度及 OH 最大值的位置與實驗結果相差約 1.4 mm，顯示在此高度計算結果仍預測較寬之火焰，但由圖 21 之二維 OH 螢光分布量測結果吾人發現在此高度 OH 已擴散到噴流中心，定量之拉曼散射與 OH 誘發螢光量測之最高溫度及 OH 最大值的位置與二維 OH 螢光分布量測結果相當吻合。由此可見雖然數值模擬已考慮熱擴散效應但使用 Miller 及 Bowman 之反應機制其預測火焰位置仍偏離實驗結果，因此，其他化學反應機制仍是值得嘗試。

5-5 管徑 0.2 及 0.48 mm 噴流氫氣火焰之照相及二維 OH 激發螢光量測

為了能正確計算噴流出口速度以及提供管徑尺寸及厚度給數值模擬比對之用，吾人利用顯微鏡所量測之微管內徑為 0.48 及 0.2 mm 其厚度分別為厚度為 0.17 及 0.09 mm 之微管顯微照相如圖 30 所示。氫氣經由微管噴出之後，與靜止之大氣進行燃燒，形成一層流擴散火焰，兩種不同管徑之噴流火焰操作條件如表 2 所示。管徑 0.2 及 0.48 mm 噴流氫氣火焰之照相及二維 OH 激發螢光影像如圖 31 所示，此兩火焰之雷諾數皆為 30。由於氫氣火焰之亮度不高，因此直接照相係以長時間曝光之 CCD 照相機取相並於鏡頭前加裝放大鏡。照片顯示兩種火焰皆成雞蛋形狀，並包覆微管出口，黃顏色的管子係因火焰加熱所致，利用紅外線照相機量測管徑 0.2 及 0.48 mm 之管壁溫度分別為 943 及 1017 K。而對應於這兩種火焰之單脈衝 OH 影像亦置於圖 31 之下方，同時 OH 影像係從離微管上方 0.1 mm 處拍攝以避免雷射光造成之 Mie 散射，由於 OH 螢光強度在火焰前緣達到最大值，因此所量測之二維 OH 影像代表反應區的形狀。對管徑 0.48 mm 之火焰而言，OH 影像分布之形狀與照片所拍攝之火焰形狀非常相似，但是當管徑降為 0.2 mm 時，其 OH 影像分布之形狀與照片所拍攝之火焰形狀不同，而成半徑約 1 mm 之球型，這個結果說明了直接照相可能會誤判火焰真正的反應區。而研究 C_2 碳氫火焰之文獻報告指出，當火焰呈球狀時，其處於對流－擴散控制區域，當下一節討論拉曼散射量測結果實無人將進一步檢視本研究之微火焰是否處於對流－擴散控制區域。

5-6 管徑 0.2 及 0.48 mm 之微火焰之熱物性質

圖 32-34 為管徑 0.2 mm 火焰在三個不同高度(x = 0.1, 1, 2 mm)之量測與數值模擬平均溫度及組成份濃度(O_2, N_2, H_2O, OH)徑向分布比較圖，同時實驗量測之混合分率亦畫在圖中，量測數據係以符號表示，而計算結果則以線條表之。圖 32 為高度 x = 0.1 mm 處之實驗與計算平均溫度、主要組成份及 OH 質量分率徑向分布比較圖，由圖中可見火焰溫度從噴流中心快速提升至 1786 K 並平坦的通過反應區，然後當通過火焰外端之後溫度陡降，而噴流中心所量測到之 O_2 及 N_2 顯示外界空氣已進入噴流中心，吾人研判造成空氣進入噴流中心可能是因火焰包覆管壁，火焰一方面加熱管壁至 943 K，一方面火焰被管壁熄滅，而在管避雨火焰之間產生空隙所致。文獻亦指出外界空氣可能經由此空隙捲入火焰，進而改變燃燒狀態[36]。事實上滲入噴流中心的空氣已被預熱至 400 K，而且沒有量測到 H_2O 及 H_2，在如此靠近噴嘴出口量測不到 H_2 有別於一般層流火焰，吾人檢查高度 0.1 mm 處橫切面之 H_2 平均光譜，發現在噴流中心之 H_2 最大積分強度與平面火焰當量比介於 1.05-1.2 之間的光譜強度相當，也就是相當於 0.065 之 H_2 莫爾分率，而量測 H_2 之實驗誤差也有可能造成量測之混合分率往貧油方向偏移，由實驗量測誤差加上微管預熱增強 H_2 熱擴散以及外界空氣漏入噴流中心等因素可能是造成量測不到 H_2 的原因。除此之外，計算所得由管壁傳至氫燃料之熱傳率為 57 W，而要將 H_2 溫度由 298 K 提升至 400 K 僅需 0.045 W 的熱，此計算結果說明了大部分的熱是透過傳導由管子帶

走，而不是用來啟動管內或管外之燃燒反應。在高度 0.1 mm 處有兩個 OH 峰值各出現在 r = 0.45 及 1.15 mm 處，這表示有兩個反應區出現在這個高度，也說明了這火焰結構與一般層流氫氣擴散火焰不同。由實驗量測與數值計算之結果相互比較，吾人發現計算之溫度及組成份濃度分布趨勢與實驗結果相似，但數值模擬無法預測空氣捲入以致低估噴流中心之 O_2 及 N_2 濃度。而數值模式假設壁溫為 300 K 以及使用的化學反應模式與簡化的傳輸模型都有可能造成 H_2 的高估，吾人曾嘗試假設管壁預熱的邊界條件，但計算的結果並無太大的改善。Mosbacher 等人[37]發現火焰曲率聚焦可加速 H_2 擴散，而且所使用之化學反應機制與分子傳輸資料對火焰結構非常敏感，因此，在模擬微火焰時較輕組成份之熱擴散以及其他化學反應機制與傳輸資料或許必須加以考慮。

圖 33 及 34 分別為高度 x = 1 及 2 mm 之量測與數值模擬平均溫度及組成份濃度(O_2, N_2, H_2O, OH)徑向分布比較圖，在這兩個高度溫度分布皆呈鐘罩型，而其平均溫度分別為 1650 及 1600 K，同時兩個 OH 峰值在 x = 1 mm 已交會成一個，此結果顯示反應區的改變，而噴流中心的燃燒反應也造成 H_2O 的增加及 O_2 與 N_2 的減少。比較數值計算與實驗量測之結果發現，計算之溫度及組成份濃度分布趨勢與實驗結果相似，但高溫度的預測結果導致 H_2O 及 OH 的高估以及低估 O_2 與 N_2。

當管徑增加到 0.48 mm 時, 在三個不同高度(x = 0.1, 1, 2 mm)之量測與數值模擬平均溫度及組成份濃度(O_2, N_2, H_2O, OH)徑向分布比較圖如圖 35-37 所示，而這個火焰除了比管徑 0.2 mm 之火焰稍大之外, 其餘溫度及組成份濃度分布趨勢皆與其相似。在 x = 0.1 mm 處，噴流中心溫度(T = 784 K)及反應區溫度(T = 1780 K)皆比同高度之管徑 0.2 mm 之火焰要高，噴流中心的高溫度顯示大量的熱從火焰傳至捲入的空氣及管壁，而計算所得由管壁傳至氫燃料之熱傳率為 111 W, 但要將 H_2 溫度由 298 K 提升至 784 K 僅需 0.543 W 的熱，此計算結果再次說明了大部分的熱是透過傳導由管子帶走，而不是用來啟動管內或管外之燃燒反應，同時預熱捲入空氣導致火焰溫度及 OH 濃度的增加。在高度 0.1 mm 處有兩個 OH 峰值各出現，這表示有兩個反應區出現在這個高度。數值計算與實驗的比較結果發現，數值計算預測較寬的火焰及較高的溫度與 OH 濃度。

由以上對微火焰完整的定量量測無人發現幾個重要特徵，首先，空氣捲入噴流中心及 H_2 的消失聯合效應導致整個火焰處於貧油燃燒狀態，再則火焰包覆微管顯示分子擴散－傳輸機制將比浮力效應更主控火焰。由 Ban 等人[9]所建議之簡單計算方式將用來檢驗本研究之火焰是處於對流－擴散控制或是浮力控制區域。Ban 等人研究 C_2 碳氫燃料火焰指出，當平均出口速度，u_e (體積流率/噴嘴截面積)，與擴散速度，$u_D = D/l_D$ (D 是質量擴散係數，l_D 火焰特徵擴散長度)的比值小於 5 時，火焰呈球型。對本研究之氫氣火焰而言，l_D 定義為在 x = 0.1 mm 處從內管壁至第一個 OH 峰值的擴散長度，特徵擴散時間，t_D，是 l_D 與 u_D 之比值，所計算之特徵性質如表 3 所列。計算結果顯示，這兩個火焰之 Fr 值都很大，因此浮力效應可以忽略，同時因為 Peclet 數低，所以火焰係處於對流－擴散控制區域。值得一提的是，管徑 0.2 mm 之球型火焰的 Peclet 數為管徑 0.48 mm 之雞蛋型火焰的 7 倍，這個結果顯示，當火焰處於對流－擴散控制區域，Peclet 數對火焰形

狀的影響不大。

第六章 結論

本子期計畫乃是改良現有之紫外光拉曼散射及雷射誘發預解離螢光系統，使其具有更佳之空間解析度，以量測微管噴流火焰。為了避免聚焦後微小焦點造成空氣及火焰組成份尤其是 H_2O 解離，吾人利用冷 CO_2 及 CH_4 噴流以及平面氫氣火焰先進行解析度與雷射能量控制之光譜量測，以確認改良後之雷射系統可用來量測微噴流火焰。除本報告之研究成果之外，本雷射系統亦已成功的量測微觸媒管反應後之溫度及組成份濃度，並已發表在國際著名之 Combustion Science and technology 期刊[38]。

針對管徑 1 mm、雷諾數 330 之噴流氫氣擴散火焰研究結果顯示，此火焰屬於一般層流擴散火焰，在 x = 1 mm 處噴流中心仍處於勢流錐，H_2 尚未開始反應，而反應區出現在最高溫度與最大 OH 峰值之混合層。隨著越往火焰下游噴流中心逐漸反應，整個火焰高度約為 60 mm。數值模擬採用 Miller 及 Bowman 之氫氧化學反應機制及完整的傳輸性質計算，並考慮組成份之熱擴散效應的計算結果顯示，除了在 x = 1 及 5 mm 處預測較窄的火焰之外，溫度及組成份濃度的預測與實驗數據非常接近，這也顯示 Miller 及 Bowman 之氫氧化學反應機制可成功的預測一般層流擴散火焰。當雷諾數降為 30 時，火焰不但縮小而且呈雞蛋形狀，整個火焰高度約為 7 mm。實驗量測顯示，在 x = 0.1 mm 處由於微管受到火焰預熱之影響，H_2 已快速往外擴散，同時微量的 N_2 也已擴散至噴流中心，火焰反應區出現在燃料與外界空氣之混合層，整體而言，此火焰的最高溫度比雷諾數 330 之火焰溫度要低。數值模擬除了預測 x = 3 mm 處有較寬之火焰之外，溫度及組成份濃度的預測與實驗數據非常接近。

對於管徑 0.2 及 0.48 mm、雷諾數 30 之兩個火焰而言，量測結果顯示，外界空氣捲入噴流中心，造成整個火焰呈現貧油燃燒狀態，實驗結果亦證明這兩個火焰係處於對流－擴散控制區域。比較數值計算與實驗量測之結果發現，計算之溫度及組成份濃度分布趨勢與實驗結果相似，但數值計算預測較寬的火焰及較高的溫度與 OH 濃度，此結果顯示數值模擬無法預測空氣捲入以致低估噴流中心之 O_2 及 N_2 濃度，同時使用的簡化傳輸模式及化學反應機制似乎無法正確模擬微型火焰。因此，在模擬微火焰時較輕組成份之熱擴散以及其他化學反應機制與傳輸資料或許必須加以考慮。

參考文獻

[1] Feynman, R. P., 1992, "There's Plenty of Room at the Bottom," *J. of Microelectromechanical Systems*, Vol. 1, No. 1, pp. 60-66.

[2] Feynman, R. P., 1993, "Infinitesimal Machinery," *J. of Microelectromechanical Systems*, Vol. 2, No. 1, pp. 4-14.

[3] Ho, C.-M. and Tai, Y.-C., 1998, "Micro-Electro-Mechanical-Systems (MEMS) and Fluid Flows," *Annu. Rev. Fluid Mech.*, Vol. 30, pp. 579-612.

[4] Shih, J.-C., Ho, M.-C., Liu, J., and Tai, Y.-C., 1996, "Monatomic and Polyatomic Gas Flow Through Uniform Microchannels," *ASME DSC* 59:197-203.

[5] Hasegawa, T., Suganuma, M., and Watanabe, H., 1997, "Anomaly of Excess Pressure Drops of the Flow Through very Small Orifices," Phys. Fluids, Vol. 9, pp. 1-3.

[6] http://sec353.jpl.nasa.gov/apc/Micropropulsion/00.html.

[7] http://www.lerc.nasa.gov/WWW/Rt1996/5000/5330sc.html.

[8] G. T. A. Kovacs, *Micromachined transducers-source book*. McGraw-Hill, New York, 1998.

[9] H. Ban, S. Venkatesh, K. Saito, J. Heat Transfer 116 (1994) 954-959.

[10] T. Ida, M. Fuchihata, Y. Mizutani, *Microscopic Diffusion Structures with Micro Flames*. Proc. 3rd International Symposium on Scale Modeling, ISSM3-E3, 2000.

[11] L. M. Matta, Y. Neumeier, B. Lemon, B. T. Zinn, *Proc. Combust. Inst.* 29 (2002) 933-939.

[12] Y. Nakamura, H. Ban, K. Saito, T. Takeno, *Structures of Micro (Millimeter Size) Diffusion Flames*. Proc. 3rd International Symposium on Scale Modeling, ISSM3-E7, 2000.

[13] Y. Nakamura, A. Kubota, H. Yamashita, K. Saito, *Numerical Study on Methane Micro-Diffusion Flames*. Proc. 19th International Colloquium on the Dynamics of Explosion and Reactive Systems, Paper No. We2-2-1(#105), 2003.

[14] Y. Nakamura, A. Kubota, H. Yamashita, K. Saito, *Near Extinction Flame Structure of Micro-Diffusion Flames*. Proc. International Symposium on Micro-Mechanical Engineering, ISMME2003-11, 2003.

[15] Shih, J. C., Ho, C. M., Liu, J. and Tai, Y. C., 1995, "Non-linear pressure distribution in uniform microchannels," *ASME AMD-MD 238*.

[16] Lahiji, G. R. and Wise, K. D., 1980, "A monolithic thermopile detector fabricated using integrated-circuit technology," *Proc. Int. Electron Dev. Meet*. Washington, D. C. pp. 676-679, New York.

[17] Eckbreth, A. C., *Laser Diagnostics for Combustion Temperature and Species*, Energy and Engineering Science Series, (Gupta, A. K. and Lilley, D. G. ed.), Abacus Press, Cambridge, 1988, Vol. 7.

[18] Andresen, P., Meijer, G., Schluter, H., Voges, H., Koch, A., hentschel, W., Oppermann, W., and Rothe, E., "Fluorescence Imaging Inside an Internal Combustion Engine Using Tunable Excimer Laser, " *Appl. Opt.*, Vol. 29, pp. 2392-2404, 1990.

[19] Herzberg, G., (1950), *Molecular Spectra and Molecular Structure-Part I.- Spectra of diatomic Molecules*, 2nd ed., D. Van Nostrand Company Inc., Princeton, New Jersey, Chapter 2, Section 2(e) and 2(f).

[20] Long, D. A., (1977), *Raman Spectroscopy*, McGraw-Hill, New York, NY.

[21] Cheng, T. S., Yuan, T., Chao, Y.-C., Lu, C.-C. and Wu, D.-C. (1998b) Premixed methane-air flame spectra measurements using UV Raman scattering. *Combust. Sci. and Tech.*, **135**, 65-84.

[22] Dibble, R. W., Masri, A. R. and Bilger, R. W. (1987) The spontaneous Raman

scattering technique applied to nonpremixed flames of methane. *Combust. Flame*, **67**, 189-206.

[23] Cheng, T. S., Wehrmeyer, J. A., and Pitz, R. W., (1992). Simultaneous temperature and multi-species measurements in a lifted hydrogen diffusion flame. *Combust. Flame*, **91**, pp. 323-345.

[24] Cheng, T. S., Wehrmeyer, J. A., Pitz, R. W., Jarrett, O., and Northam, G. B., (1994). Raman measurement of mixing and finite-rate chemistry in a supersonic hydrogen-air diffusion flame. *Combust. Flame*, **99**, pp. 157-173.

[25] Nandula, S. P., Brown, T. M., Skaggs, P. A., Pitz, R. W. and DeBarber, P. A. (1994) Multi-species line Raman measurements in H_2-air turbulent flames. *Thirty-second Aerospace Sciences Meeting and Exhibit*, Reno, NV, AIAA-94-0227.

[26] Chen, Y.-C., Peters, N., Schneemann, G. A., Wruck, N., Renz, U., and Mansour, M. S., (1996). The detailed flame structure of highly stretched turbulent premixed methane-air flames. *Combust. Flame*, **107**, pp. 223-244.

[27] Andresen, P., Bath, A., Gröger, W., Lülf, H. W., Meijer, G., and ter Meulen, J. J., (1988). Laser-induced fluorescence with tunable excimer lasers as a possible method for instantaneous temperature field measurements at high pressure: checks with an atmospheric flame. *Appl. Opt.* **27**, 365-378.

[28] Chen, Y.-C. and Mansour, M. S., (1996). Measurements of the detailed flame structure in turbulent H_2-Ar jet diffusion flames with line-Raman/Rayleigh/LIPF-OH technique. *Proceedings of the Combustion Institute*, **26**, 97-103.

[29] E. Gutheil, G. Balakrishnan, F. A. Williams, in: N. Peters, B. Rogg, (Eds.), *Reduced Kinetics Mechanisms for Applications in Combustion System*, Springer-Verlag, New York, 1993, pp. 177-195.

[30] R., J. Kee, F. M. Rupley, A. J. and Miller, *The CHEMKIN Thermodynamic Database*, Report No. SAND87-8215, Sandia National Laboratories, 1987.

[31] M. D. Smooke, *Reduced Kinetic Mechanisms and Asymptotic Approximations for Methane-Air Flames*, Lecture Notes in Physics, Vol. 384, Springer-Verlag, New York, 1991, pp. 1-28.

[32] http://www.ca.sandia.gov/TNF/radiation.html.

[33] S. V. Patankar, *Numerical Heat Transfer and Fluid Flow*, McGraw-Hill, New York, 1980.

[34] Chen, C. J. and Rodi, W. (1980), *Vertical Turbulent Buoyant jets. A Review of Experimental Data*, Pergamon press, new York.

[35] 廖仁瑞，"微機電技術製作之白金觸媒反應系統"，國立成功大學航太工程學系碩士論文(2002)。

[36] K. Saito, A. S. Gordon, F. A. Williams, Combust. Sci. Tech., 47 (1986) 117-138.

[37] D. M. Mosbacher, J. A. Wehrmeyer, R. W. Pitz, C.-J. Sung, J. L. Byrd, *Proc. Combust. Inst.* 29 (2002) 1479-1486.

[38] Y.-C. Chao, J.-R. Hsu, C.-Y. Wu, G.-B. Chen, T.-S. Leu, and T. S. Cheng, (2004) "Operational Characteristics of Catalytic Micro-Combustion in a Platinum Microtube," *Combust. Sci. and Technol*, Vol. 176, No. 10, pp. 1755-1777.

[39] Miller, J. A. and Bowman, C. T., Mechanism and Modeling of Nitrogen Chemistry in Combustion, Prog. in Energy and Combustion Science, 1989, Vol. 15, pp287-338.

[40] T. S. Cheng, Y.-C. Chao, C.-Y. Wu, G.-B. Chen, T. Yuan, and T. S. Leu, "Preliminary Study of Micro Reacting System Using Laser Diagnostic Techniques," Presented at the Proceedings of the 13th National Conference on Combustion Science and Technology, Taipei, Taiwan, March 29, 2003, NSC-90-2212-E-216-019.

[41] T. S. Cheng, Y.-C. Chao, C.-Y. Wu, G.-B. Chen, T. Yuan, and T. S. Leu, "Raman-LIPF Measurements of Temperatures, Major Species, and OH in a Laminar

Hydrogen Jet Diffusion Flame," Presented at the Proceedings of the 13th National Conference on Combustion Science and Technology, Taipei, Taiwan, March 29, 2003, NSC-90-2212-E-216-019.

[42] T. S. Cheng, Y.-C. Chao, C.-Y. Wu, G.-B. Chen, T. Yuan, and T. S. Leu, "Experimental and Numerical Study of a Laminar Nonpremixed Hydrogen Flame," Presented at the 19th International Colloquium on the Dynamics of Explosions and Reactive Systems, Hakone, Japan, July 28~August 1, 2003, NSC-90-2212-E-216-019.

[43] T. S. Cheng, Y.-C. Chao, C.-Y. Wu, G.-B. Chen, T. Yuan, and T. S. Leu, "UV Raman/LIPF Diagnostics in a Mesoscale Nonpremixed Hydrogen Jet Flame," 2003**年中國航空太空學會/中華民用航空學會學術研討會暨國科會航太學門研究成果發表會**, Tainan, December 19, 2003, NSC-91-2212-E-216-010.

[44] T. S. Cheng, Y.-C. Chao, C.-Y. Wu, Y.-H. Li, K.-Y. Lee, T. Yuan, and T. S. Leu, "Characteristics of Hydrogen Microflames," Presented at the 14th Annual National Conference on Combustion, Chung-Li, Taiwan, March 27, 2004, NSC 92-2212-E-216-001.

[45] T. S. Cheng, Y.-C. Chao, C.-Y. Wu, Y.-H. Li, Y. Nakamura, K.-Y. Lee,T. Yuan, and T. S. Leu, (2004) "Experimental and Numerical Investigation of Microscale Hydrogen Diffusion Flames," Presented at the *30th Symposium (International) on Combustion*, The Combustion Institute, Chicago, USA, July 25-30, 2004.

表 1 兩種不同雷諾數之噴流火焰操作條件

D (mm)	Thickness (mm)	Flowrate (cc/min)	Mass flowrate (mg/s)	Velocity (m/s)	Reynolds number	Measured tube wall temperature (K)
1	0.17	1696.5	2.336	36	330	703
1	0.17	155.37	0.214	3.3	30	803

表 2 兩種不同口徑之噴流火焰操作條件

D (mm)	Thickness (mm)	Flowrate (cc/min)	Mass flowrate (mg/s)	Velocity (m/s)	Reynolds number	Measured tube wall temperature (K)
0.2	0.17	31.07	0.043	16.48	30	943
0.48	0.09	77.68	0.107	7.16	30	1017

表 3 計算之微型火焰特徵及性質

Burner diameter (mm)	0.20	0.48
u_e (m/s)	16.48	7.16
Re	30	30
Fr	1.39×10^{5}	1.09×10^{4}
T_{mea} (K)	1786	1879
l_D (m)	2.6×10^{-4}	9×10^{-5}
D (m^2/s)	6.02×10^{-4}	6.49×10^{-4}
u_D (m/s)	2.32	7.21
t_D (s)	1.12×10^{-4}	1.25×10^{-5}
Pe	7	1

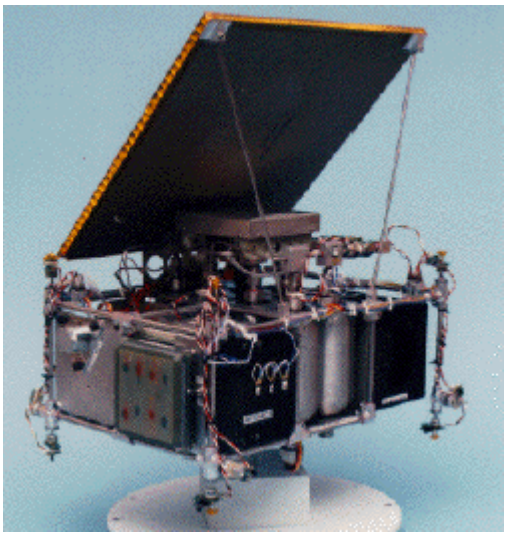

圖 1　MTDII 衛星

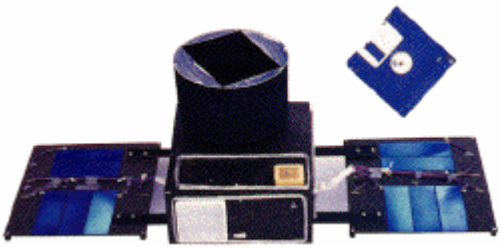

圖 2 Bitsi 衛星

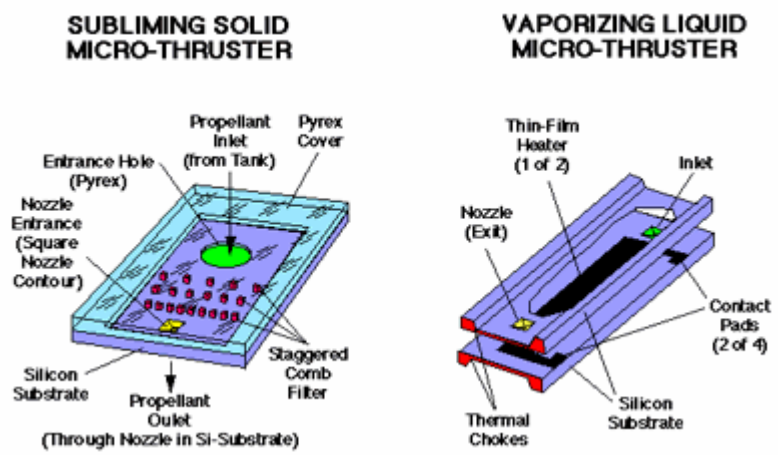

圖 3 昇華固體和汽化液體微推進器

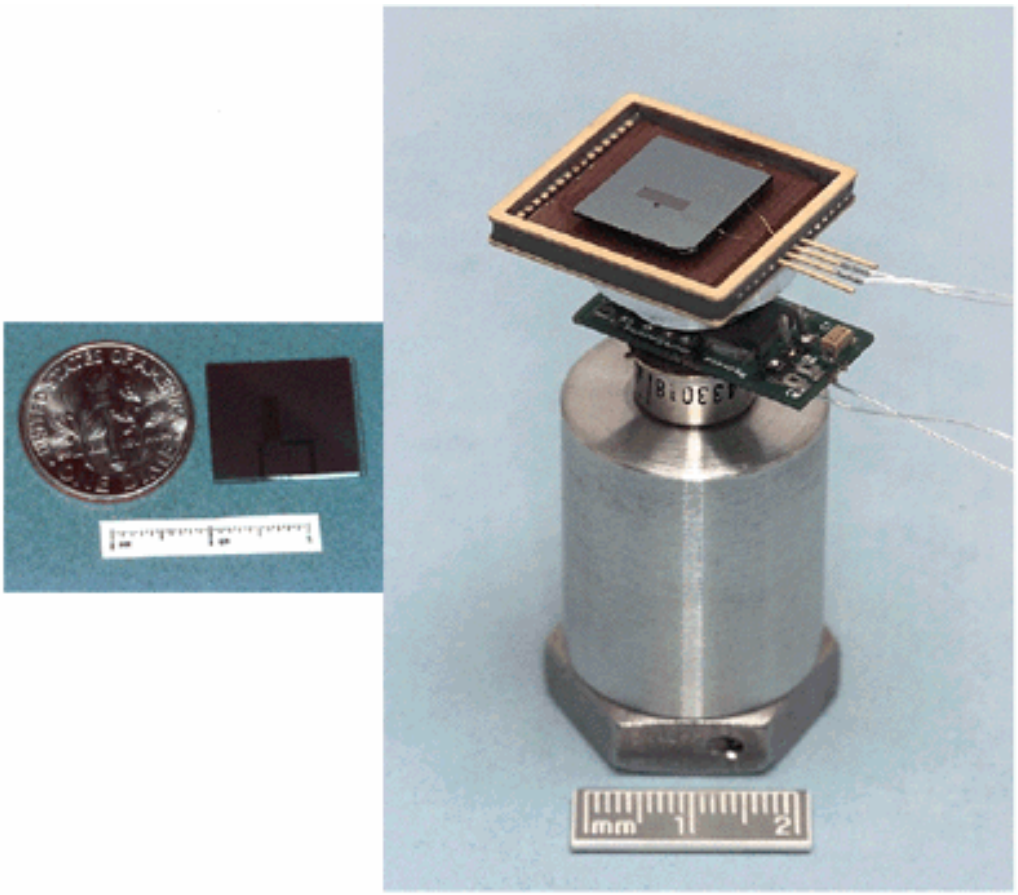

圖 4 晶片型離子推進器

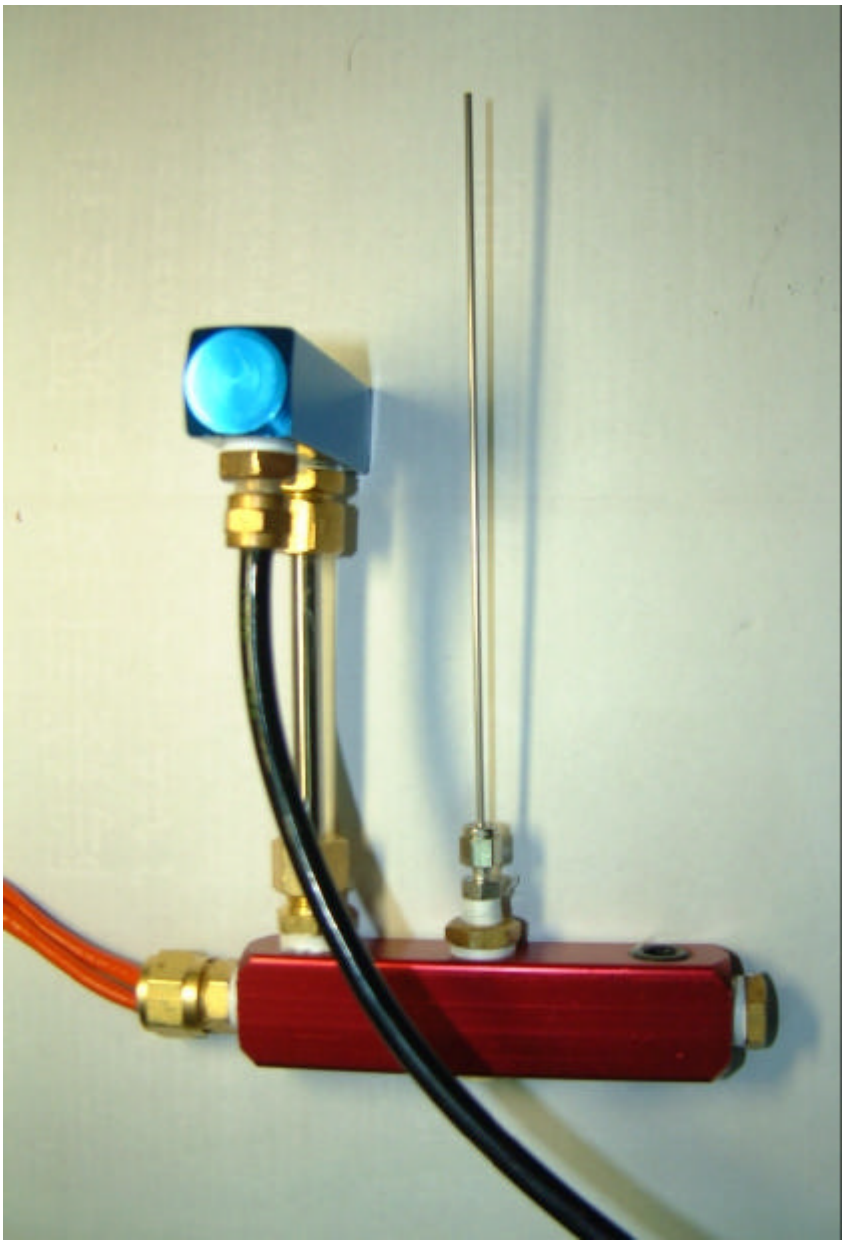

圖 5 **口徑** 1 mm **微管之裝置圖**

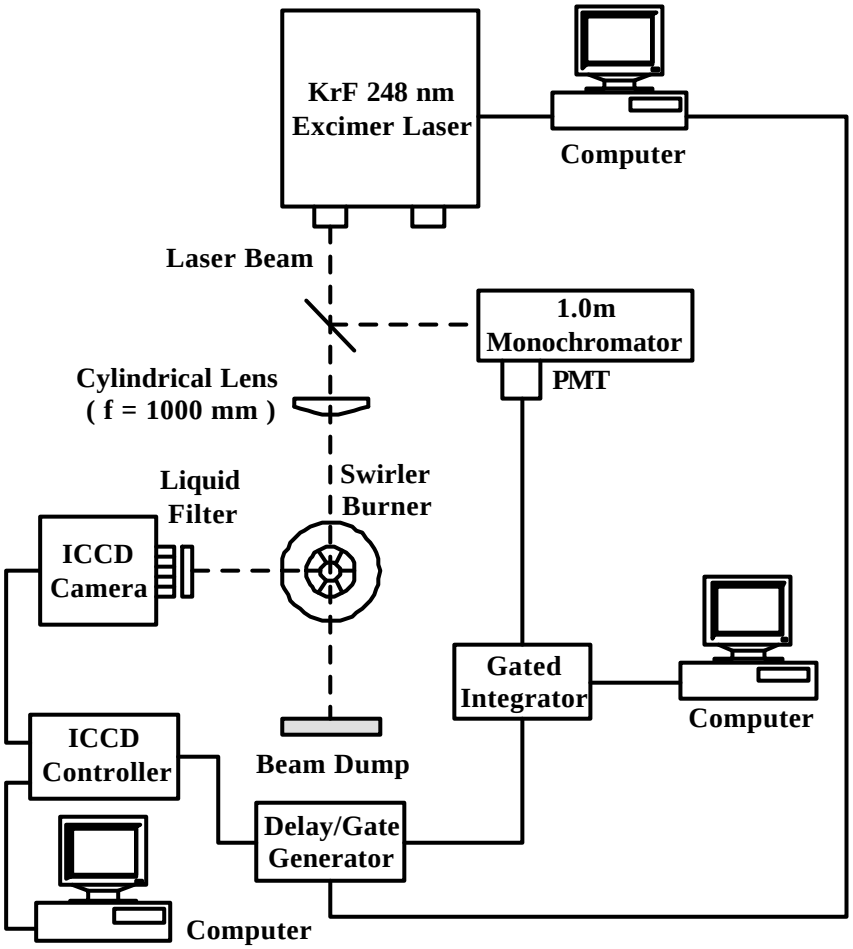

圖 6 二維雷射誘發螢光量測系統

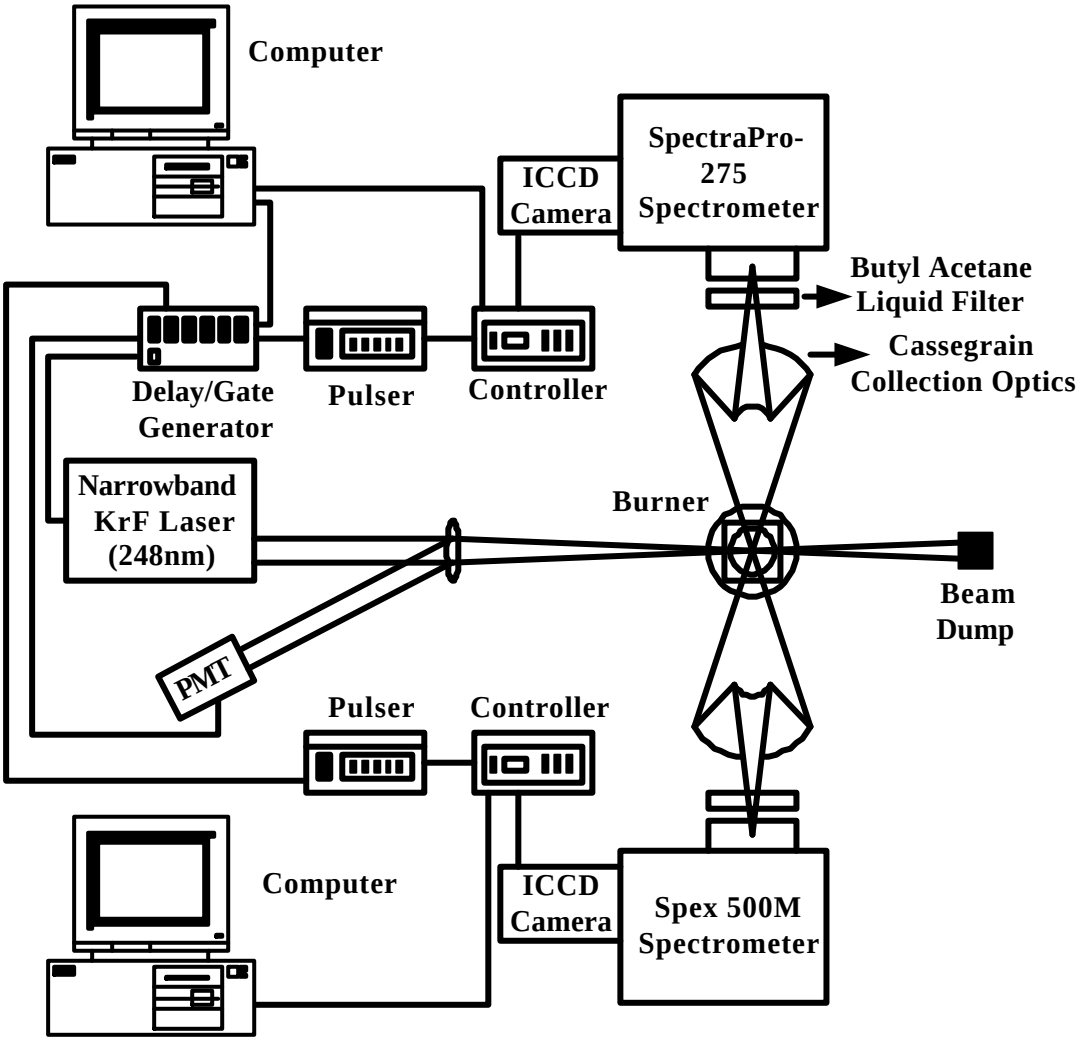

圖 7　UV Raman/LIPF **系統配置圖**

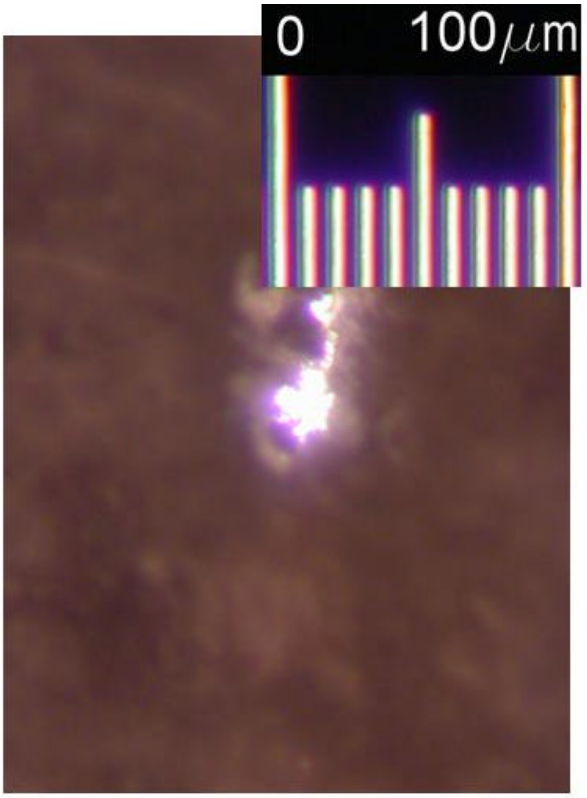

圖 8 雷射光經焦距 200 mm 之鏡片聚焦後之焦點尺寸

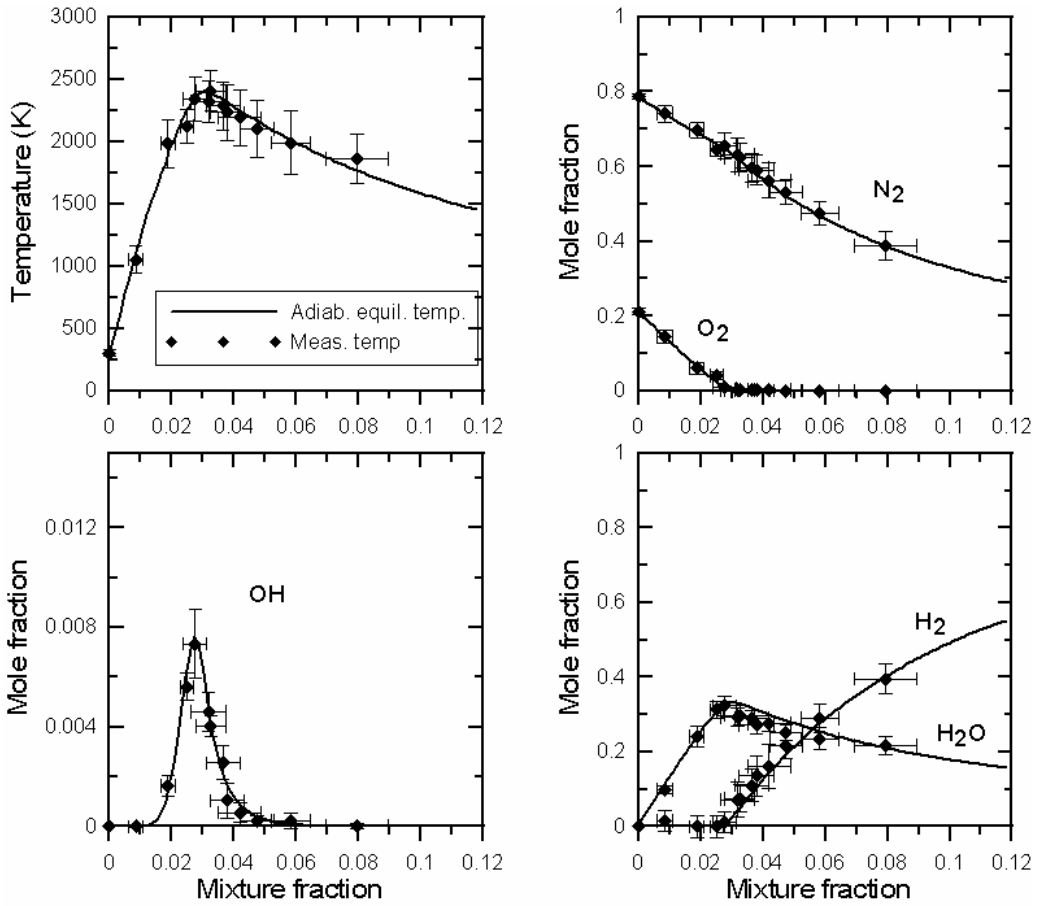

圖 9 平面火焰溫度、主要組成份及 OH 莫爾分率之校正結果

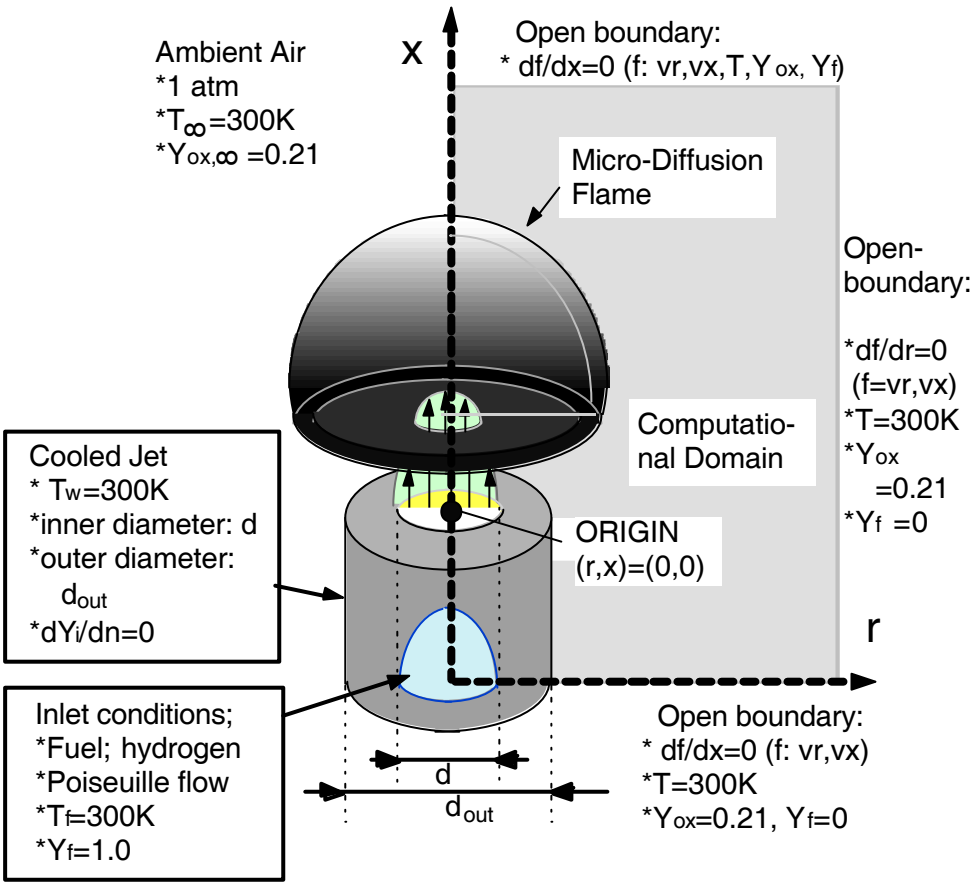
Ambient Air
*1 atm
*T∞=300K
*Yox,∞ =0.21
x
Open boundary:
* df/dx=0 (f: vr,vx,T,Yox, Yf)
Micro-Diffusion Flame
Open-boundary:
*df/dr=0
(f=vr,vx)
*T=300K
*Yox
=0.21
*Yf =0
Computatio-nal Domain
Cooled Jet
* Tw=300K
*inner diameter: d
*outer diameter:
dout
*dYi/dn=0
ORIGIN
(r,x)=(0,0)
r
Inlet conditions;
*Fuel; hydrogen
*Poiseuille flow
*Tf=300K
*Yf=1.0
Open boundary:
* df/dx=0 (f: vr,vx)
*T=300K
*Yox=0.21, Yf=0
d
dout

圖 10 數值計算模型

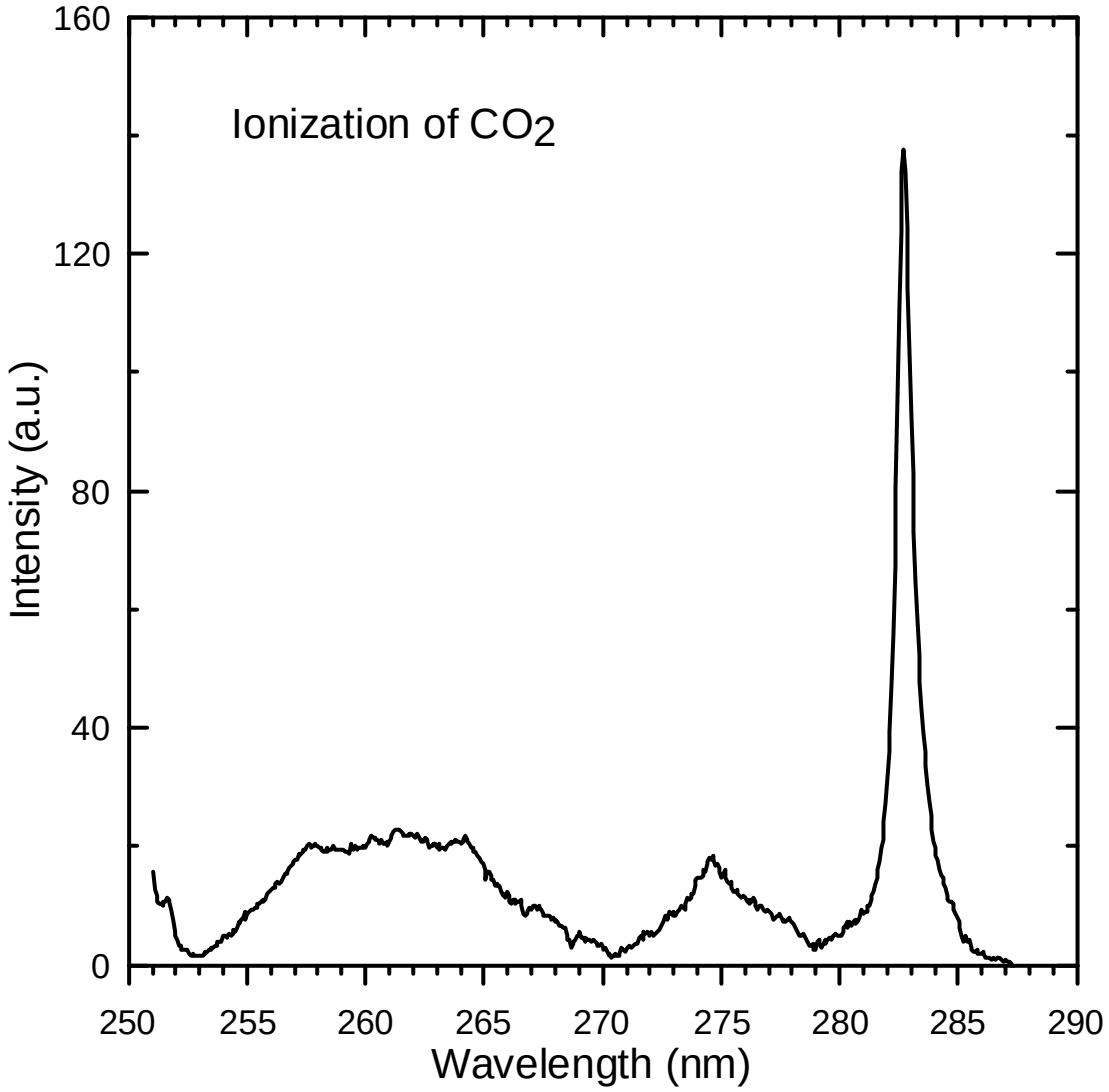

圖 11　CO2 **離子化之後的譜線**

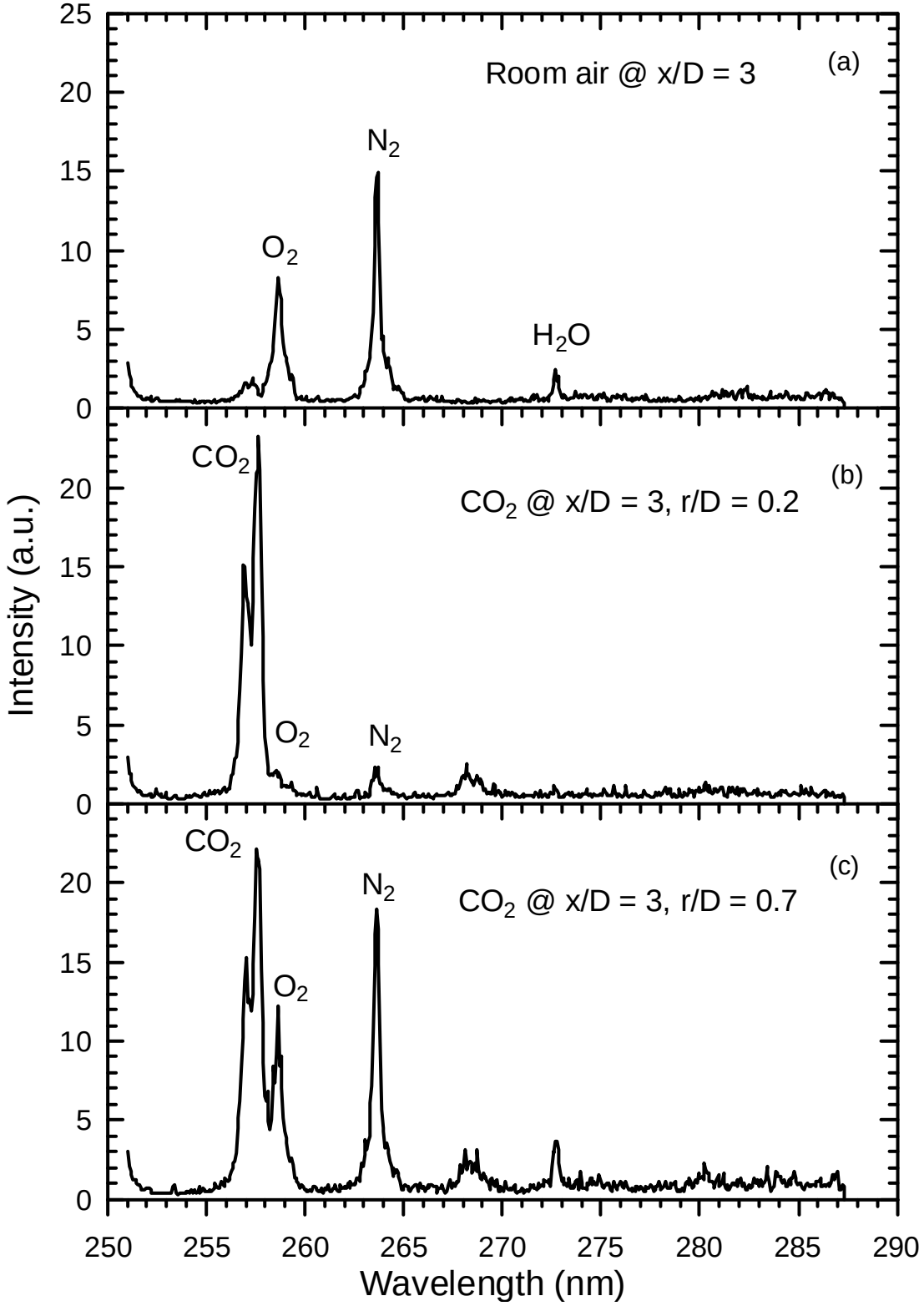

圖 12 **空氣及微管噴流為** CO2 **之拉曼散射光譜**

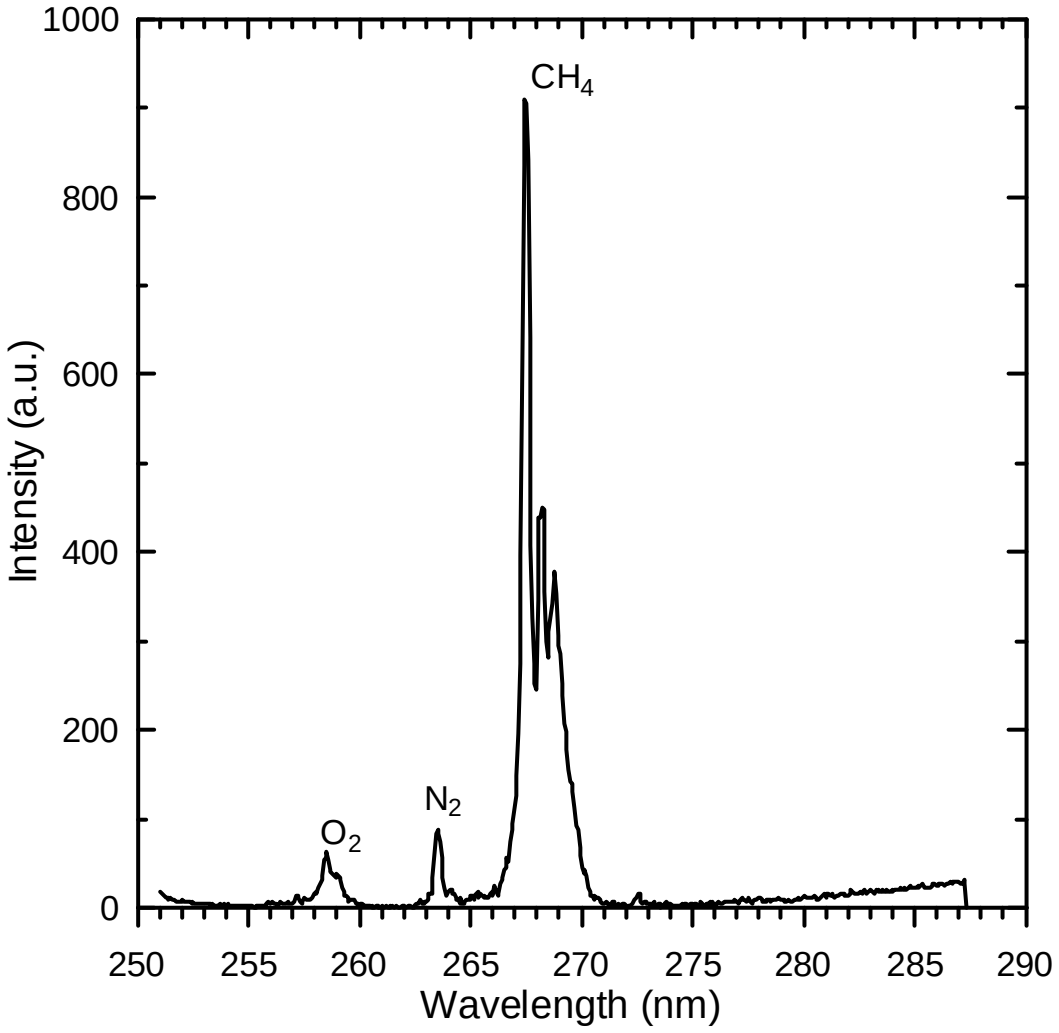

圖 13 微管噴流為 CH4 之拉曼散射光譜

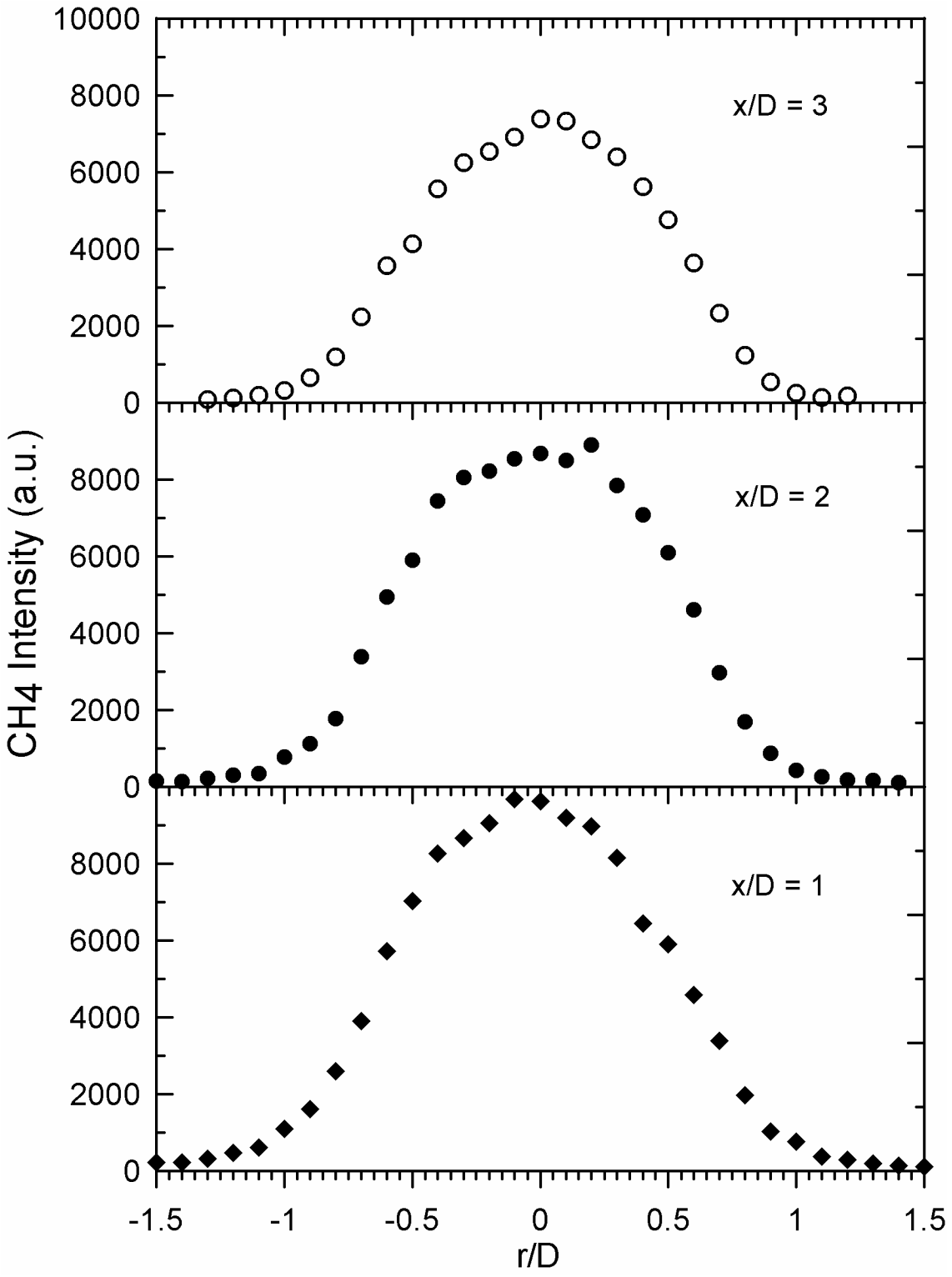

圖 14 在離微管出口 x/D = 1、2、3 處沿著徑向方向之 CH4 濃度分布

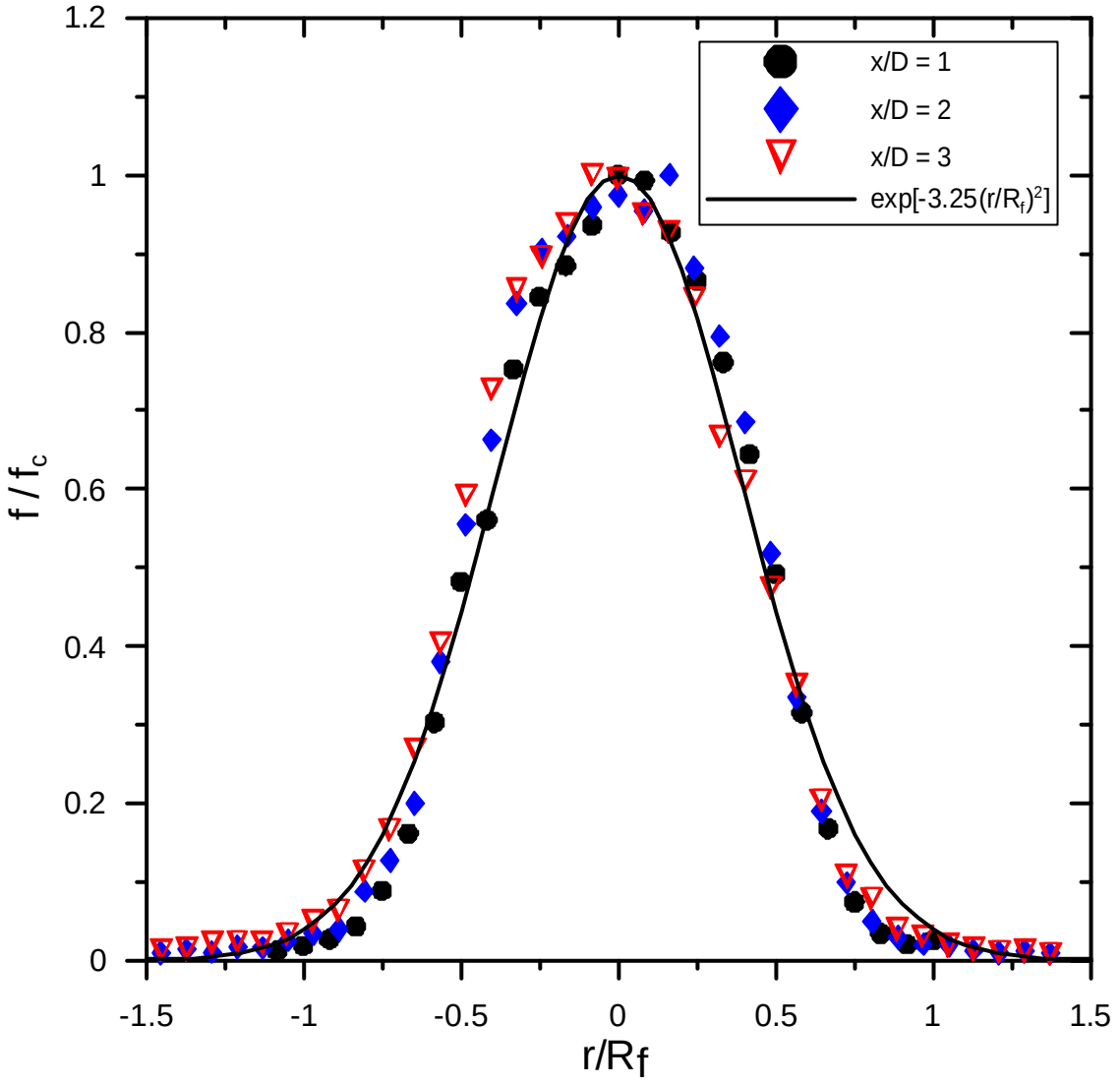

圖 15 在離微管出口 x/D = 1、2、3 處沿著徑向方向歸一化後 CH4 之濃度分布

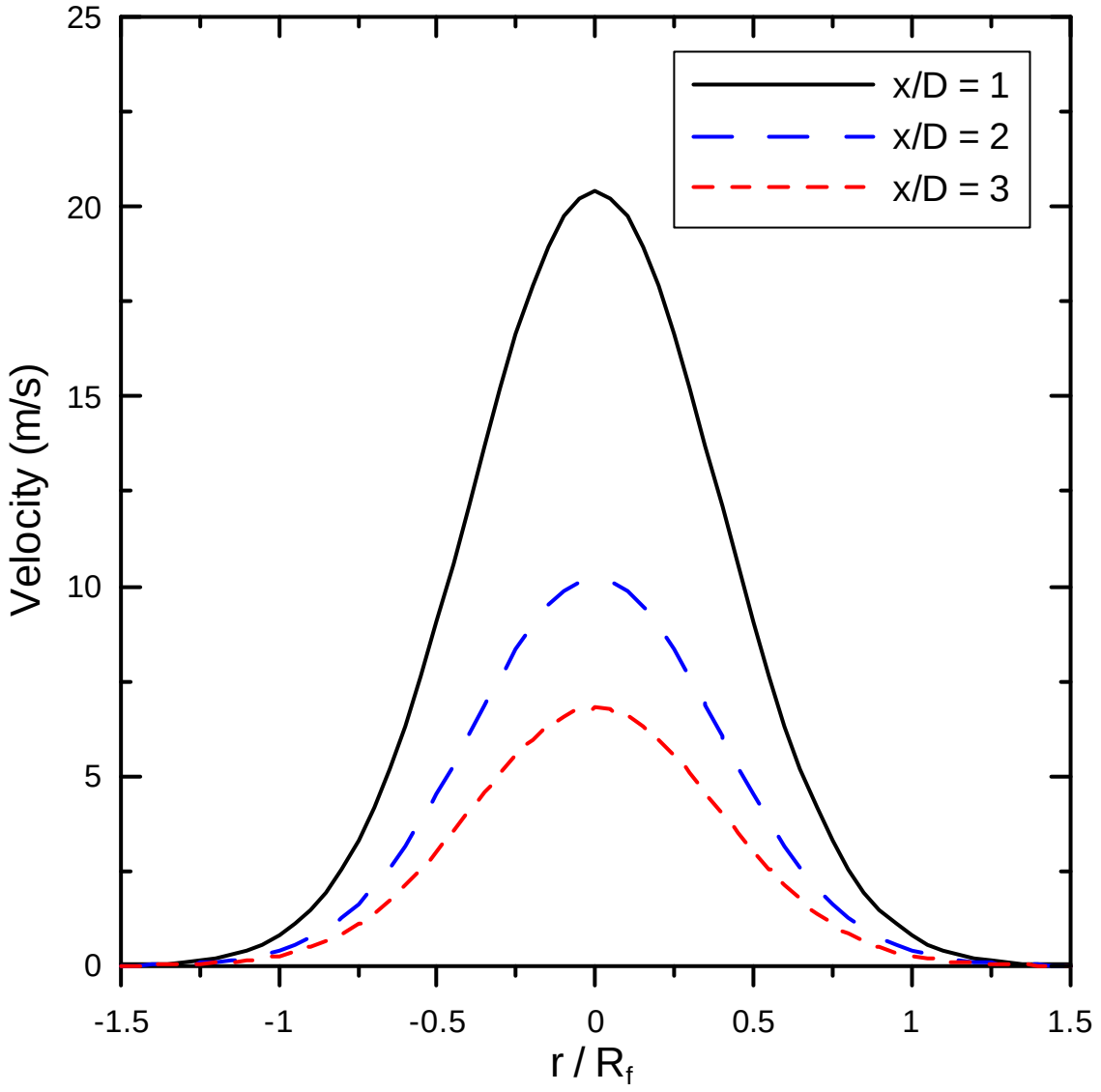

圖 16 利用 CH_4 之濃度分布及自似性所推算出之速度分布

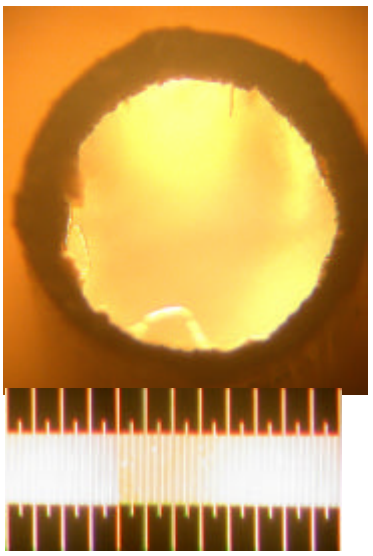

圖 17 **管徑為** 1 mm**，厚度為** 0.17 mm **之微管顯微照相圖**

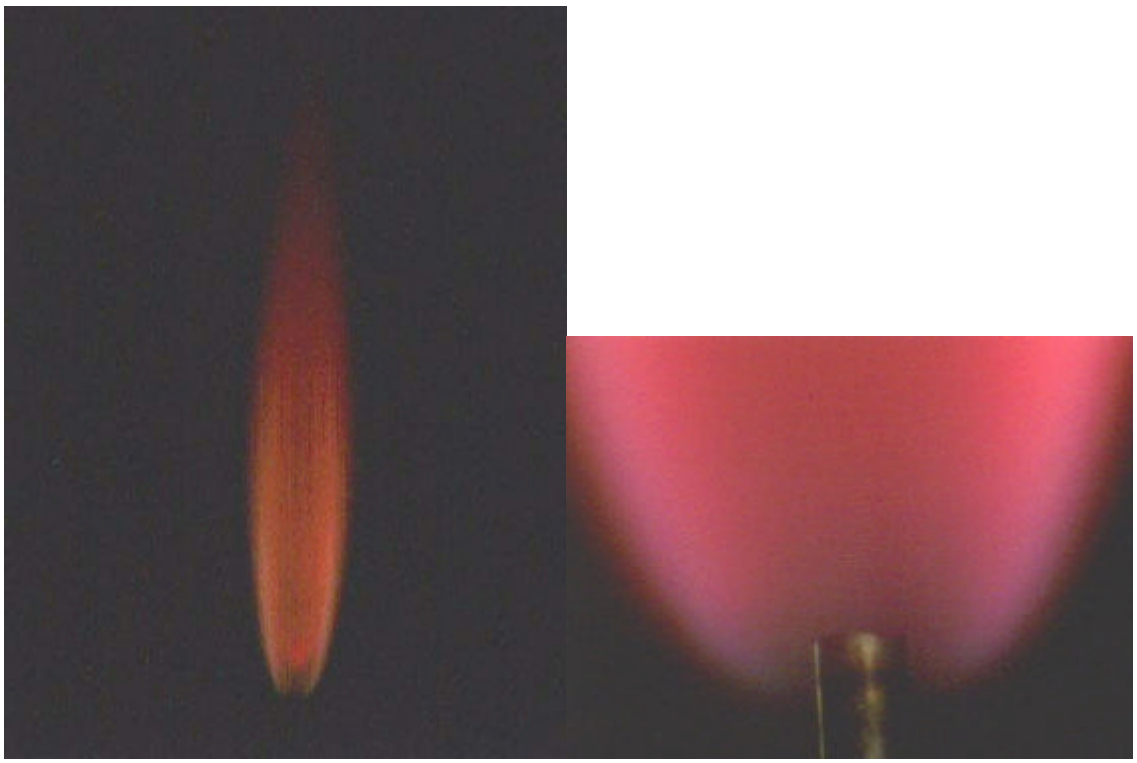

圖 18 **雷諾數** 330 **之微管氫氣噴流火焰照相圖**

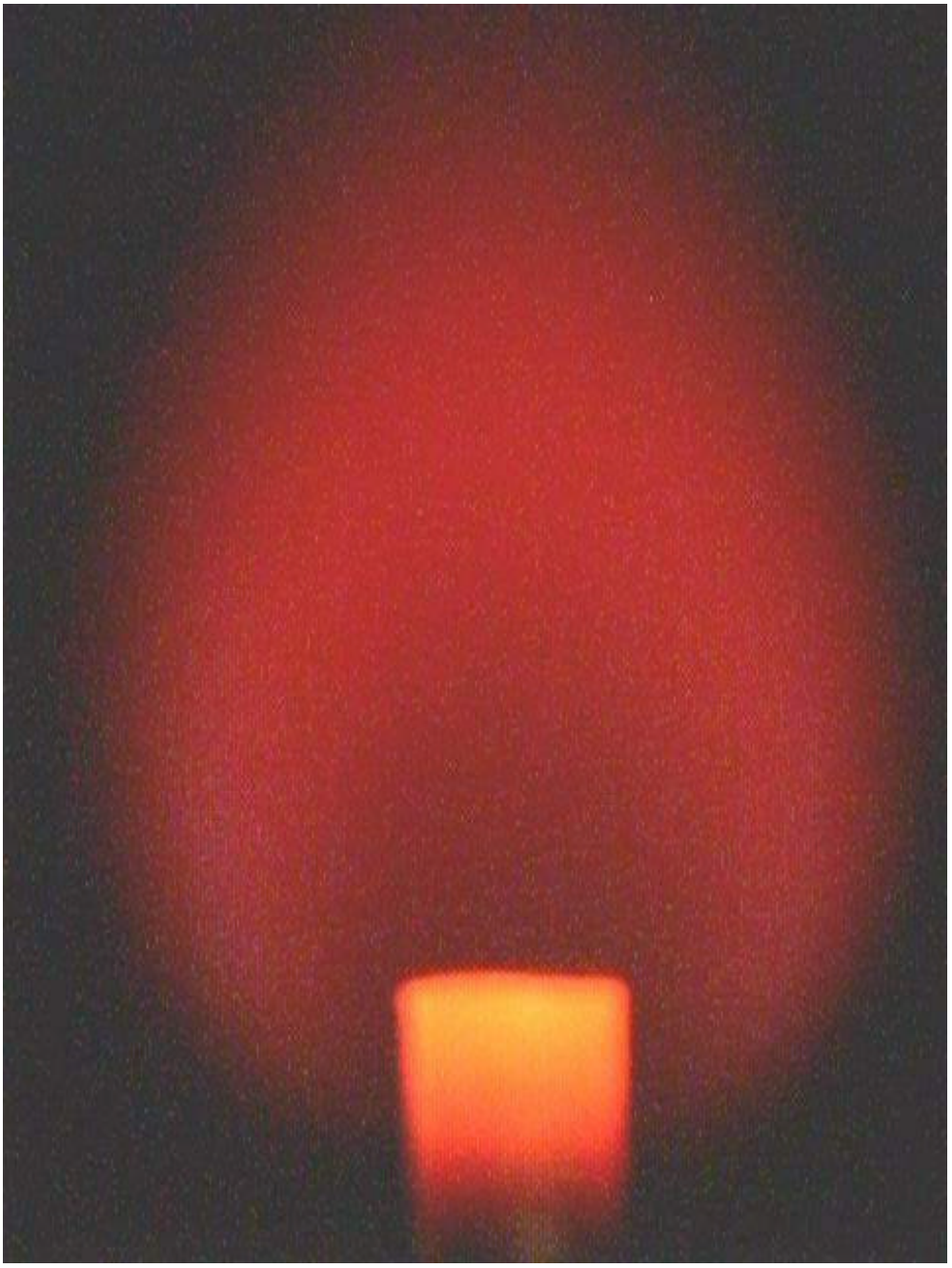

圖 19 雷諾數 30 之微管氫氣噴流火焰照相圖

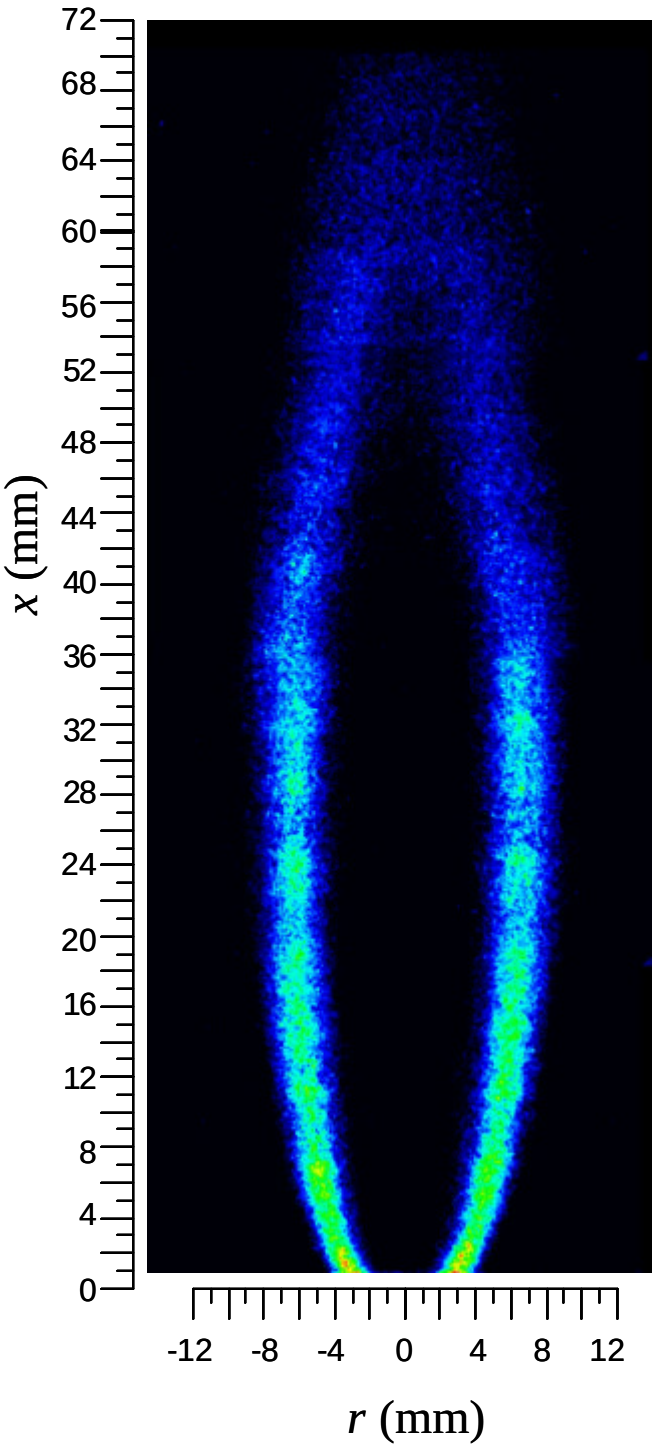

圖 20 **雷諾數** 330 **之二維** OH **螢光分布**

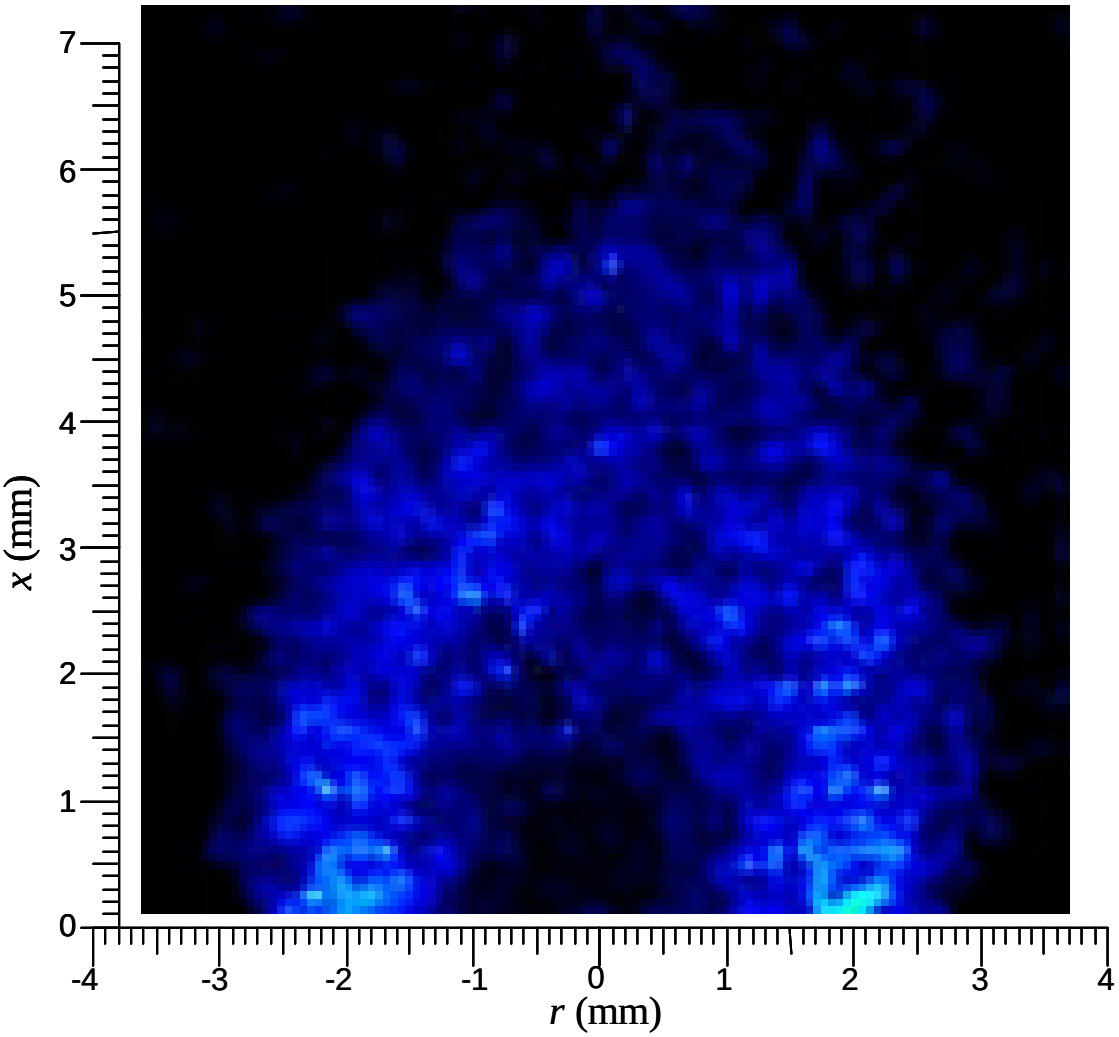

圖 21 **雷諾數** 30 **之二維** OH **螢光分布**

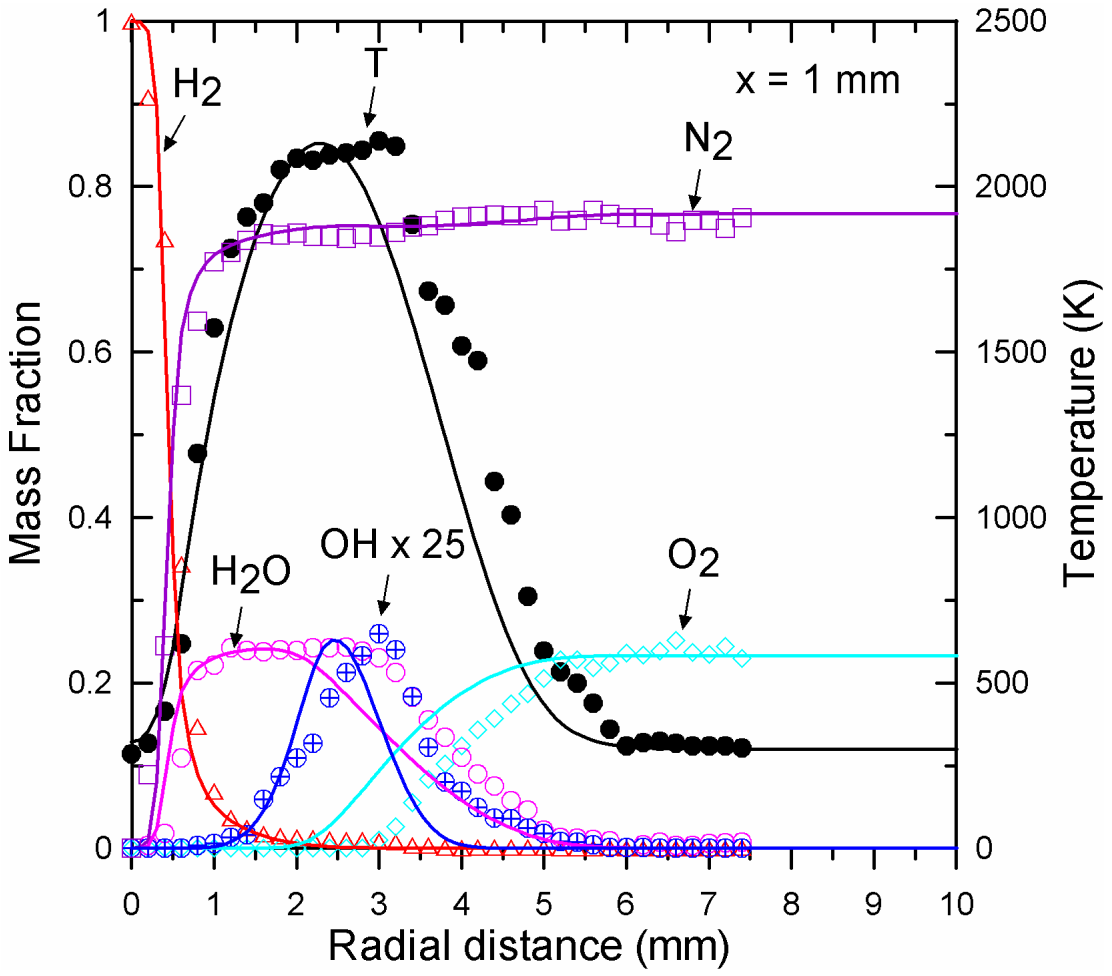

圖 22 雷諾數 330 火焰之平均溫度、主要組成份及 OH 質量分率在高度 x = 1 mm 處之實驗與計算徑向分布比較圖

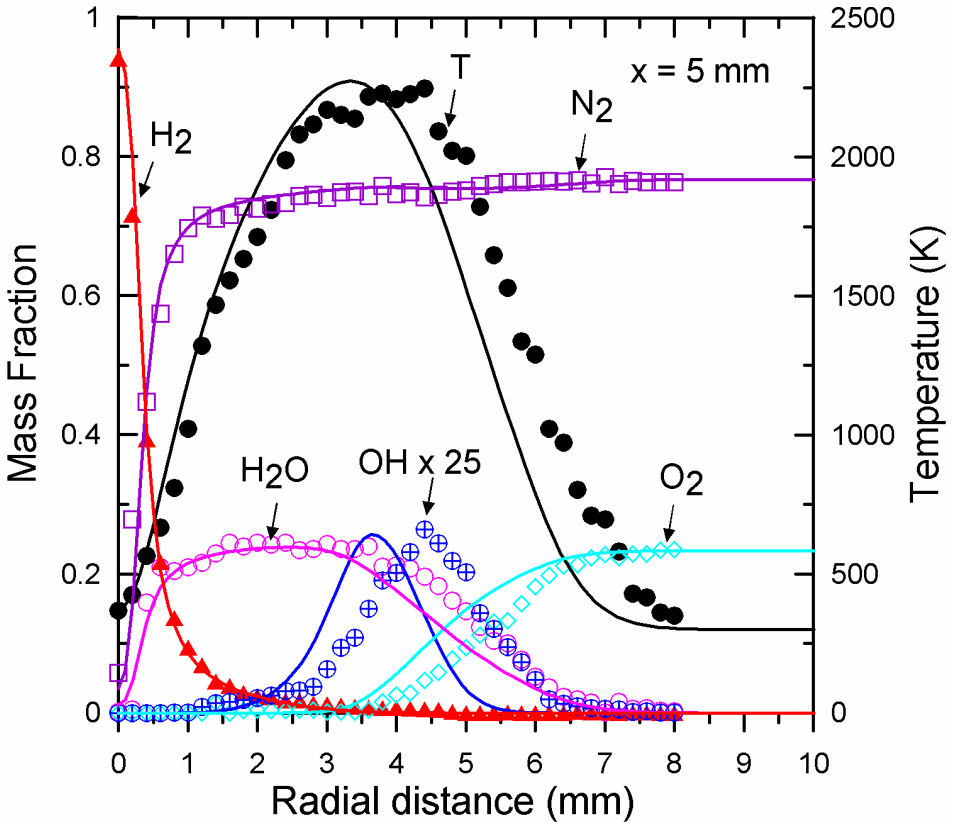

圖 23 雷諾數 330 火焰之平均溫度、主要組成份及 OH 質量分率在高度 x = 5 mm 處之實驗與計算徑向分布比較圖

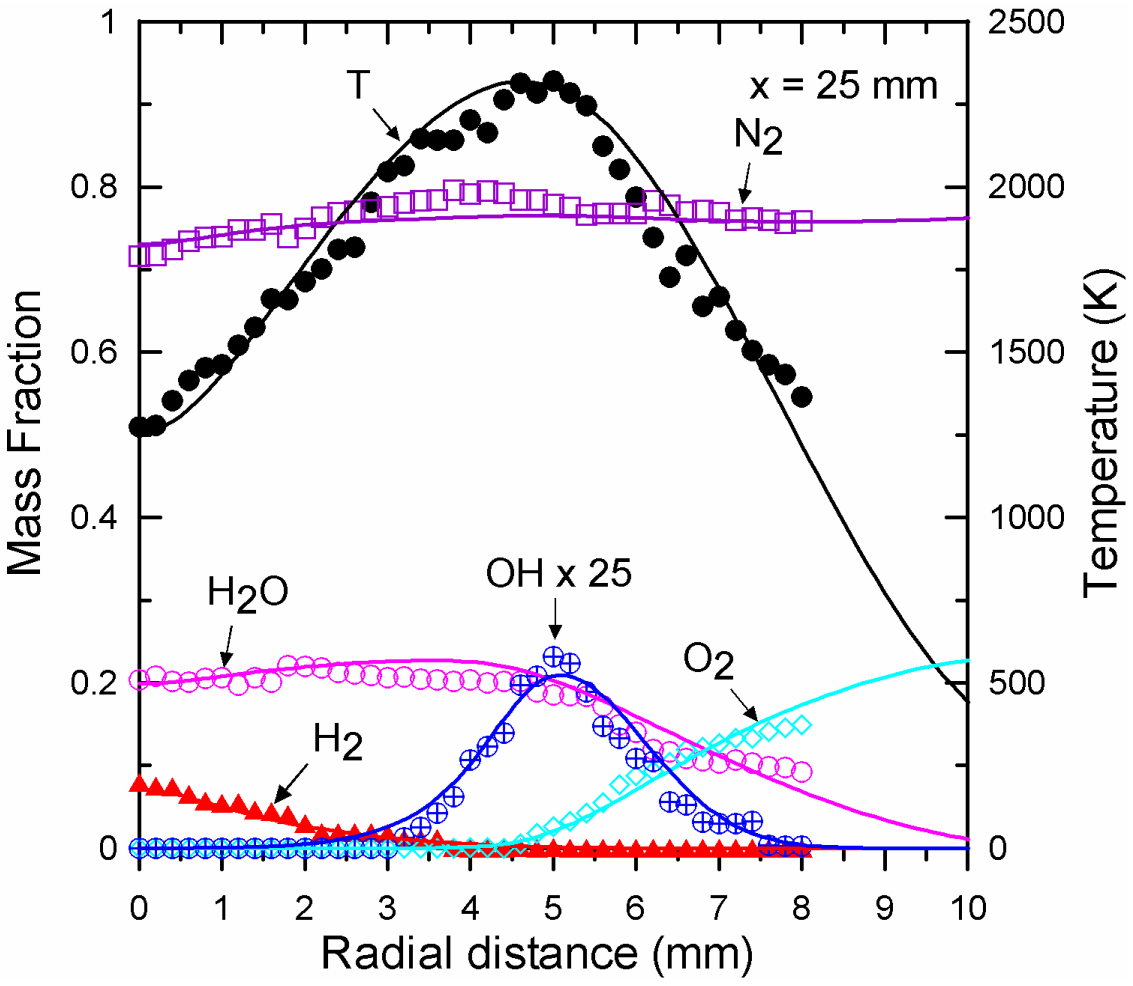

圖 24 雷諾數 330 火焰之平均溫度、主要組成份及 OH 質量分率在高度 x = 25 mm 處之實驗與計算徑向分布比較圖

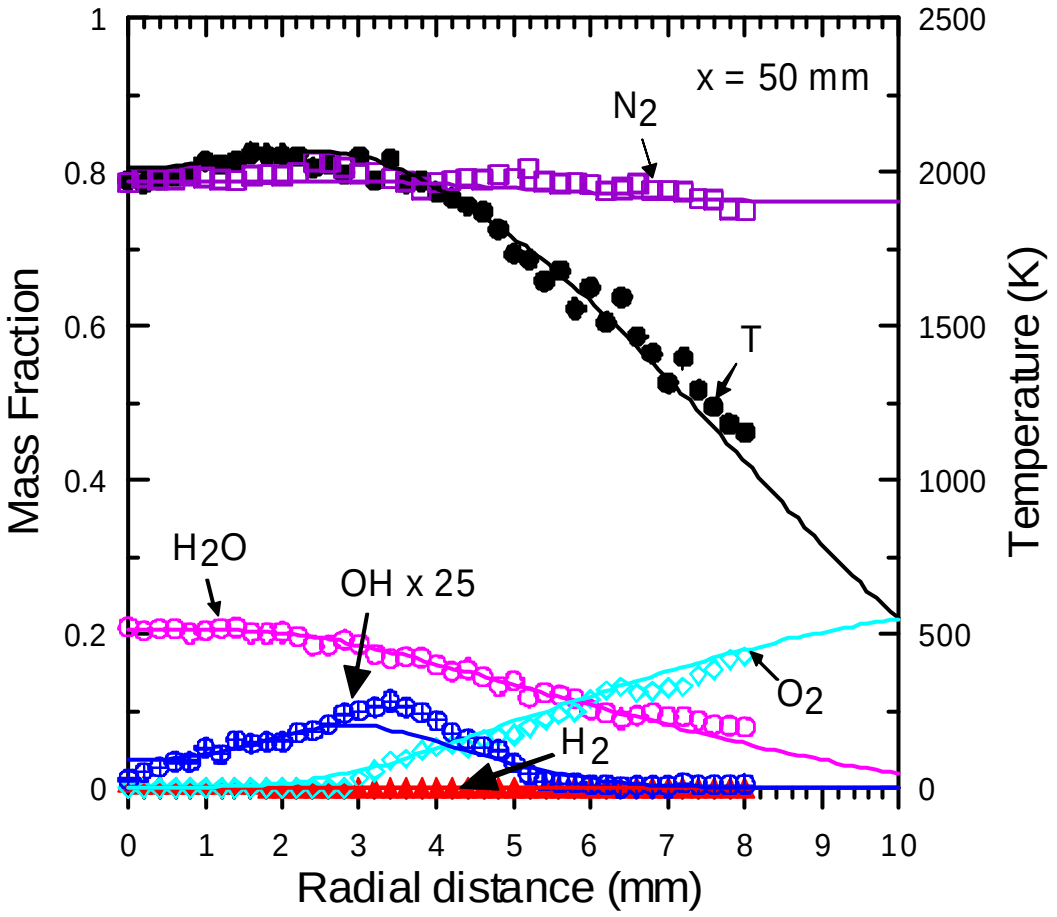

圖 25 雷諾數 330 火焰之平均溫度、主要組成份及 OH 質量分率在高度 x = 50 mm 處之實驗與計算徑向分布比較圖

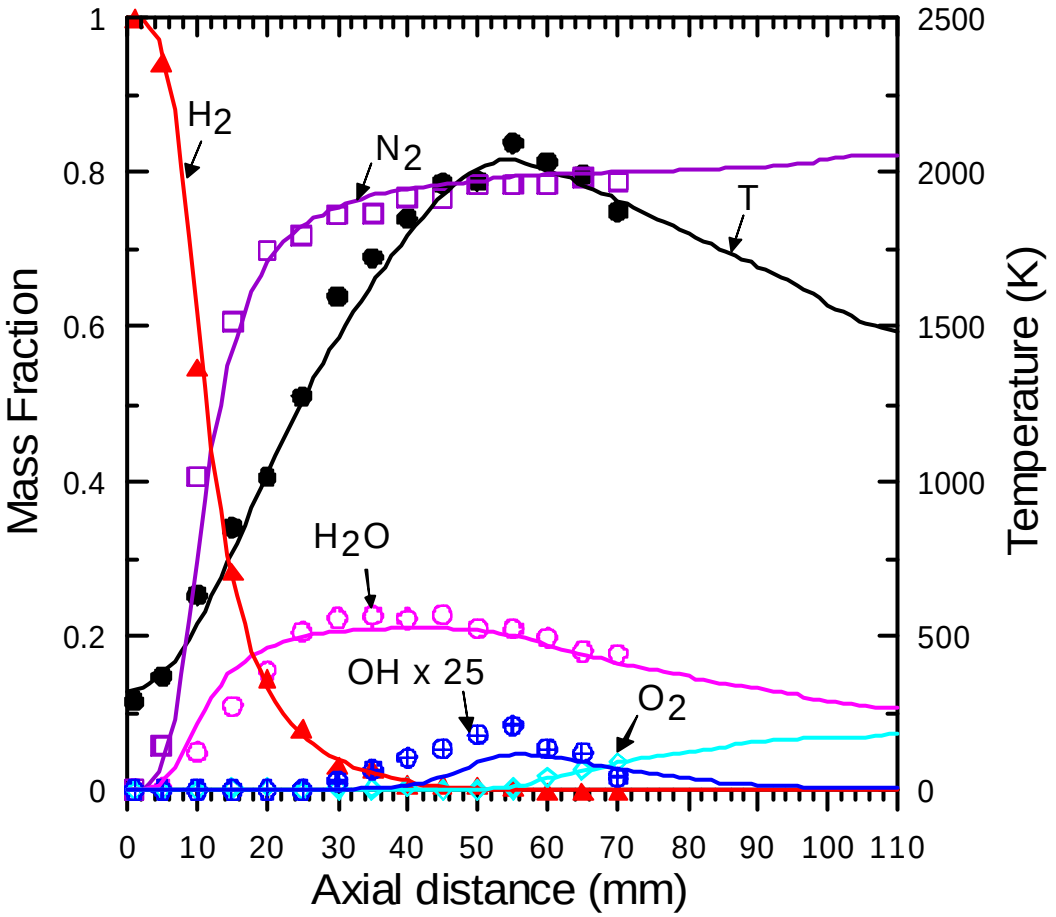

圖 26 雷諾數 330 火焰沿著噴流中心之平均溫度、主要組成份及 OH 質量分率之實驗與計算軸向分布比較圖

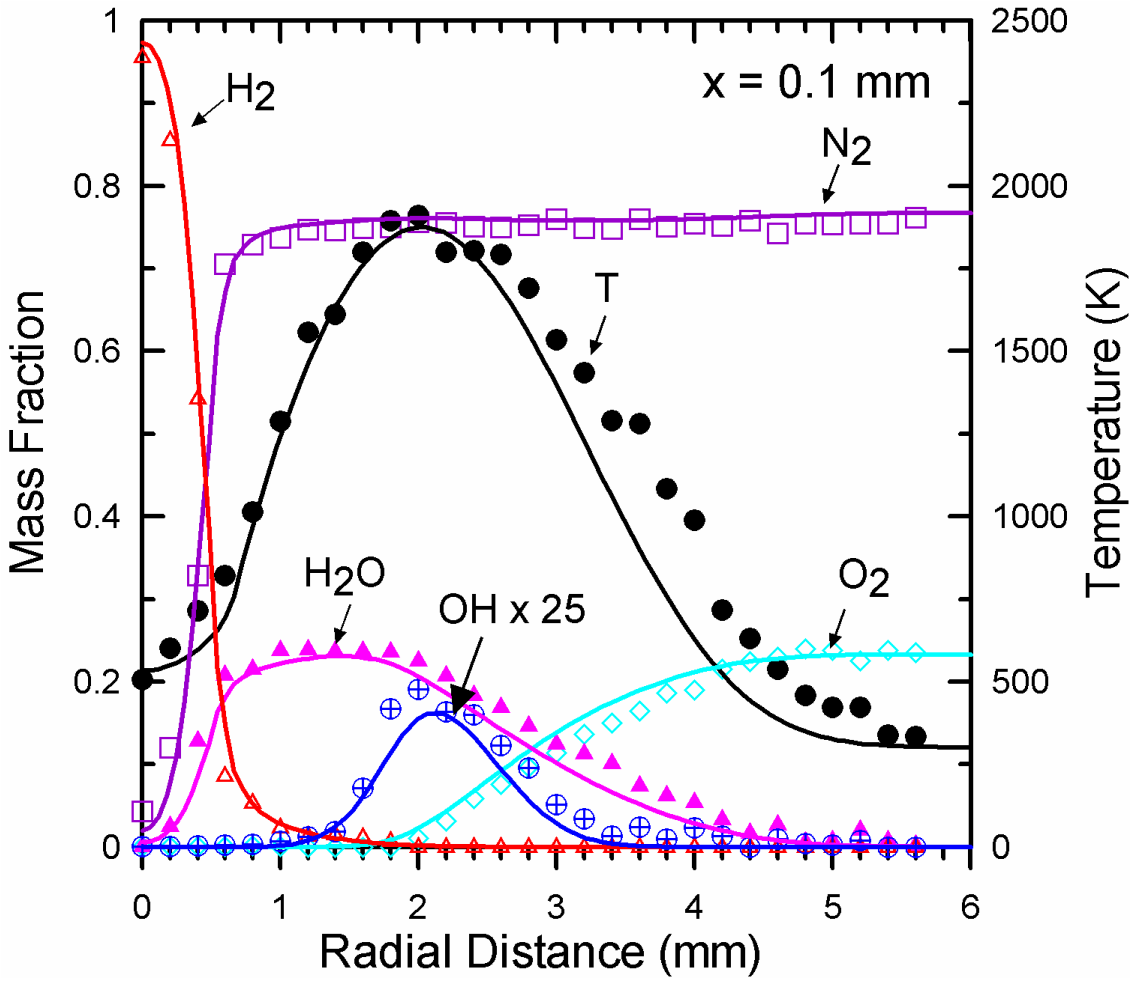

圖 27 雷諾數 30 火焰之平均溫度、主要組成份及 OH 質量分率在高度 x = 0.1 mm 處之實驗與計算徑向分布比較圖

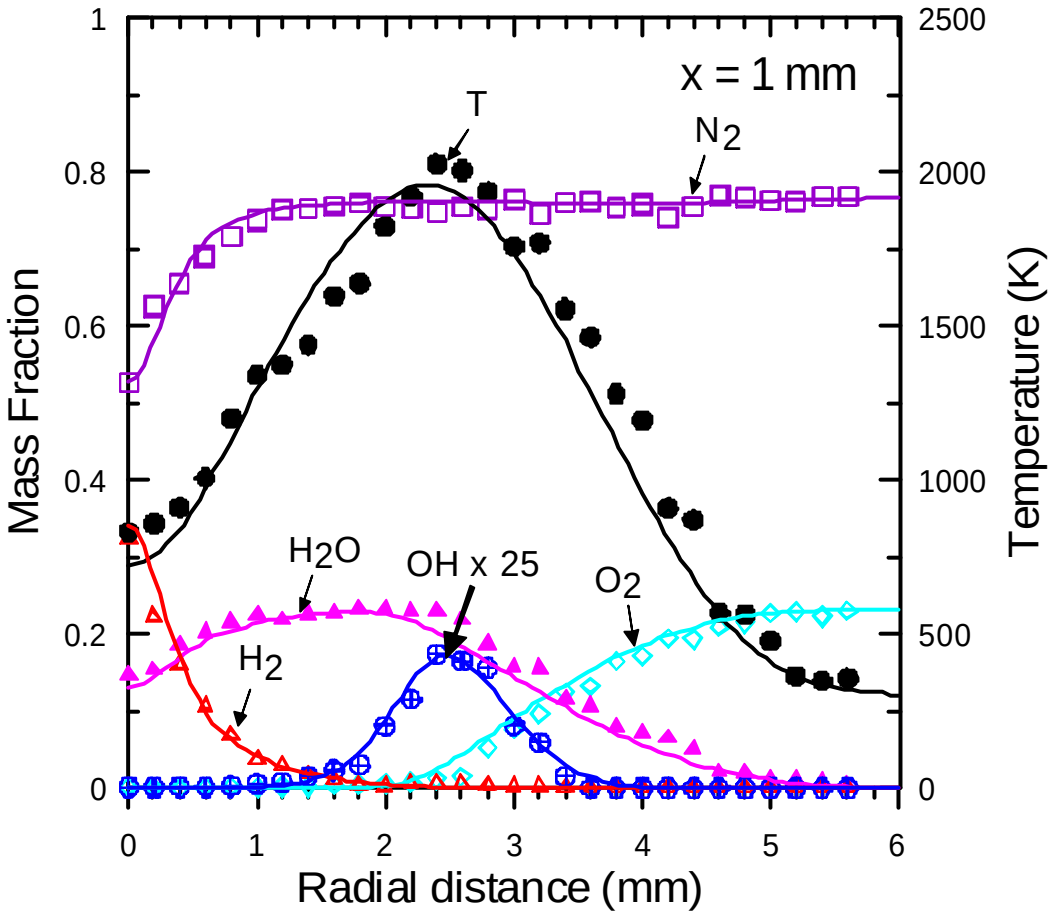

圖 28 雷諾數 30 火焰之平均溫度、主要組成份及 OH 質量分率在高度 x = 1 mm 處之實驗與計算徑向分布比較圖

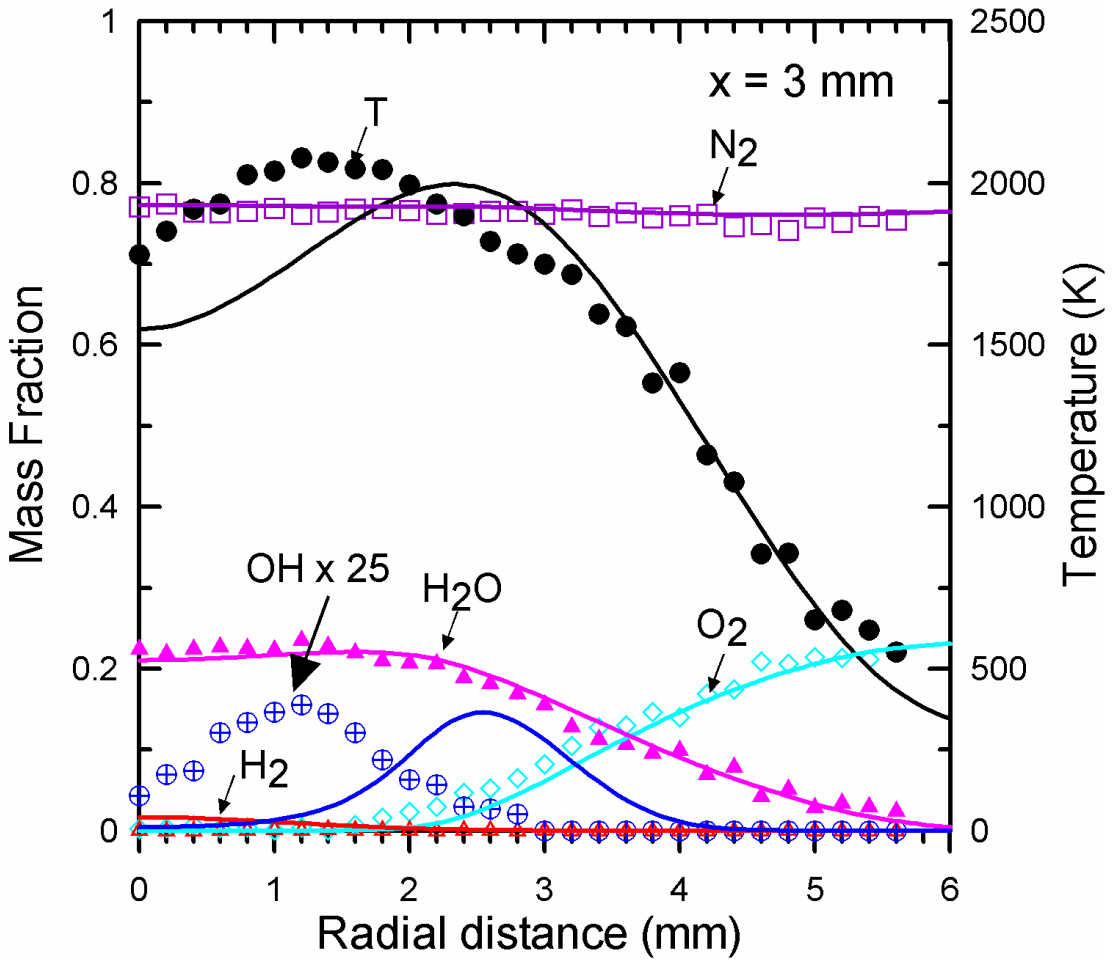

圖 29 雷諾數 30 火焰之平均溫度、主要組成份及 OH 質量分率在高度 x = 3 mm 處之實驗與計算徑向分布比較圖

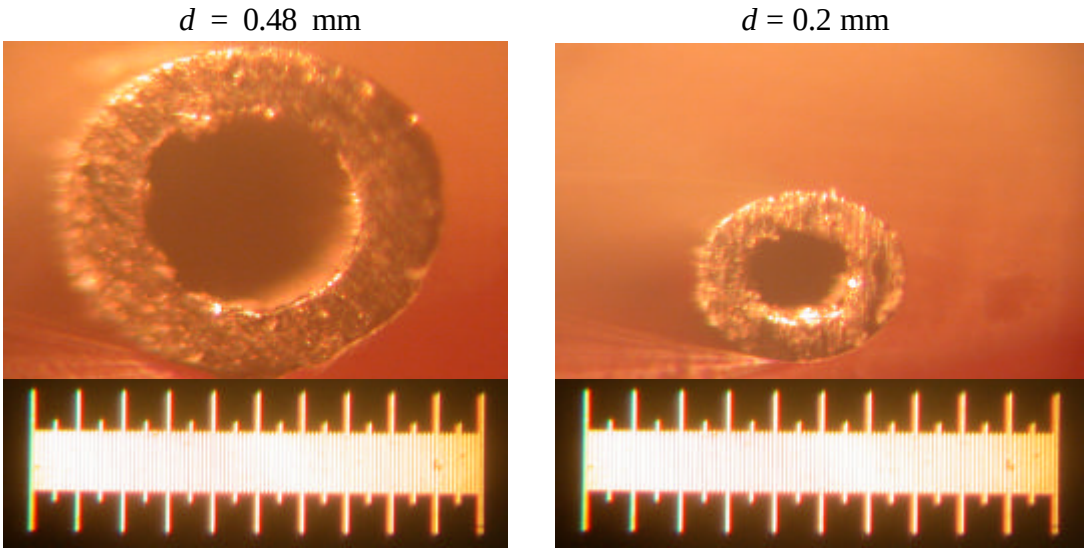

圖 30 **管徑為** 0.48 **及** 0.2 mm **其厚度分別為厚度為** 0.17 **及** 0.09 mm **之微管顯微照相圖**

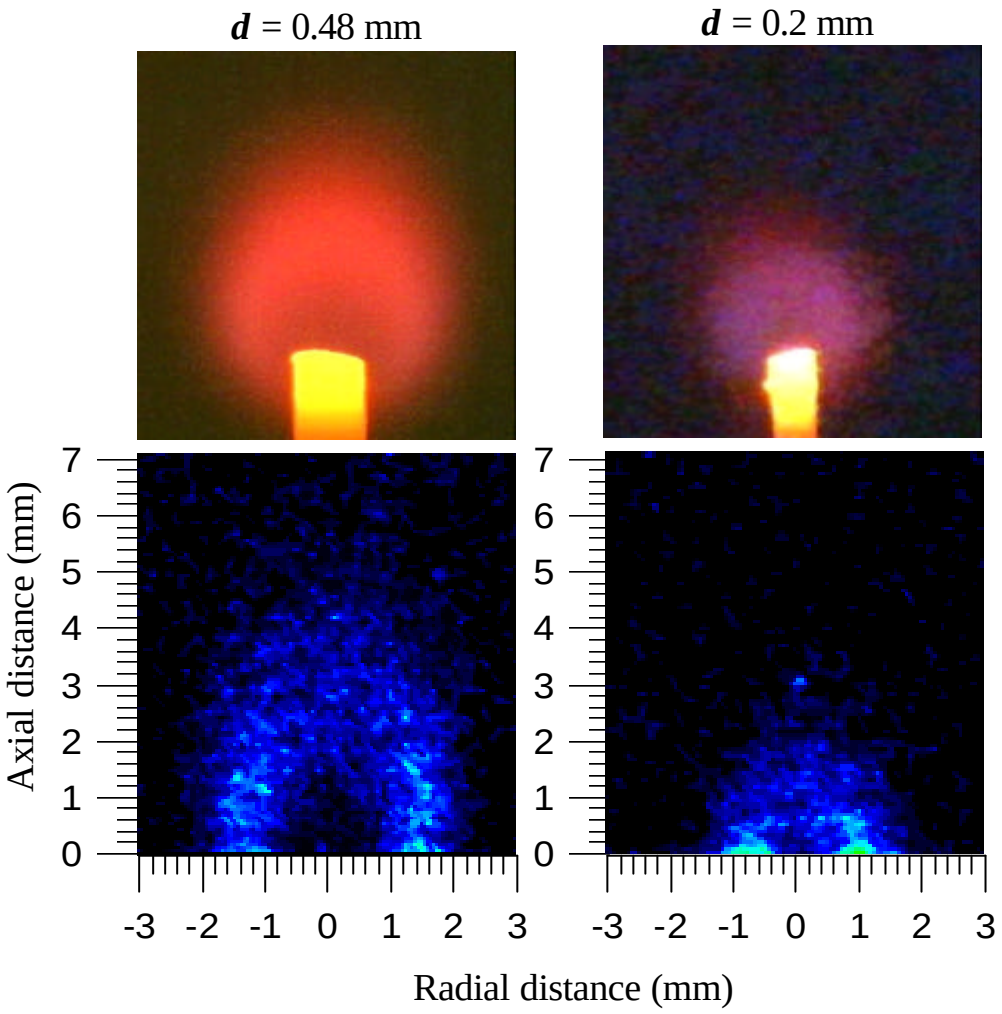

圖 31 **管徑** 0.2 **及** 0.48 mm **為氫氣擴散火焰之照相與單脈衝** OH **影像圖**

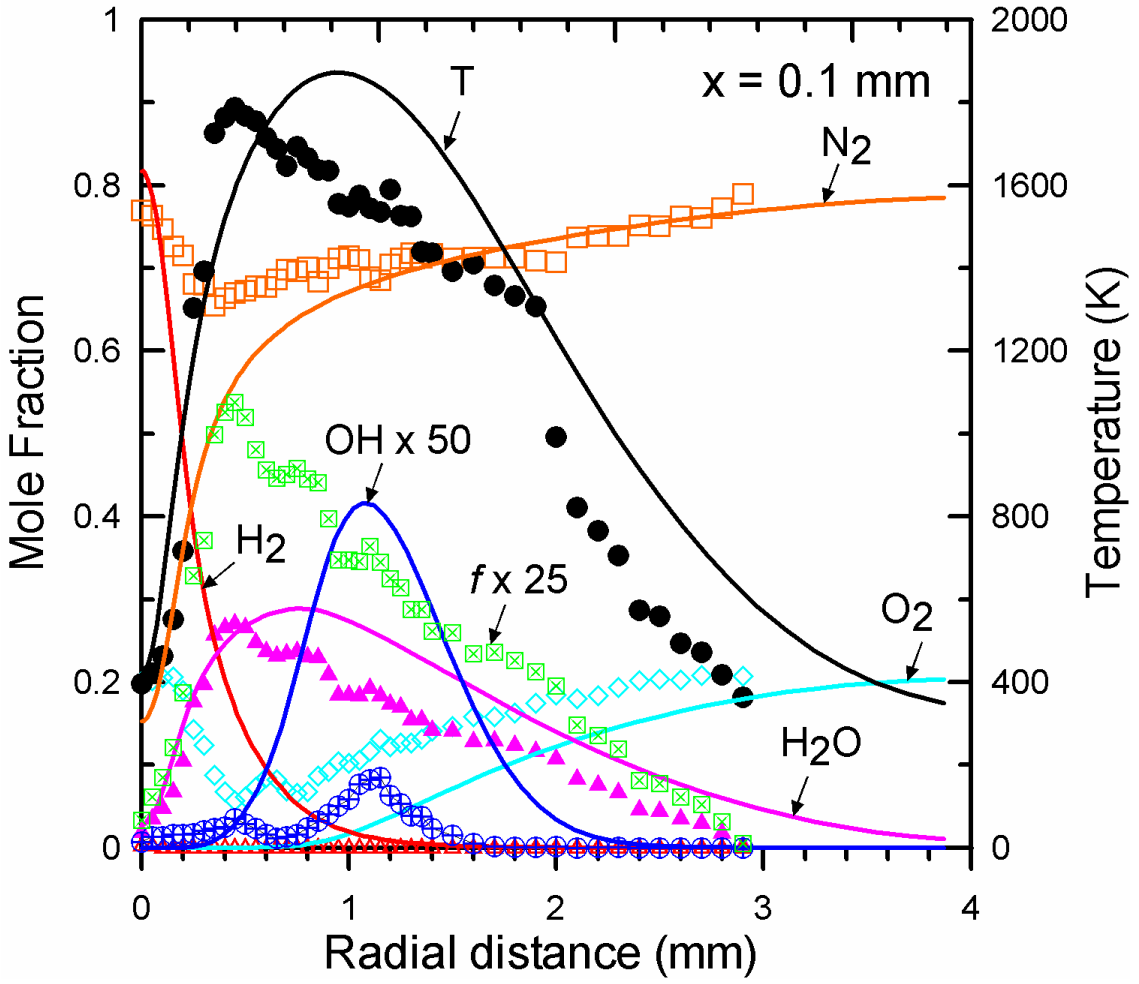

圖 32 **管徑** 0.2 mm **之火焰在高度** x = 0.1 mm **處實驗量測之平均溫度、主要組成份及** OH **莫爾分率徑向分布與計算結果比較圖。** ●: T, ◇: O2, □: N2, ▲: H2O, △: H2, ⊕: OH × 50, —: **計算結果**

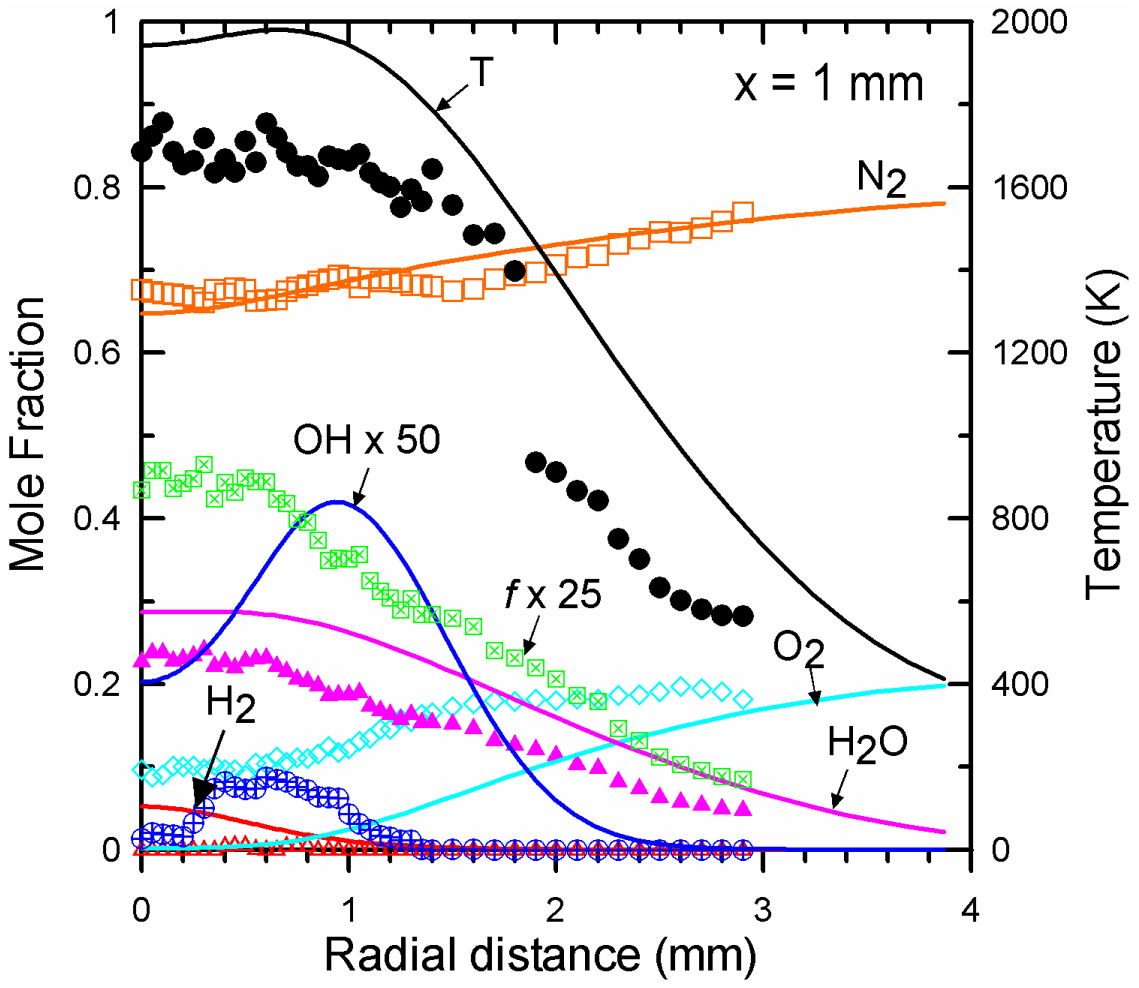

圖 33 管徑 0.2 mm 之火焰在高度 x = 1 mm 處實驗量測之平均溫度、主要組成份及 OH 莫爾分率徑向分布與計算結果比較圖。 ●: T, ◇: O2, □: N2, ▲: H2O, △: H2, ⊕: OH × 50, —: **計算結果**

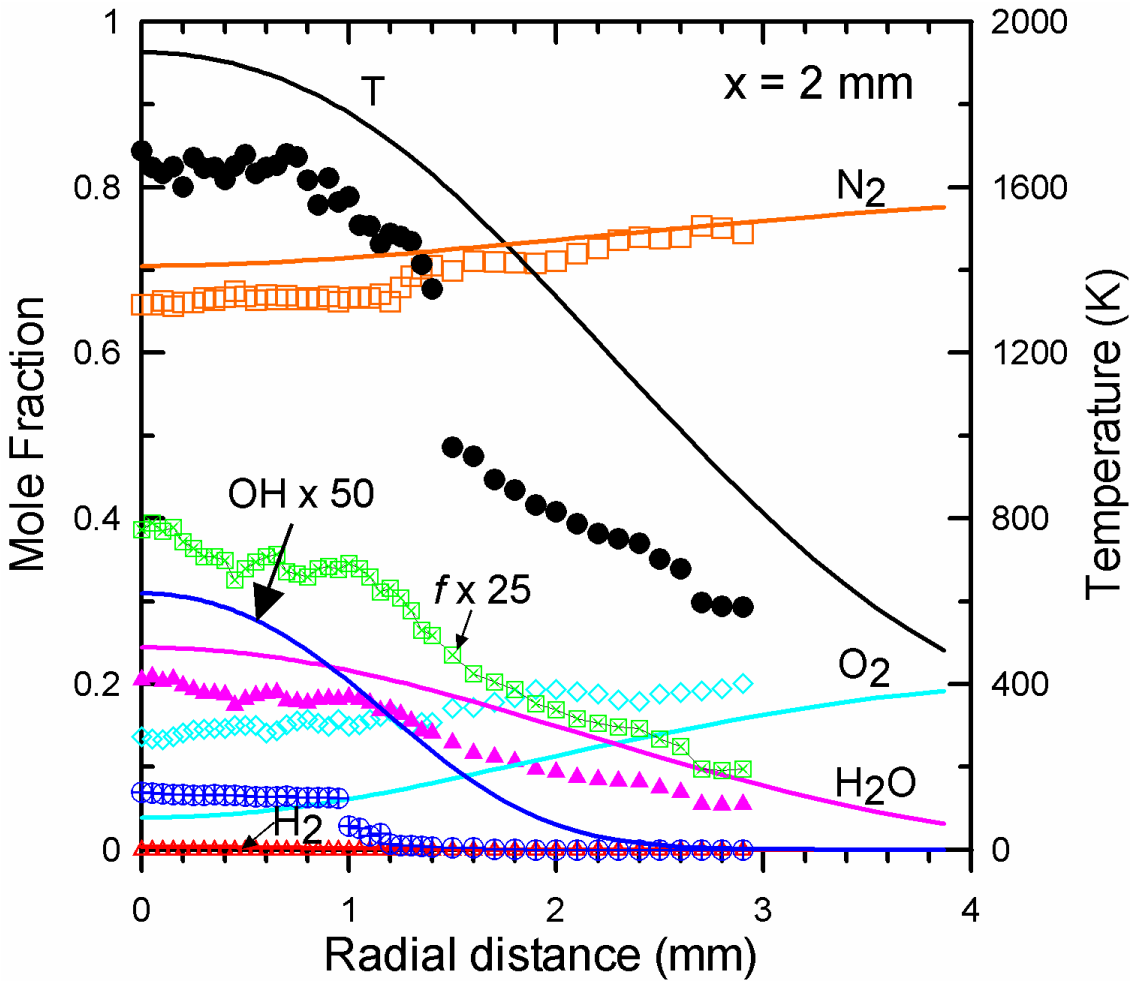

圖 34 管徑 0.2 mm 之火焰在高度 x = 2 mm 處實驗量測之平均溫度、主要組成份及 OH 莫爾分率徑向分布與計算結果比較圖。 ●: T, ◇: O2, □: N2, ▲: H2O, △: H2, ⊕: OH × 50, —: **計算結果**

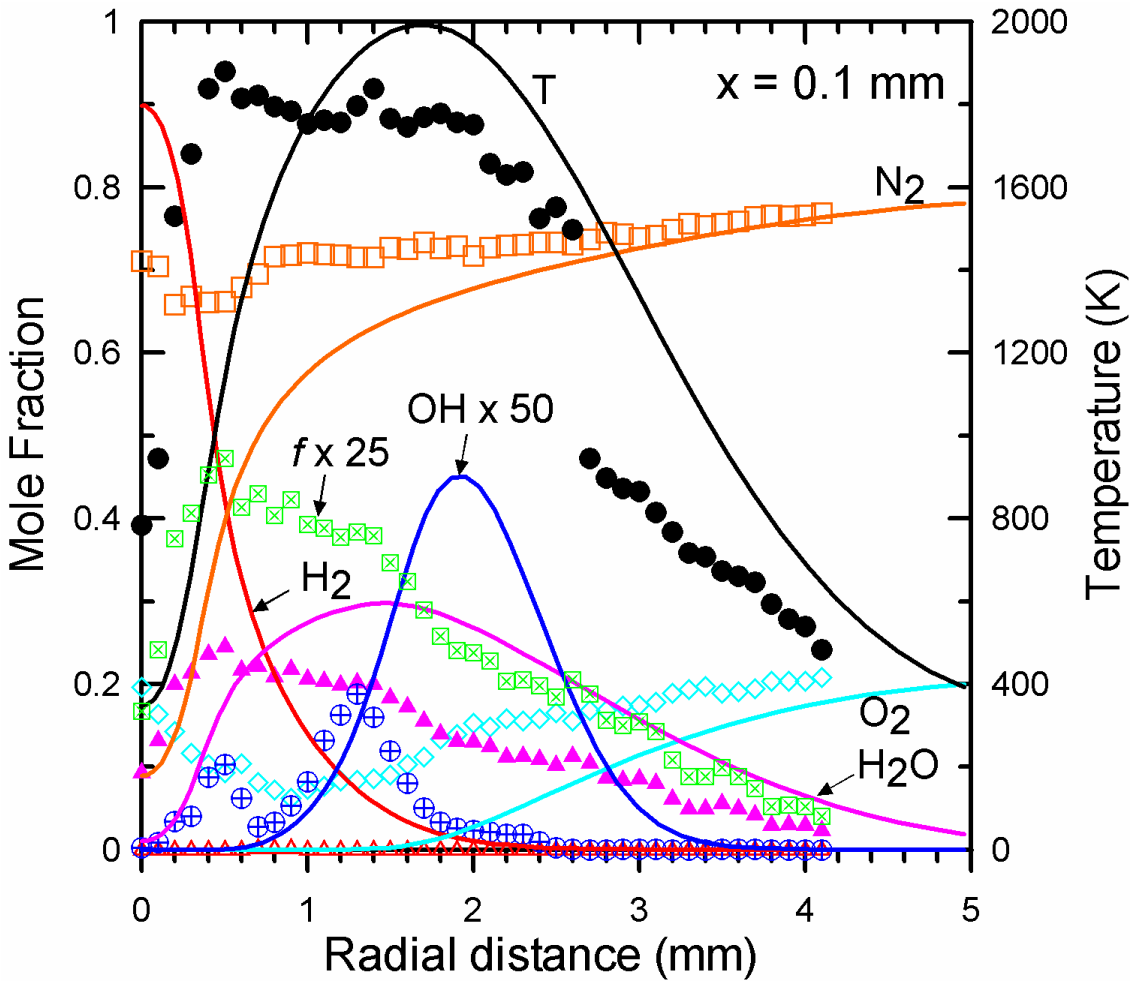

圖 35 管徑 0.48 mm 之火焰在高度 x = 0.1 mm 處實驗量測之平均溫度、主要組成份及 OH 莫爾分率徑向分布與計算結果比較圖。 ●: T, ◇: O2, □: N2, ▲: H2O, △: H2, ⊕: OH × 50, —: **計算結果**

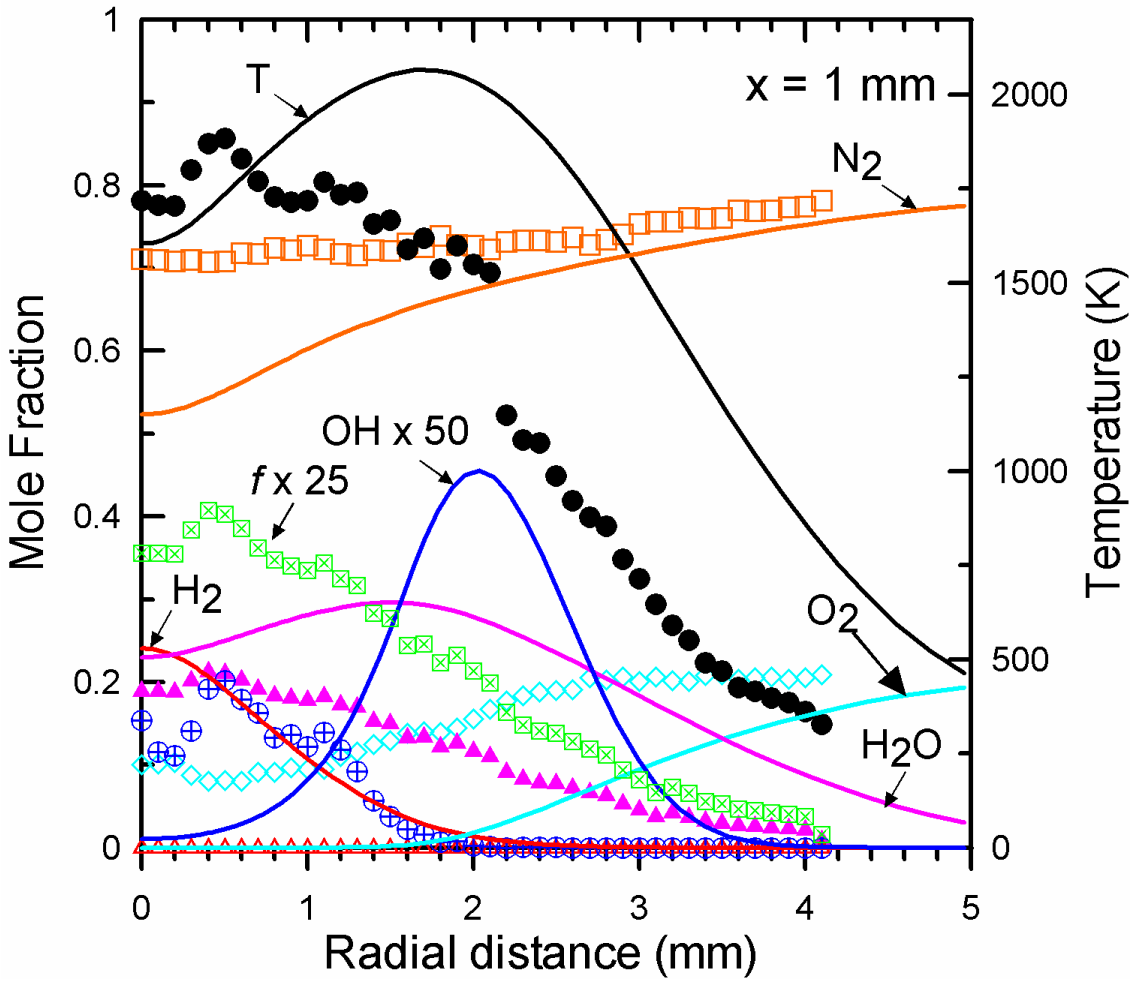

圖 36 **管徑** 0.48 mm **之火焰在高度** x = 1 mm **處實驗量測之平均溫度、主要組成份及** OH **莫爾分率徑向分布與計算結果比較圖。** ●: T, ◇: O2, □: N2, ▲: H2O, △: H2, ⊕: OH × 50, —: **計算結果**

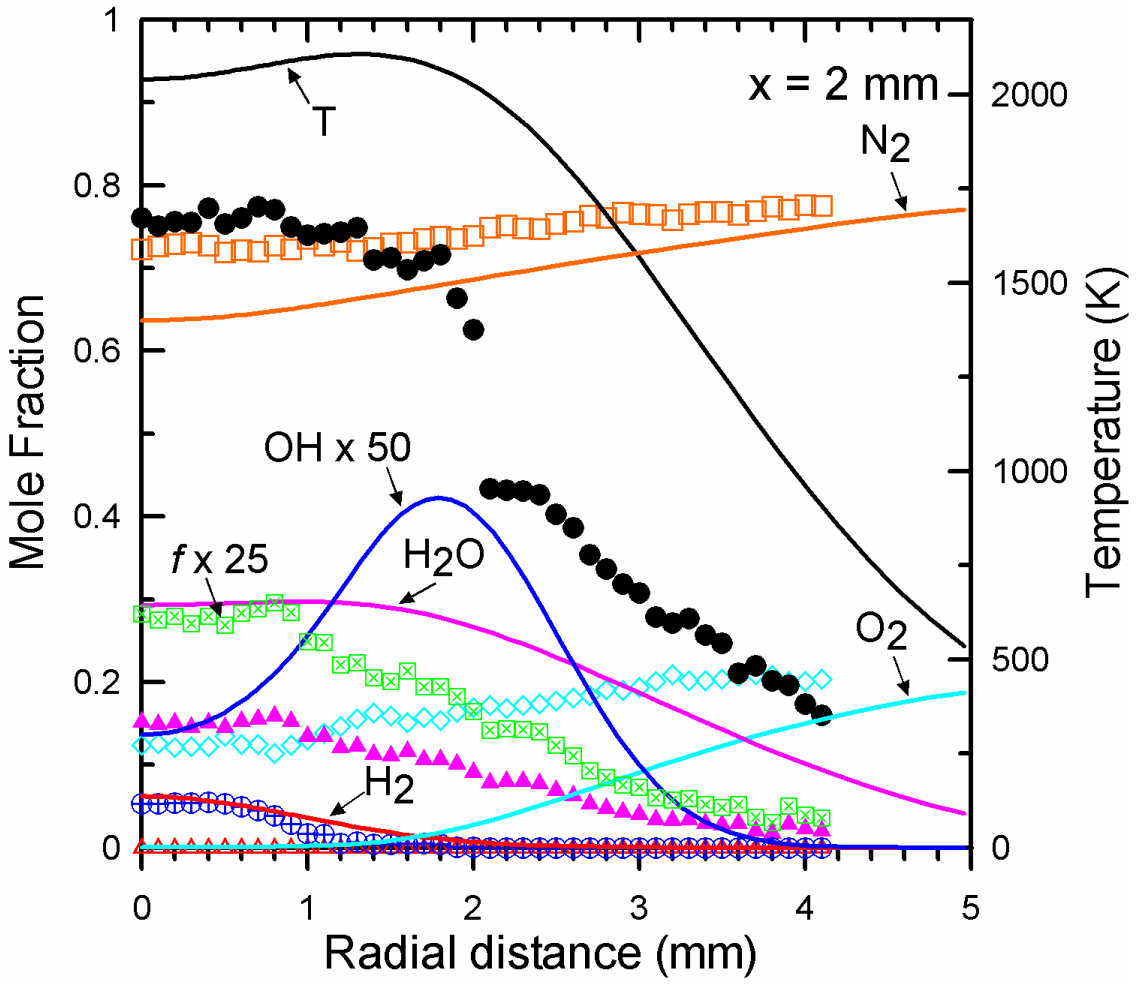

圖 37 **管徑** 0.48 mm **之火焰在高度** x = 2 mm **處實驗量測之平均溫度、主要組成份及** OH **莫爾分率徑向分布與計算結果比較圖。** ●: T, ◇: O2, □: N2, ▲: H2O, △: H2, ⊕: OH × 50, —: **計算結果**

計畫成果自評

本子計畫之主要研究內容乃是改良現有之紫外光拉曼散射及雷射誘發預解離螢光系統，使其具有更佳之空間解析度，以量測觸媒微管反應後之產物及微管噴流火焰，進而瞭解觸媒微管及微型火焰之特性，作為研發微推進系統之參考。整體而言，本研究內容符合原計畫項目，並達成預期目標。所開發之雷射診測系統可應用於必須具有極佳解析度之微反應器燃燒產物量測，惟因雷射光經聚焦之後單位體積能量密度甚高，即使降低雷射能量至不致造成空氣解離，但一般石英視窗仍然無法承受如此高能量密度之雷射光，因此本雷射診測系統僅能應用於具外流場之微尺度量測。在配合總計畫進行研發微推進系統的過程中，本子計畫之研究成果亦每年在國內外之學術研討會發表(詳見參考文獻[40-45]及附錄) ，其中在 2004 年美國芝加哥舉行之第 30 屆國際燃燒會議所發表的「微氫氣擴散火焰之實驗與數值研究」論文不但是國際上首次針對微火焰進行最完整之定量量測，同時該論文亦即將刊登在國際燃燒學會之 SCI 期刊。此外，我們也正在整理過去兩年在國內外研討會發表之實驗數據，在完成數值模擬與實驗數據比對之後，將投稿國際著名有關燃燒之 SCI 期刊發表。同時，由本研究發現，當火焰小至直徑約 2 mm 之球型火焰時，火焰屬於對流－擴散主控區域，因此對較輕分子熱擴散效應的考慮及化學反應模式的選用就變得相當重要，這對將來利用數值模擬作為研發微推進系統之輔助工具時將扮演重要參考依據。

誌謝

感謝國科會對本計畫全程三年(90/8~93/7)之經費補助，計畫編號 NSC90-2212-E-216-019, NSC91-2212-E-216-010, NSC92-2212-E-216-001，同時我們亦感謝成大航太所趙怡欽、袁曉峰及呂宗行教授在實驗儀器設備上及研究生人力（吳志勇、李約亨、陳志鵬、李國源、張智銘、張智國）所提供的協助以及日本名古屋大學中村佑二(Yuji Nakamura)教授在數值模擬的合作，使得本計畫得以順利完成。

附　　錄

中華民國燃燒學會第 13 屆學術研討會，台北市，March 29, 2004

應用雷射診測技術於微反應系統之初步研究

鄭藏勝
中華大學機械工程學系暨機航所

趙怡欽、吳志勇、陳冠邦、袁曉峰、呂宗行
國立成功大學航空太空工程學系
國立成功大學太空科學與技術研究中心

摘要

國際間正積極發展以微機電系統技術製作之化學微推進系統，為了研究微反應系統內流場速度、壓力及化學反應對微燃燒室性能之影響，微燃燒室內或其出口之速度、壓力、溫度及反應物濃度的量測是相當重要的。本文旨在探討應用雷射診測技術研究微燃燒室流場之可行性，初期係以 1 mm 之微管並利用改良之光學系統針對微管出口之未反應氣體（CO_2 及 CH_4）進行組成份濃度分布量測，以瞭解雷射系統是否足以解析微管流場。量測結果顯示，取樣體積為 $0.02 \times 0.04 \times 0.04$ mm^3 之解析度足以用來量測微管出口非反應 CH_4 之濃度分布，由濃度分布可利用自似性推算出速度分布，未來本雷射系統將可應用於微反應槽出口的量測。

關鍵字：微機電系統、雷射診測技術、微燃燒

一、前言

近幾年來國內在微機電系統 (Micro-Electro-Mechanical Systems: MEMS)的研究正蓬勃發展，研究的方向主要還是在 IC 的設計與製造以及其相關之冷卻問題，至於在航太領域中以 MEMS 為基礎之化學微推進系統則尚未有研究報告出現。由於發展人造衛星的應用與研究乃國家的既定政策，而微衛星(Micro-Satellite)因其體積與重量皆比一般衛星要少很多，不論其軌道運行空間或是其發射成本考量皆優於目前使用的一般衛星，因此在發展衛星科技的同時，微衛星相關的科技研究是值得重視的課題。目前美國 NASA[1]正極力推展 1-10 公斤等級微衛星的研發，其將微衛星分成三個等級，第一種等級介於 5-10 公斤，直徑約 30 公分，其姿態控制 (Attitude Control)所需之推力可利用 4.5 mN 之冷氣體推進器(Cold Gas Thruster)，或是利用直徑 5-10 公分之離子引擎(Ion Engine)。第二種等級約 1 公斤，直徑約 10 公分，其姿態控制所需之推進器就必須結合 MEMS 技術重新設計，因為低於微米大小的噴嘴喉部必須依靠 MEMS 技術才能製造。第三種等級低於 1 公斤，直徑約 1-3 公分，體積如此小之微衛星其推進器將比第二種等級還要小，那麼如何將系統整合便成為關鍵技術，也就是說把所有的零組件整合在一片晶片上 (System-on-a-Chip)。第三種等級目前僅止於概念階段，尚未真正投入研發，目前美國 NASA 真正投入研發的微推進系統也僅止於第一及第二種等級的應用。

對微推進系統而言，其需求不外乎已超越目前傳統尺寸的推進技術就是必須從目前已具有的技術去作更先進的改良，目前有幾個概念已被提出並進行可行性研究，如美國噴射推進實驗室提出以 MEMS 為基礎之相變化推進器(Phase Change Thruster)，如昇華固體微推進器 (Subliming Solid Micro-Thruster)和汽化液體微推進器(Vaporizing Liquid Micro-Thruster)，固體推

進劑為氨鹽(Ammonia Salts)，液體推進劑為水、氨(Ammonia)或聯氨(Hydrazine)。其他還有可提供高比衝之晶片型離子推進器，或是目前正在構思的射頻(Radio-Frequency)和冷陰極(Cold cathode)推進器。此外，NASA Lewis 研究中心[2]亦提出研發高性能、無毒性之單推進劑(Monopropellant)系統以取代目前所使用的聯氨(N_2H_4)單推進劑，惟耐高溫觸媒的開發是此高性能、無毒性之單推進劑系統是否能成功的關鍵。其他一些化學推進系統亦被考慮，如(1)利用氫、氧和惰性氣體(氮或氦)混合物之溫氣體推進系統以取代冷氣體推進系統，(2)熱解固體和混合物燃料之推進系統，(3)電解水以提供推進及電力雙重功能之推進系統，(4)以微渦輪機械(Microturbomachinery)為基礎之推進系統。

在研發微推進器的同時下列幾點因素必須加以考慮:(1)質量與體積，（2）氣體洩漏(Gas Leakage)，(3)過濾和污染(Filtration and Contamination)，(4)高動量(高速度差)，(5)流場物理特性，但其影響如何仍有待更深入的研究。由於以 MEMS 技術為基礎之微推進器不但可整合感測器、致動器、以及控制電路於單一晶片上，推進器的組成也單純化，所需能源也相對降低很多，這些都是國內發展微推進系統的優點及前景，可見其具有發展的重要性與前瞻性。對於微推進系統內部有關微槽(Micro Channel)之流力、熱傳、及流體傳輸現象的研究亦已成為一新的領域，而微米槽內之流體現象通常以 Knudsen 數($Kn = l/L$，l為粒子的平均自由路徑，L為特徵長度)和平均分子間的距離(δ)與分子直徑(d)的比值來判別，若 Knudsen 數大於或等於 1，則傳統連續流體之假設即不適用，Navier-Stokes 方程式僅能用在$d / d > 10$和$Kn < 0.1$的區域，由於微槽內之流體通常屬於高 Knudsen 數範圍，傳統的流場統御方程式可能無法完全描述流場物理現象，因此，在發展 MEMS 技術的同時其微槽內和出口處之流場物理現象必須加以研究。

研究方法不外乎理論探討、數值模擬、或實驗量測。理論探討是以統計方法直接或近似解 Boltzmann 方程式[3]，數值模擬則以直接模擬蒙地卡羅(Direct Simulation Monte Carlo, DSMC)方法解非線性 Boltzmann 方程式[4]，DSMC 方法已被應用低壓 CVD(Chemical Vapor Deposition)系統半導體長晶過程的研究[5]，電漿蝕刻 SiO_2 流場模擬[6]，及微槽內溫度分布的計算[7]。而實驗量測方面則是利用預埋入微槽內之壓力或溫度感測器(Sensor)量測壓力[8]或溫度[9]分布，至於使用光學診測方法量測微米槽內或其出口處之溫度或組成份濃度分布則尚無研究報告出現。因此本文旨在探討應用光學診測技術來研究微槽流場之可行性。

二、實驗設備及儀器

本研究主要在改良原有的雷射診測系統，期能解析微尺度之流場，雷射診測系統如圖 1 所示。雷射係使用可調波長之準分子雷射(Lambda Physik LPX-250T)，正常輸出波長為 248 nm，可調範圍為 1 nm (248-249 nm)，脈寬約為 20 ns，最大重複率(Repetition rate)為 50 Hz，若使用氦氣為緩衝氣體(Buffer gas)，則每脈衝之最大能量約為 250 mJ，但若使用氖氣為緩衝氣體則每脈衝之最大能量可達 450 mJ，雷射光之發散率約為 0.2×10^{-3} rad。雷射光經由聚焦鏡片聚焦於微管上方之後，其拉曼散射(Raman Scattering)光或螢光可經由光學鏡片將其收集之後導入光譜儀作光色散處理，而收集散射光之鏡片通常以球面鏡片為之，而大直徑之鏡片其厚度也較厚，因此容易造成象差(Aberration)，而致使較難將散射光或螢光完全聚焦使其進入光譜儀，因此，本研究係使用卡塞格侖反射鏡(Cassegrain mirror)收集散射光並聚焦使其進入 SpectraPro-275 之光譜儀，經由光譜儀分光之後的拉曼散射光係由 ICCD 照

相機所量測，並將其訊號儲存於個人電腦以作進一步的分析。而吾人亦利用一光電增倍管(Photomultiplier tube)量測由聚焦鏡片所反射之雷射光，以作為雷射脈衝能量之相對量測。

由於所使用之準分子雷射其雷射光發散率約為 0.2×10^{-3} rad，若以焦距 2000 mm 之聚焦鏡片聚焦，則其理論焦點之最小尺寸約為 0.4 mm，那麼如果使用此解析度來量測 1 mm 甚至微米尺寸之微管，則解析度不夠。因此，本實驗採用 200 mm 之聚焦鏡聚焦，其焦點之最小理論尺寸約為 0.04 mm，但單發雷射打在感應紙之後，經顯微鏡量測其焦點截面積約為 0.02×0.04 mm^2 (如圖 2 所示)，其中 0.04 mm 為平行於噴流方向之焦點高度，但使用如此短焦距之聚焦鏡片必須降低雷射之輸出脈衝能量，否則因單位體積的雷射能量太高將造成氣體離子化(Ionization)現象，同時由於所量測之體積亦比使用焦距為 2000 mm 之聚焦鏡片縮小 10 倍，因此散射光之強度也將大大的降低，這對使用拉曼散射技術量測微米流場之組成份濃度將有極不利之影響。在未針對微米槽(Micro Channel)進行量測之前，吾人先對 D = 1 mm 微管(如圖 3 所示)出口未反應氣體進行拉曼散射光譜量測，1 mm 微管係固定在微調精度為 1 μm 之雙軸移動平台之上。準分子雷射波長調至 248.56 nm 以避免直接激發 OH 及 O_2 而造成其螢光干擾拉曼訊號，雷射輸出能量為 160 mJ/pulse，SpectraPro-275 光譜儀波長設定在 270 nm，入口隙縫設為 100 μm 以收集足夠的散射光作光譜分析又不致造成譜線太過寬廣而造成不同訊號之譜線相互干擾，由於光譜儀之入口隙縫係與雷射光垂直，依光譜儀入口隙縫寬度(100 μm)及卡塞格侖反射鏡之放大倍 (M = 2.34) 率推算，所收集之雷射光長度為 0.04 mm，因此，本雷射系統之取樣體積約為 $0.02 \times 0.04 \times 0.04$ mm^3，最佳解析度為 0.02 mm。

三、結果與討論

本研究係將未反應氣體（CO_2 及 CH_4）由微管噴出，並在離微管出口高度 x/D = 1，2，3 處量測其拉曼散射光譜，拉曼散射之理論及其應用已有廣泛的介紹[10-12]，本文不再贅述。首先吾人將 CO_2 氣體由微管噴出，並在離微管出口高度 x/D = 1 處進行拉曼散射光譜量測，其拉曼譜線如圖 4 所示。吾人發現在雷射輸出能量為 160 mJ/pulse 時，CO_2 很容易被離子化(Ionization)，因此造成寬廣而無法確認 CO_2 之譜線出現。依本實驗所使用之雷射波長(248.56 nm)推算，CO_2 之拉曼譜線應出現在 257 nm 處，惟尚無法確認之峰值卻出現在 283 nm 處，造成如此寬廣譜線的可能反應步驟如下：

$$CO_2 + h\nu \rightarrow CO_2 + CO_2^+$$

$$CO_2 + h\nu \rightarrow C + O_2 + C^+ + O_2^+$$

$$CO_2 + h\nu \rightarrow CO + O + CO^+ + O^+$$

由於離子化後之 CO_2 拉曼譜線無法確認，同時在不同徑向位置 CO_2 之離子化程度亦不一樣，造成量測上的困難，因此必須將雷射光能量降低以避免將 CO_2 氣體離子化。

經過一連串降低雷射光能量測試之後，吾人發現當雷射光能量為 60 mJ/pulse 時，CO_2 不再離子化。因此，將量測點移至離微管出口 x/D = 3 處，並在徑向位置 r/D = 0.2 及 0.7 處進行量測，其量測結果與無 CO_2 噴流時所量測之光譜如圖 5 所示。圖 5a 為無 CO_2 噴流時所量測之室內空氣拉曼光譜，O_2、N_2 及 H_2O 之拉曼光譜各出現在 258.4、263.7 及 273.2 nm 處。當 CO_2 由微管噴出並將量測點移至接近噴流中心時(r/D = 0.2)，很強的 CO_2 拉曼訊號出現在 256.6 及 257.3 nm 處，由圖 5b 可見微量的外界空氣已捲入 CO_2 噴流中。但若量測點接近噴流與外界空氣之交會處(r/D = 0.7)，則 CO_2 與 O_2 之譜線相互重疊而造成訊號分辨上的困難(如圖 5c 所示)，由此可見 CO_2 氣體並不適合用來測試雷射系統之解析度。

接著吾人利用未燃之 CH_4 氣體來測試，吾人發現當雷射光能量為 60 mJ/pulse 時 CH_4 不但不會被離子化或點燃，其拉曼散射訊號亦非常強且其譜線亦未與其他譜線相互干擾(如圖 6 所示)，因此，吾人將 CH_4 流量固定在 2.1 lit/min，微管出口速度為 44.6 m/s，雷諾數為 2700，在離微管出口 x/D = 1、2、3 處沿著徑向方向(每次移動 0.1 mm)進行光譜量測，每一量測點雷射激發 200 次，平均後之光譜再經積分後 CH_4 之濃度分布如圖 7 所示。由圖 7 可見，CH_4 在三個不同高度之濃度呈高斯分布(Gaussian distribution)，由於 CH_4 噴流的密度比周圍空氣的密度為低，理論上當 CH_4 噴出微管時會造成浮力效應(Buoyancy effect)，但因本噴流為層流(Re = 2700)，且量測高度之區域受噴流動量所主控，以致像無浮力噴流(Non-buoyant jet)一樣，其濃度及速度呈高斯分布[13]。由於雷射量測系統之解析度為 0.02 mm，同時每隔 0.1 mm 量測一點，因此 1 mm 內便有具高度解析之 10 個量測點。反之，若解析度為 0.5 mm，既使每隔 0.1 mm 量測一點，也會因解析度不夠而造成量測誤差。

雖然本研究並未量測噴流之速度分布，但利用所量測之濃度分布(如圖 7 所示)及噴流之相似性(Similarity)可推算出噴流流場之速度分布。吾人可利用 x/D = 1、2、3 處所量之濃度得到濃度分布半徑(Half-radius of concentration)，在 x/D = 1、2、3 處之濃度分布半徑分別為 R_f = 1.2、1.24 及 1.26，將各個高度之濃度除以噴流中心之濃度及將噴流半徑除以濃度分布半徑之後，其結果如圖 8 所示。由圖 8 可見此噴流具有自似性(Self-similar)，同時由於速度及濃度分布在噴流中存有相似性，因此，速度分布可由下列公式表之：

$$\frac{U}{U_c} \cong \frac{f}{f_c} = \exp\left[-3.25\left(r/R_f\right)^2\right] \qquad (1)$$

其中 U_c 為噴流中心線速度。對圓管噴流而言，在無浮力效應區域之中心線速度可由下列公式表之[13]：

$$U_c = 6.2\left(\frac{r_0}{r_a}\right)^{1/2}\left(\frac{x}{D}\right)^{-1} U_0 \qquad (2)$$

其中 r_0 為噴流出口流體之密度，為 r_a 周圍空氣之密度，U_0 為噴流出口速度。以 CH_4 噴流而言，r_0/r_a = 0.544，U_0 = 44.6 m/s，則在 x/D = 1、2、3 處之中心線速度分別為 20.4、10.2、6.8 m/s，由式(1)所推算出之速度分布如圖 9 所示。

由實驗結果可知，經改良後之雷射系統其解析度足以解析 1 mm 之微管，未來本雷射系統可應用於寬度 1 mm、長度 20 mm 及不同深度之微槽出口的量測[14]。微槽係以微機電技術內鍍白金薄膜而成之微反應系統，白金係觸媒的一種，其可用來降低燃氣之反應活化能，在開發微米燃燒器的過程中扮演重要的角色。為了對微槽內觸媒燃燒反應有更進一步的瞭解，微槽內或其出口處之溫度或組成份濃度分布必須取得。惟若要使用雷射光學系統量測微槽內之溫度或組成份濃度則必須考慮微槽視窗是否足以承受雷射光強度及微槽內壁面光反射的問題，因此，在微槽出口處量測是較佳的選擇。利用雷射拉曼散射技術量測燃燒流場雖可同時取得溫度及組成份濃度之資訊，但拉曼散射訊號隨著溫度的升高而降低，同時量測微槽時之取樣體積亦非常微小，因此量測用來推算反應效率之 H_2O 時，其拉曼散射訊號是否足夠將影響量測之準確性。克服此困難之解決方法分別為利用 N_2 光譜吻合法(Spectrum-fit method)量測溫度及利用雙光子預解離水蒸汽法(Two-Photon Predissociative of Water Vapor)量測 H_2O 濃度。

四、結論

應用雷射拉曼散射技術於非反應微管噴流濃度之量測已完成，進而歸納出以下的結論：

1. 取樣體積為 $0.02 \times 0.04 \times 0.04$ mm^3 之解析度足以用來量測 D = 1 mm 微管出口之組成份濃度分布，未來本雷射系統可應用於寬度 1

mm、長度 20 mm 及不同深度之微反應槽出口的量測。

2. 過高之雷射光能量將造成 CO_2 離子化，但降低雷射光能量亦會降低拉曼散射訊號，進而影響量測之準確度，當應用於微反應槽量測時，其解決方法分別為利用 N_2 光譜吻合法(Spectrum-fit method)量測溫度及利用雙光子預解離水蒸汽法量測 H_2O 濃度。
3. 對層流之微管噴流而言，其非反應 CH_4 濃度呈高斯分布並具有自似性，由濃度分布可利用自似性推算出速度分布。

五、誌謝

本研究蒙國科會經費補助，計畫編號(NSC-90-2212-E-216-019)，以及成功大學航太系張智銘、張智國、李國源等研究生實驗協助，謹此致謝。

六、參考文獻

[1] http://sec353.jpl.nasa.gov/apc/Micropropulsion/00.html

[2] http://www.lerc.nasa.gov/WWW/Rt1996/5000/5330sc.html

[3] Bhatnagar, P. L., Gross, E. P., and Krook, M., 1954, “Model for collision processes in charged and neutral one-component systems,” *Phy. Rev*. 94:511-524.

[4] Bird, G. A., 1978, “Monte Carlo simulation of gas flows,” *Annu. Rev. Fluid Mech.* 10:11-31.

[5] Coronell, D. G. and Jensen, K. F., 1992, “Analysis of transition regime flows in low pressure chemical deposition reactors using the direction simulation Monte Carlo method,” *J. Electrochem. Soc.* 139:2264-2273.

[6] Johannes, J., Bartel, T. J., Economou, D. J., Lumberopoulos, D. P. and Wise, R. S., 1996, “Simulation images from a low-pressure chlorine plasma reactor using DSMC,” *IEEE trans. Plasma Sci.* 24:127-128.

[7] Oh, C. K., Oran, E. S. and Cybyk, B. Z., 1995, “Microchannel flow computed with the DSMC-MLG,” *AIAA pap. No. 95-2090*, Reston, VA.

[8] Shih, J. C., Ho, C. M., Liu, J. and Tai, Y. C., 1995, “Non-linear pressure distribution in uniform microchannels,” *ASME AMD-MD 238*.

[9] Lahiji, G. R. and Wise, K. D., 1980, “A monolithic thermopile detector fabricated using integrated-circuit technology,” *Proc. Int. Electron Dev. Meet.* Washington, D. C. pp. 676-679, New York.

[10] J. A. Wehrmeyer, T. S. Cheng, and R. W. Pitz, (1992), "Raman Scattering Measurements in Flames Using a Tunable KrF Excimer Laser," *Applied Optics*, Vol. 31, pp. 1495-1504.

[11] T. S. Cheng, J. A. Wehrmeyer, and R. W. Pitz, (1992), "Simultaneous Temperature and Multi-Species Measurement in a Lifted Hydrogen Diffusion Flame," *Combustion and Flame*, Vol. 91, pp. 323-345.

[12] T. S. Cheng, J. A. Wehrmeyer, R. W. Pitz, O. Jarrett, Jr., and G. B. Northam, (1994), "Raman Measurement of Mixing and Finite-Rate Chemistry in a Supersonic Hydrogen/Air Diffusion Flame", *Combustion and Flame*, Vol. 99, pp.157-173.

[13] Chen, C. J. and Rodi, W. (1980), *Vertical Turbulent Buoyant jets. A Review of Experimental Data*, Pergamon press, new York.

[14] 廖仁瑞，〞微機電技術製作之白金觸媒反應系統〞，國立成功大學航太工程學系碩士論文(2002)。

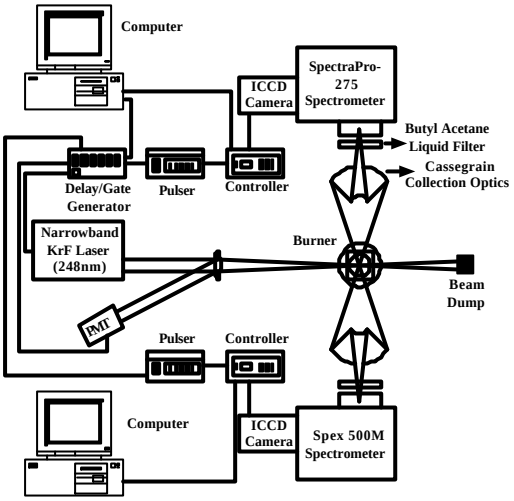

圖 1 UV Raman 系統配置圖

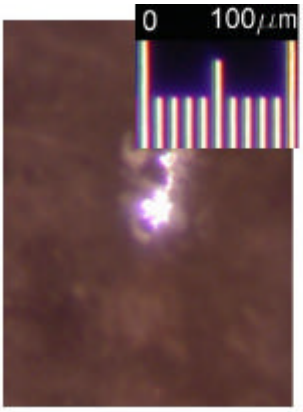

圖 2 雷射光經焦距 200 mm 之鏡片聚焦後之焦點尺寸

圖 3 口徑 1 mm 微管之裝置圖

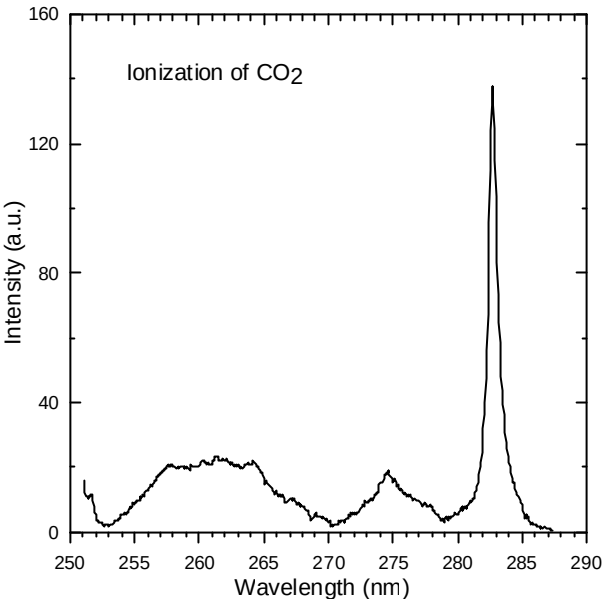

圖 4 CO_2 離子化之後的譜線

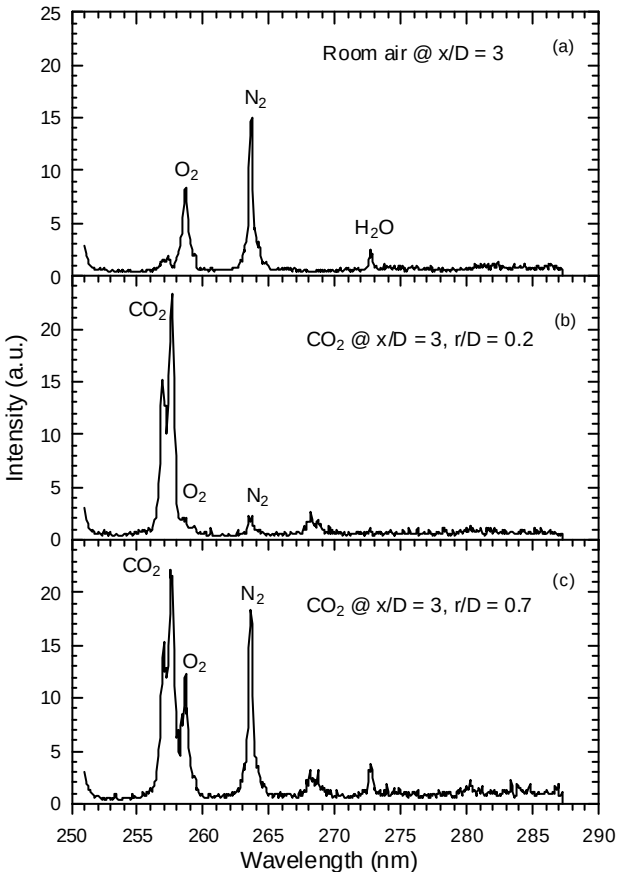

圖 5 空氣及微管噴流為 CO_2 之拉曼散射光譜

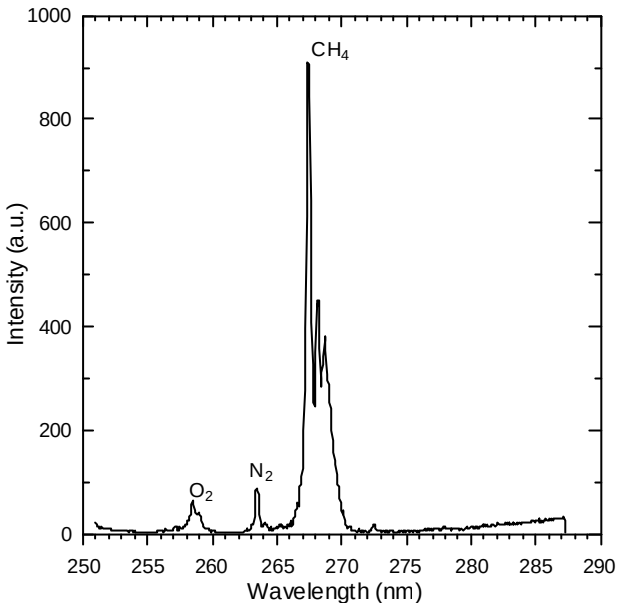

圖 6 微管噴流為 CH_4 之拉曼散射光譜

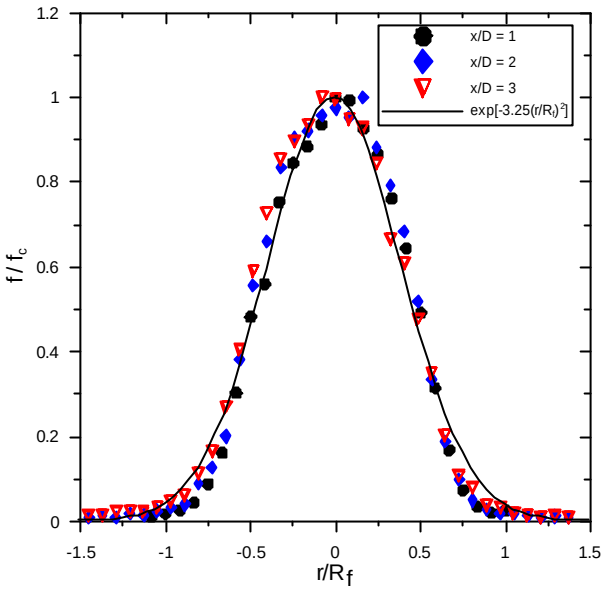

圖 8 在離微管出口 x/D = 1、2、3 處沿著徑向方向歸一化後 CH_4 之濃度分布

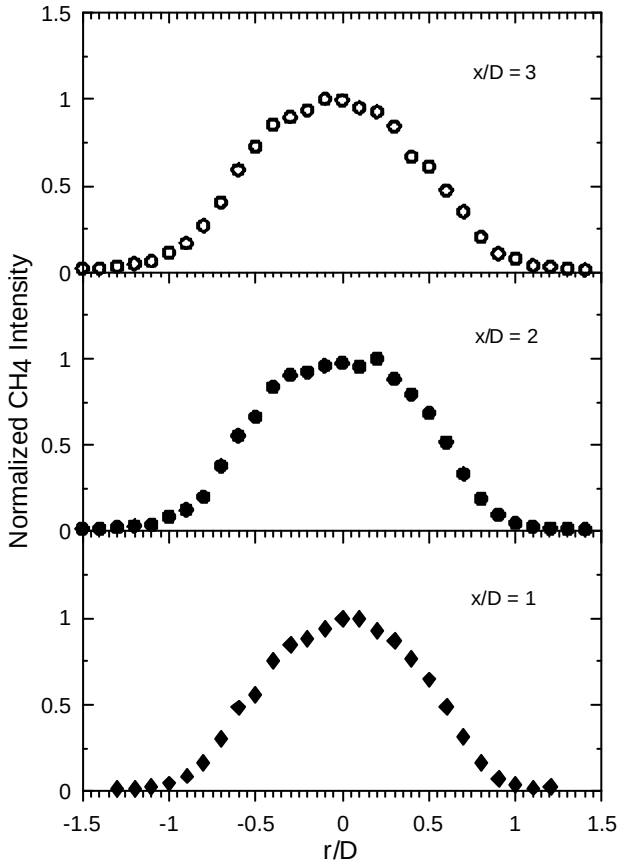

圖 7 在離微管出口 x/D = 1、2、3 處沿著徑向方向之 CH_4 濃度分布

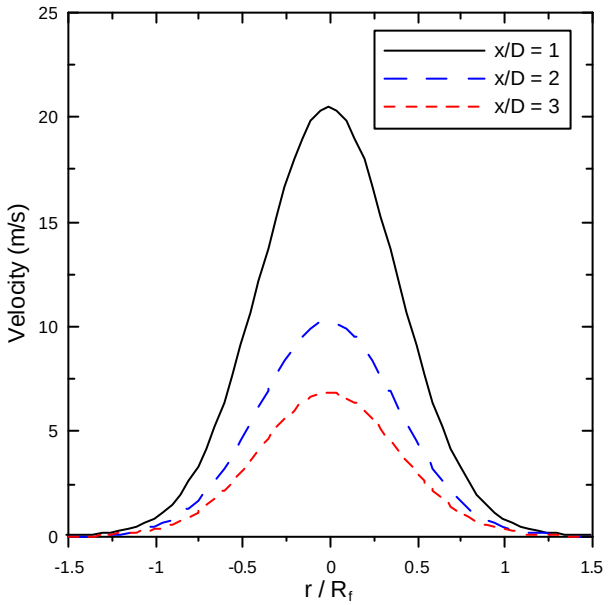

圖 9 利用 CH_4 之濃度分布及自似性所推算出之速度分布

Preliminary Study of Micro Reacting System Using laser Diagnostic Techniques

T. S. Cheng
Department of Mechanical Engineering, Chung Hua University

Y.-C. Chao, C.-Y. Wu, G.-B. Chen, T. Yuan, and T. S. Leu
Institute of Aeronautics and Astronautics, Space Science and Technology Center, National Cheng Kung University

Abstract

The development of micro-electro-mechanical systems (MEMS)-based micro reacting system has been underway for several years. In order to investigate the effects of velocity, pressure, and chemical reaction on the performance of micro combustor, the state properties such as velocity, pressure, temperature, and species concentrations must be measured. A goal of this paper is to study the potential of applying laser diagnostic techniques to micro reacting system. A sample volume of 0.02 $\times$ 0.04 $\times$ 0.04 mm^3 is used to resolve the flowfields produced from 1 mm diameter tube. Radial profiles of CH_2 concentrations are obtained to test the applicability of the laser system. It demonstrates that present laser system is capable of analysis micro reacting channel.

Keywards: MEMS, Laser Diagnostic Technique, Microcombustor

中華民國燃燒學會第 13 屆學術研討會，台北市，March 29, 2004

Raman-LIPF Measurements of Temperature, Major species, and OH in a Laminar Hydrogen Jet Diffusion Flame

T. S. Cheng
Department of Mechanical Engineering, Chung Hua University

Y.-C. Chao, C.-Y. Wu, G.-B. Chen, T. Yuan, and T. S. Leu
Institute of Aeronautics and Astronautics, National Cheng Kung University

Abstract

Simultaneous, temporally and spatially resolved point measurements of temperature, major species concentrations (N_2, O_2, H_2O, H_2), and hydroxyl radical concentration (OH) are obtained in a laminar hydrogen jet diffusion flame using combined ultraviolet (UV) spontaneous vibrational Raman scattering and laser-induced predissociative fluorescence (LIPF) techniques. Radial profiles are measured at three axial locations for a jet exit Reynolds number of 330. The measurements indicate that the unburned fuel within the potential core experiences significant preheating as it travels into downstream. Near the burner exit, the OH peaks outer the stoichiometric contour defined by the intersection of the H_2 and O_2 concentration profiles. Significant radial diffusion and hence flame expansion is found for such a small burner flame. The detailed measurements of the flame properties provide information for validation of combustion models.

Keywords: Laminar hydrogen flame, Raman scattering, LIPF.

1. Introduction

Laser-based non-intrusive techniques, with adequate temporal and spatial resolution, have been applied to measure the state properties of gases in combustion environments for many years [1]. One laser-based technique, spontaneous Raman scattering, has the capability of providing simultaneous measurements of temperature and all major species concentrations in hydrogen and hydrocarbon diffusion flames. Although Raman scattering has a relatively weak signal, it has been applied to simultaneously measure temperature and all major species concentrations in turbulent hydrogen diffusion flames [2-7], hydrogen diluted with argon flames [8-10] and hydrocarbon flames [11-14].

From the search of published literatures, most reports are on the measurements of turbulent flames. There is a need to provide laminar flame data for validation of combustion models. A goal of this paper is to provide a fine resolution and accurate database for comparisons with comprehensive numerical models of laminar hydrogen jet diffusion flame. In addition, the fine resolutions of the laser system may apply to the Micro-Electro-Mechanical Systems (MEMS) based micro reacting systems.

2. Experimental Apparatus

The schematic diagram of the UV Raman system is shown in Figure 1. A narrowband KrF excimer laser (Lambda Physik LPX-250T) produces UV light that is tunable from 247.9 to 248.9 nm with a bandwidth of 0.003 nm. The maximum pulse energy is 450 mJ with pulse duration of 20 ns. For the present experiment, the laser pulse energy is set to 150 mJ to avoid

laser-induced air breakdown. The laser is tuned to 248.56 nm to minimize fluorescence interference from OH and O_2. Light scattered by the 200 mm focusing lens is measured by a PMT to provide a relative measure of the laser pulse energy. The laser is focused toward either the multi-element, uncooled, flat-flame diffusion "Hencken" burner or the jet. The "Hencken" burner produces a homogenous laminar post flame zone that is used for evaluation and calibration of the Raman system.

The laser beam is focused by a single 200 mm spherical lens to a 0.02×0.04 mm profile in the sample volume where the largest dimension is parallel to the direction of the jet flow. The probe length as determined by the magnification ratio of collection optics (2.34) and the opening slit of spectrometer (100 μm) is 0.04 mm in the direction of beam propagation. Stokes Raman and fluorescence signals emanating from the sample volume are collected and focused by a Cassegrainian optics (magnification ratio 2.34) through a 10 mm thick butyl acetate liquid filter and relayed to the entrance slit of a 0.275 m, f/3.8 spectrometer (Acton Research Co., SpectraPro-275) with a 1200 grooves/mm grating (3 nm/mm dispersion) and a 0.5 m, f/4 spectrometer (SPEX-500M) with a 1800 grooves/mm grating (1.1 nm/mm dispersion) for dispersion and separate measurement. An intensified CCD camera (Princeton Instruments, 576 x 384 array, 22 x 22 μm pixels) is aligned at the exit plane of the spectrometer for monitoring the Stokes Raman and fluorescence signals. The Raman and fluorescence signals are digitized with a 14-bit A/D card connected to a personal computer for data reduction. The spectral coverage of the 0.5 m spectrometer is 13.8 nm, which is insufficient to measure all the major species Raman signals. Hence, it is used for the O_2 (258.4 nm) and N_2 (263.7 nm) Raman signal measurements. The spectral coverage of the 0.275 m spectrometer is 36.3 nm, which is used to measure H_2O (273.2 nm) and H_2 (277.1 nm) Raman signals as well as OH (297 nm) fluorescence in hydrogen flames. Both the 0.5 m and 0.275 m spectrometers are aligned by placing a 200 μm wire at the center of the probe volume and centering the image onto the respective slits. This procedure ensures that both N_2 Stokes and anti-Stokes Raman signals are measured from the same sample volume.

The flow facility is a 1 mm inner diameter vertical straight tube. Fuel is introduced through the jet into the still atmospheric air without coflow. The jet is mounted on a 3-D translation stage while the optical system remains fixed.

3. Calibration and Data Reduction

The Raman system is calibrated with the flat-flame "Hencken" burner operated at several known equivalence ratios from lean to rich. For each flame condition, the flame temperature is obtained by comparison of a measured N_2 Stokes spectrum with a calculated theoretical spectrum [15]. The spectral method is an excellent tool for laminar flame temperature measurement especially for flame temperatures higher than the thermocouple melting temperature. The measured flame temperature and measured flow rates are used to calculate equilibrium species concentrations and calibrate the Raman and OH fluorescence signals. For species concentration measurement, the integrated charge Q_i from an ICCD camera collecting the Raman scattering signal from species i is given by the equation [11]:

$$Q_i = K_i \, Q_l \, [N_i] \, f_i(T) \qquad (1)$$

where $[N_i]$ is the number density of species i, Q_l is the incident laser energy, K_i is a proportionality constant dependent on the vibrational Raman cross

section, geometry, and optical efficiency, and $f_i(T)$ is bandwidth factor which accounts for the temperature-dependent distribution of molecules in their allowed quantum states. The bandwidth factor can be theoretically calculated for diatomic molecules; however, the calculation is less reliable for polyatomic molecules. Hence, the terms K_i and $f_i(T)$ are combined to give the calibration factor $C_i = 1/K_i f_i(T)$ which is obtained from calibration.

For the OH concentration measurement, the use of laser-induced predissociative fluorescence (LIPF) technique has been described elsewhere [3]. The measured OH fluorescence intensity is related to the OH number density as follows:

$$I_F = C\frac{A}{A+Q+P} I_L [N_{OH}] f_B(T) \qquad (2)$$

where C is a constant dependent on optical and detector efficiency, A is the fluorescence rate, Q is the collisional quenching rate, P is the predissociating rate, I_L is the incident laser intensity, $[N_{OH}]$ is the OH number density, and $f_B(T)$ is the temperature dependent Boltzmann population fraction. Since P is about 20 times greater than A plus Q, hence Eq. (2) can be simplified as:

$$I_F = C\frac{A}{P} I_L [N_{OH}] f_B(T) \qquad (3)$$

The number density of OH molecules is linearly proportional to the measured intensity if fluorescence is measured from the v′ = 3 state. Since the laser is not tuned to a single resonant line, the OH fluorescence is from the excitation of the residual broadband output (~10 mJ) of the narrowband KrF excimer laser. The OH LIPF signal is linearly proportional to the OH concentration. The OH linear relationship is calibrated in the Hencken burner at 5 cm downstream where the OH radicals have recombined to an equilibrium concentration. The OH fluorescence signal is calibrated from lean to rich flame conditions. The O_2 fluorescence interferes with the OH fluorescence signal at high temperature lean conditions and is corrected by monitoring the O_2 fluorescence at 268 nm.

The perfect gas law is used to arrive at the temperature measurement by adding the number densities of the major species. The mixture fraction, f, is a conserved scalar that describes the state of mixing between fuel and oxidizer. The mixture fraction is calculated from the Raman scattering measurements of the major species concentrations for each laser shot as the mass originating from the fuel stream divided by the total mass [2,8]:

$$f = \frac{2[H_2] + 2[H_2O]}{32[O_2] + 28[N_2] + 18[H_2O] + 2[H_2]} \qquad (3)$$

The contribution of H_2O in the room air and the flame radicals (i.e., OH, H) to the mixture fraction calculation is small (< 0.001) and is neglected. The mixture fraction is 1 in pure hydrogen, 0 in pure air, and 0.0283 at stoichiometric.

The results of calibration of the single-pulse Raman system over a wide range of fuel/air ratios in the Hencken burner are shown in Figs. 2-5. At each fuel/air ratio, 200 laser shots are recorded. The mean and standard deviation values for each flame condition are presented by symbols and error bars and are compared to theoretical adiabatic equilibrium curves. The variations of mixture fraction are correlated to all major species concentrations according to Eq. (3). The experimental relative standard deviation for single-shot N_2 concentration measurements is 3% at room temperature and 7% in a stoichiometric flame at 2300 K (see Fig. 4c). The relative standard deviation for temperature and OH concentration measurements is 13% and 19% in the stoichiometric flame, respectively. The well-calibrated Raman system is then capable of analyzing flows where conditions are unknown.

4. Results and Discussion

A laminar hydrogen jet diffusion flame is formed by injecting fuel through a straight tube (D = 1 mm) into still atmospheric air. The jet has an exit velocity of 36 m/s, which is calculated based on the flowrate and the jet exit diameter (Reynolds number = 330). Raman and LIPF measurements are made in the radial direction at three axial locations: x/D = 1, 3, and 5. At each measurement location 200 independent laser shots are taken. For each single laser shot, the thermodynamic state properties (e.g., temperature and species concentrations) are measured in the flame. Other quantities such as density and mixture fraction can be calculated.

Figures 6-8 show the radial profiles of the mean temperature, major species (O_2, N_2, H_2O, H_2), and OH concentrations at different axial locations for the flame. Figure 6 details the radial profile across the potential core at x/D = 1. The temperature rapidly rises from the cool unburned core to 2155 K, where it plateaus across the reaction zone. As expected, the maximum flame temperature occurs at the stoichiometric contour defined by the intersection of the H_2 and O_2 concentration profile. At this axial position, the N_2 has diffused into the central jet and the OH peaks outer the stoichiometric contour. The peak OH concentration (X_{OH} = 0.00943) is about a factor of 1.56 higher than the equilibrium value that corresponds to a measured mixture fraction. This superequilibrium OH concentration is caused by the slow three-body recombination reactions and hence results in a lower flame temperature [3]. It is noted that the maximum OH concentration at this axial position do not coincide with the location of maximum temperature. This is due to more radial diffusion with a smaller burner than that with a larger burner [15].

Figure 7 shows the radial profile for the flame at x/D = 3. At this axial location, the centerline H_2 mole fraction decreases to 0.371 and the temperature rises to 1640 K. The maximum temperature has reached to 2323 K and is also located at the stoichiometric contour but not coincided with the peak OH location. The depressing of temperature at outer flame zone is also due to superequilibrium OH effect. The maximum value of OH is 0.0087.

Figure 8 shows the radial profile for the flame at x/D = 5. At this axial location, the centerline H_2 mole fraction decreases to 0.279 and the temperature rises to 1782 K. Here, the peak temperature (T = 2310 K) slightly shifts outward away from the stoichiometric contour. However, the maximum OH and H_2O concentrations at this axial position coincide with the location of maximum temperature. Note that the maximum value of OH has decreased from 0.0087 to 0.004 and results in a temperature close to an adiabatic equilibrium value.

5. Conclusions

UV Raman scattering combined with LIPF has been applied to a laminar hydrogen jet diffusion flame. The spatial resolution is improved over previous UV Raman system. Simultaneous, temporally and spatially resolved point measurements of temperature, major species concentrations (O_2, N_2, H_2O, H_2), and hydroxyl radical concentration (OH) are measured. In addition to obtaining an accurate and detailed mapping of temperature and species concentrations, we found that fuel has not been completely consumed at the measured three axial positions. We also found that the maximum OH concentration does not coincide with the location of maximum

temperature at x/D = 1 and 3. The detailed measurements of the flame properties provide information for combustion models validation.

Acknowledgements

This research was supported by the National Science Council of the Republic China under Grant Number NSC-90-2212-E-216-019, NSC-90-2212-E-006-156, NSC-90-2212-E-006-159

References

[15] Eckbreth, A. C. (1996) *Laser Diagnostics for combustion temperature and species*. 2nd ed., Gordon and Breach Publishers, New York.

[16] Drake, M. C., Pitz, R. W., and Lapp, M., *AIAA J*. 24:905-917 (1986).

[17] Cheng, T. S., Wehrmeyer, J. A., and Pitz, R. W. (1992) Simultaneous temperature and multi-species measurements in a lifted hydrogen diffusion flame. *Combust. Flame*, **91**, 323-345.

[18] Cheng, T. S., Wehrmeyer, J. A., Pitz, R. W., Jarrett, O., and Northam, G. B. (1994) Raman measurement of mixing and finite-rate chemistry in a supersonic hydrogen-air diffusion flame. *Combust. Flame*, **99**, 157-173.

[19] Barlow, R. S. and Carter, C. D. (1994) Raman/Rayleigh/LIF measurements of nitric oxide in turbulent hydrogen jet flames. *Combust. Flame*, **97**, 261-280.

[20] Nandula, S. P., Brown, T. M., and Pitz, R. W., (1994). Measurements of scalar dissipation in the reaction zone of turbulent nonpremixed H_2-air flames. *Combust. Flame*, **99**, pp. 775-783.

[21] Brockhinke, A., Andresen, P., and Kohse-Höinghaus, K. (1995) Quantitative one dimensional single-pulse multi-species concentration and temperature measurement in the lift-off region of a turbulent H_2/air diffusion flame. *Appl. Phys*. B **61**, 533-545.

[22] Magre, P., and Dibble, R. W., (1988) *Combust. Flame* 73:195-206.

[23] Barlow, R. S., Dibble, R. W., Chen, J.-Y., and Lucht, R. P., (1990) *Combust. Flame* 82:235-251.

[24] Chen, Y.-C. and Mansour, M. S., (1996). Measurements of the detailed flame structure in turbulent H_2-Ar jet diffusion flames with line-Raman/Rayleigh/LIPF-OH technique. *Proceedings of the Combustion Institute*, **26**, 97-103.

[25] Dibble, R. W., Masri, A. R., and Bilger, R. W., *Combust. Flame* 67:189-206 (1987).

[26] Bergmann, V., Meier, W., and Stricker, W., (1998) Application of spontaneous Raman and Rayleigh scattering and 2D LIF for the characterization of a turbulent $CH_4/H_2/N_2$ jet diffusion flame. *Appl. Phys. B* 66:489-502.

[27] Nguyen, Q. V., Dibble, R. W., Carter, C. D., Fiechtner, G. J. and Barlow, R. S. (1996) Raman-LIF measurements of temperature, major species, OH, and NO in a methane-air bunsen flame. *Combust. Flame*, **105**, 499-510.

[28] Nooren, P. A., Versluis, M., van der Meer, T. H., Barlow, R. S., and Frank, J. H., (2000) Raman-Rayleigh-LIF measurements of temperature and species concentrations in the Delft piloted turbulent jet diffusion flame. *Appl. Phys. B*, DOI 10.1107/s003400000278.

[29] Agrawal, A. K., Cherry, S. M., and Gollahalli, S. R., (1998) Effects of Buoyancy on Steady Gas jet Diffusion Flames. *Combust. Sci. Tech.*, Vol. 140, pp. 51-68..

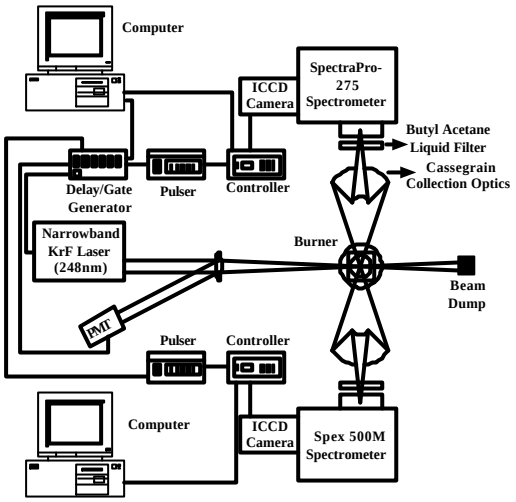

Fig. 1. Schematic diagram of UV Raman.

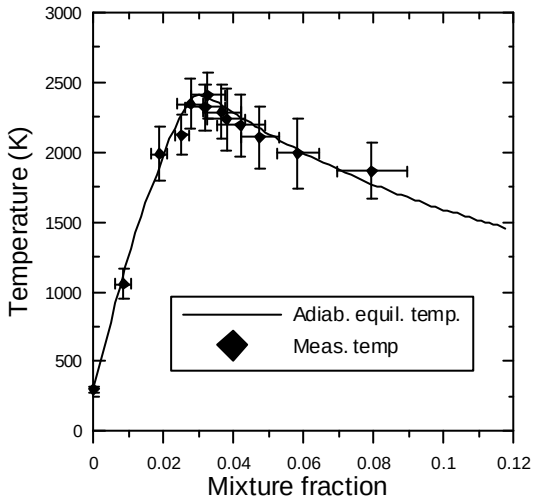

Fig. 2. Calibration result for temperature measurements.

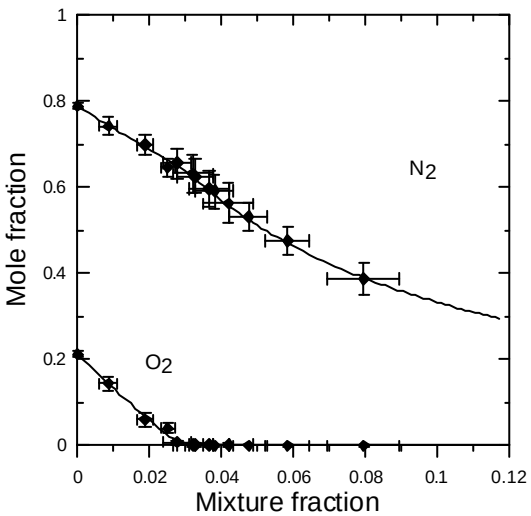

Fig. 3. Calibration result for O_2 and N_2 concentration measurements.

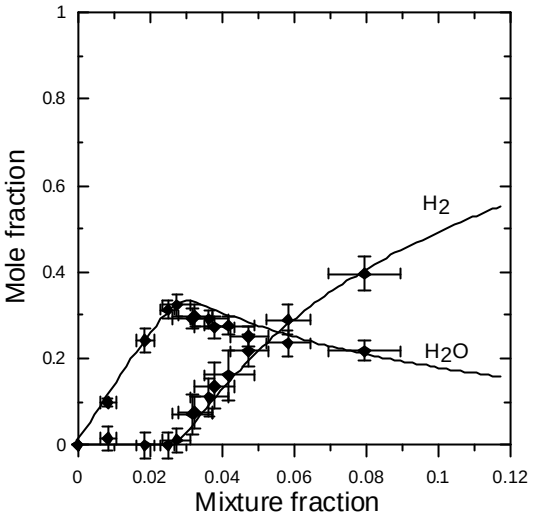

Fig. 4. Calibration result for H_2O and H_2 concentration measurements.

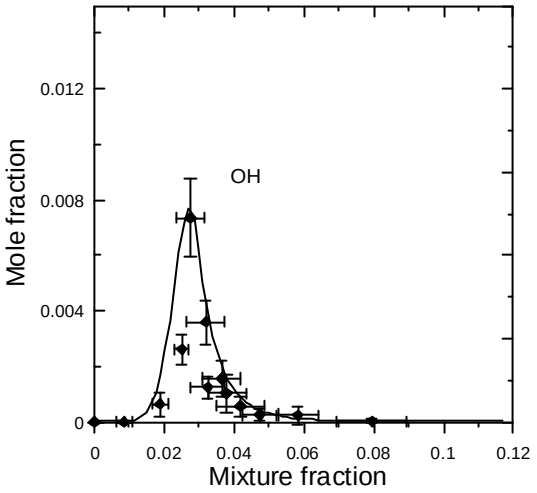

Fig. 5. Calibration result for OH concentration measurements.

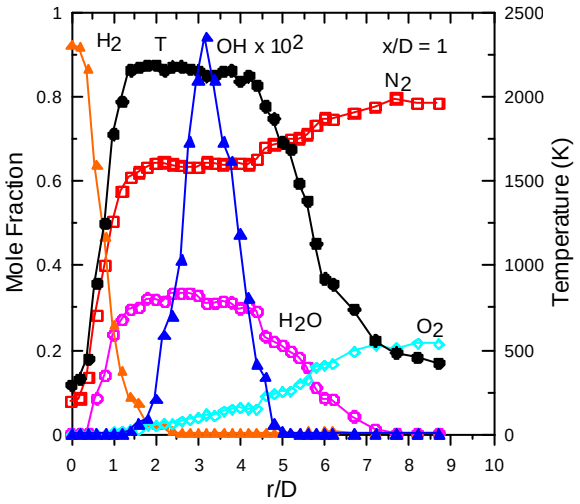

Fig. 6. Radial profiles of mean temperature, major species, and OH mole fractions at x/D = 1. The OH scale is magnified for clarity.

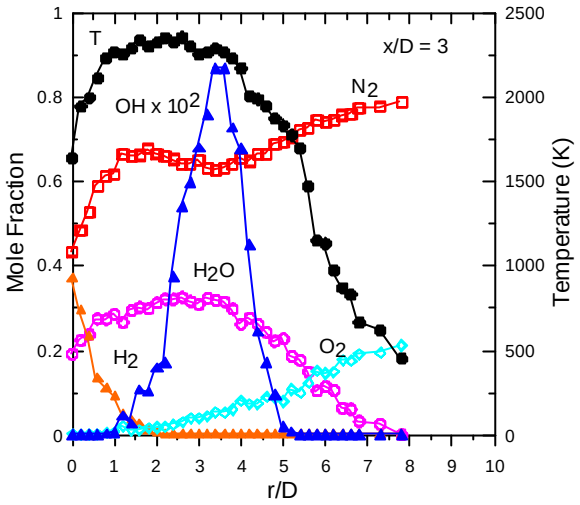

Fig. 7. Radial profiles of mean temperature, major species, and OH mole fractions at x/D = 3.

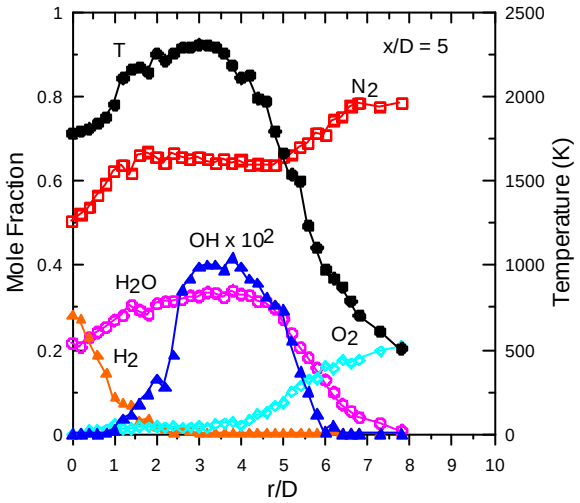

Fig. 8. Radial profiles of mean temperature, major species, and OH mole fractions at x/D = 5.

層流氫氣擴散火焰之溫度及組成份濃度量測

鄭藏勝
中華大學機械工程學系

趙怡欽、吳志勇、陳冠邦、袁曉峰、呂忠行
國立成功大學航太工程學系

摘要

利用結合拉曼散射及雷射誘發螢光技術不但具有時間及空間解析且可同時量測層流氫氣擴散火焰之溫度、主要組成份(N_2, O_2, H_2O, H_2)、及氫氧基(OH)濃度。本實驗量測雷諾數 300 之噴流火焰三個高度之溫度及組成份徑向分布，研究發現當勢流錐內未燃燒的燃料往下游流動時受到明顯的預熱，同時，接近噴嘴出口處，氫氧基的峰值位置並未與完全反應介面重合。吾人發現，小噴嘴之火焰具有可觀的徑向擴散以致造成火焰擴張。本研究之實驗數據可提供予燃燒模式驗證之用。

關鍵字：層流氫氣火焰、拉曼散射、雷射誘發螢光

UV RAMAN/LIPF DIAGNOSTICS IN A MESOSCALE NONPREMIXED HYDROGEN JET FLAME

T. S. Cheng*

Department of Mechanical Engineering
Chung Hua University

Y.-C. Chao, C.-Y. Wu, G.-B. Chen, T. Yuan, and T. S. Leu

Institute of Aeronautics and Astronautics
National Cheng Kung University

* 707, Sec. 2, Wufu Rd., Tungshiang, Hsinchu, Phone: 886-3-5186489, Fax: 886-3-5373771, E-mail: tscheng@chu.edu.tw

ABSTRACT

The application of single-pulse UV Raman scattering and laser-induced predissociative fluorescence (LIPF) techniques for future study of micro channel/tube reacting flows is examined with a probe volume of $0.02 \times 0.04 \times 0.04$ mm^3. A 1 mm diameter tube is used for the present investigation. UV Raman scattering combined with LIPF is applied to a mesoscale H_2 jet diffusion flame. Simultaneous, temporally and spatially resolved point measurements of temperature, major species concentrations (O_2, N_2, H_2O, H_2), and hydroxyl radical concentration (OH) are made in the radial and axial directions. Quantitative OH concentration measurement and qualitative 2-D OH imaging indicate that two reaction zones (diffusion and premixed) coexist in this small tube flame, due to flame quenching and subsequently air leaking into the fuel stream. Comparisons between the measured and calculated data indicate that the flamelet approach predicts favorable results for temperature and major species concentrations except for OH radicals. The present study demonstrates that future application of this Raman/LIPF system to micro catalytic channel/tube flows is feasible.

Keywords: Raman scattering, LIPF, mesoscale nonpremixed flame, micro reacting flows

中尺度非預混氫氣噴流火焰之雷射診測

鄭藏勝
中華大學機械工程學系

趙怡欽、吳志勇、陳冠邦、袁曉峰、呂宗行
國立成功大學航太工程學系

摘要

本文利用具有極佳空間解析度之拉曼散射及雷射誘發螢光技術來探討其應用於微反應流場之可行性。本實驗量測直徑 1mm 微管所產生之中尺度非預混氫氣噴流火焰軸向及徑向之溫度、主要組成份(N_2, O_2, H_2O, H_2)、及氫氧基(OH)濃度分布。定量及二維定性之 OH 量測顯示此火焰存在雙層反應區。比較實驗數據與計算結果發現，火焰片模式除了對 OH 的預測失真之外，對溫度及主要組成份的預測皆有合理的結果。本研究顯示可應用此系統於微反應流場之量測。

關鍵字：拉曼散射、雷射誘發螢光、中尺度非預混火焰、微反應流

INTRODUCTION

With increasing demands on micro devices such as micro satellite and micro airplane, needs for a micro power source to activate these systems have been increased as well [1]. These systems require high energy density power source to provide a long period of time of operation. Generally, the energy density of typical hydrocarbon fuels is about 100 times higher than that of batteries. Even regarding the heat losses in the process of extracting power from the fuel, a micro scale propulsion system has been considered as a viable alternative to the batteries [2]. Various propulsion devices such as micro heat engine, gas turbine, rocket engine, and thruster have been successfully demonstrated [2, 3]. Along the development of micro propulsion systems, one of the major problems is the combustion in a miniature volume of combustor. Two new challenges such as the limited flow residence time for complete combustion within the combustor and an increase of heat loss to the walls of the combustor due to increased surface area-to-volume ratio are encountered. Existing literature on combustion is insufficient for understanding the physical phenomena in a volume that is comparable to a laminar flame thickness. Intensive theoretical and numerical efforts have been underway to face the new challenges [4, 5]. However, these models require benchmark data for assessments. Therefore, experimental measurements of pressure, velocity, temperature and reactive scalars either inside the combustor or in the combustor exhaust are needed not only to gain a better insight into the physics but also to provide information for the input and validation of theoretical models.

Laser-based non-intrusive techniques, with adequate temporal and spatial resolution, have been applied to measure the state properties of gases in combustion environments for many years [6]. One laser-based technique, spontaneous Raman scattering, has the capability of providing simultaneous measurements of temperature and all major species concentrations in hydrogen and hydrocarbon diffusion flames. Although Raman scattering has a relatively weak signal, it has been applied to simultaneously measure temperature and all major species concentrations in turbulent hydrogen diffusion flames [7-9], hydrogen diluted with argon flames [10, 11] and hydrocarbon flames [12-15]. From the search of published literatures, all reports are on the measurements of large-scale turbulent flames. There is a need to verify whether such a system can also be applied to micro reacting flows.

In the present study, we attempt to apply spontaneous Raman scattering technique to a jet flame that is produced from a 1 mm diameter tube. The laser system is then applied to a laminar nonpremixed hydrogen jet flame. Simultaneous measurements of temperature and multi-species concentrations in the flame provide fine resolution and accurate database for validation of combustion models. The present study demonstrates that future application of this system to micro channel/tube reacting flows is feasible.

EXPERIMENTAL APPARATUS

The schematic diagram of the UV Raman system is shown in Figure 1. A narrowband KrF excimer laser produces UV light that is tunable from 247.9 to 248.9 nm with a bandwidth of 0.003 nm. The maximum pulse energy is 450 mJ with pulse duration of 20 ns. For the present experiment, the laser pulse energy is reduced to avoid laser-induced air breakdown. The laser wavelength is tuned to 248.56 nm to minimize fluorescence interference from OH and O_2 and two-photon H_2O photodissociation. Light scattered by the 200 mm focusing lens is measured by a PMT to provide a relative measure of the laser pulse energy. The laser beam is focused by a single 200 mm spherical lens to a 0.02×0.04 mm profile in the sample volume where the largest dimension is parallel to the direction of the jet flow. The probe length as determined by the magnification ratio of collection optics (2.34) and the opening slit of spectrometer (100 μm) is 0.04 mm in the direction of beam propagation. Stokes Raman and fluorescence signals emanating from the sample volume are collected and focused by a Cassegrainian optics (magnification ratio 2.34) through a 10 mm thick butyl acetate liquid filter and relayed to the entrance slit of a 0.275 m, f/3.8 spectrometer with a 1200 grooves/mm grating and a 0.5 m, f/4 spectrometer with a 1800 grooves/mm grating for dispersion and separate measurement. An intensified CCD camera (Princeton Instruments, 576 x 384 array, 22 x 22 μm pixels) is aligned at the exit plane of the spectrometer for monitoring the Stokes Raman and fluorescence signals. The Raman and fluorescence signals are digitized with a 14-bit A/D card connected to a personal computer for data reduction. The flow facility is a 1 mm inner diameter vertical

straight tube. Fuel is introduced through the tube into the still atmospheric air without coflow. The jet is mounted on a 3-D translation stage while the optical system remains fixed. The resolution of translation stage is 1 μm.

CALIBRATION AND DATA REDUCTION

For hydrogen flame measurements, the Raman system is calibrated with the flat-flame "Hencken" burner operated at several known equivalence ratios from lean to rich. The calibration procedure for major species (N_2, O_2, H_2, and H_2O) and OH concentration measurements is similar to that described elsewhere [8]. The perfect gas law is used to arrive at the temperature measurement by adding the number densities of the major species. The experimental relative standard deviation for single-shot N_2 concentration measurements is 3% at room temperature and 7% in a stoichiometric flame at 2300 K. The relative standard deviation for temperature and OH concentration measurements is 9% and 19% in the stoichiometric flame, respectively. Typical single-shot relative standard deviations in this range are comparable to other UV Raman systems [16, 11]. The well-calibrated Raman system is then capable of analyzing hydrogen jet flames.

In addition, the qualitative 2-D OH imaging is also employed to visualize the flame structure [18]. For the OH imaging, the laser wavelength is tuned to 248.46 nm to excite the $P_2(8)$ rotational line of the A-X (3,0) transition. The laser beam is formed to a thin sheet of 34 mm height and 0.2 mm thick by a single cylindrical lens (f = 1000 mm) and intersected vertically through the flame axis. Only the 20 mm central portion of the laser sheet, where the laser intensity is high and uniform, is used for imaging. The OH fluorescence signal is imaged onto an intensified CCD camera with a UV camera lens (Nikkor, f = 105 mm, f/4.5). A 10-mm-thick butyl acetate liquid filter is placed in front of the camera to reject the Rayleigh light.

RESULTS AND DISCUSSION

Before applied the present system to hydrogen jet flame measurement, we examine the flat-flame first. The laser energy is set to 200 mJ/pulse corresponding to a power density of 1.25 TW/cm^2 in the probe volume. No gas breakdown is found from the visual observation and spectra measurements. A laminar hydrogen jet diffusion flame is formed by injecting fuel through a straight tube into still atmospheric air. The jet has an exit velocity of 36 m/s, which is calculated based on the flowrate and the jet exit diameter (*Re* = 330). Raman and LIPF-OH point measurements are made in the radial and axial directions. At each measurement location 200 independent laser shots are taken. For each single laser shot, the thermodynamic state properties (e.g., temperature and species concentrations) are measured in the flame. Other quantities such as density and mixture fraction can be calculated. Figures 2-5 show the measured radial profiles of the mean temperature, major species (O_2, N_2, H_2O, H_2), and OH concentrations with the calculated results obtained from a postprocessing of flamelet model for the flame. The experimental data are indicated by symbols and those from the flamelet model are denoted by solid lines. The predicted data are derived from the measured mixture fraction and a flamelet library. Figure 2 details the radial profile across the potential core at *x/D* = 1. The temperature rapidly rises from the cool unburned core to 2008 K, where it plateaus across the reaction zone. As expected, the maximum flame temperature and the peak OH location occur at the stoichiometric contour defined by the intersection of the H_2 and O_2 concentration profile. The peak OH concentration (X_{OH} = 0.018) is about a factor of 3 higher than the adiabatic equilibrium value that corresponds to a measured mixture fraction of 0.029. This superequilibrium OH concentration is caused by the slow three-body recombination reactions and hence results in a flame temperature (T = 2134 K) lower than the adiabatic equilibrium calculations (T = 2370 K). Comparisons between the predicted and measured data are in favorable agreement except that for OH concentration. The flamelet model predicts a broader distribution of OH radicals. The flamelet model predicts a broader distribution of OH radicals. It should be noted that one might argue that the superequilibrium OH is produced from the photofragment of two-photon H_2O photodissociation. If this were true, then the measured OH concentrations must be much higher than the flamelet predictions. Figure 2 declares that the superequilibrium OH concentration is caused by the slow three-body recombination reactions.

Figure 3 shows the radial profile for the flame at *x/D* = 5. At this axial location, the N_2 has diffused into the central jet and the temperature and peak OH shift toward outer radial position. The maximum temperature has reached to 2224 K and is also located with the peak OH at the stoichiometric contour. The depressing of temperature is also due

to superequilibrium OH effect. The maximum value of OH is 0.017. Comparisons of the predicted and measured data also indicate that the flamelet model predicts a broader OH distribution at this axial position. Figure 4 shows the radial profile for the flame at x/D = 25. At this axial location, the centerline temperature has increased to 1874 K and the centerline H_2 decreases to 0.155. Two temperature and OH peaks are found at the radial position of r/D = 1.4 and 4. This indicates that two reaction zones are formed in the flame at this downstream location. The flame structure measured at this axial location contradicts to a general concept that only one reaction zone exists in a laminar hydrogen diffusion flame. The reason for causing two reaction zones will be explained later with the 2-D OH imaging. Comparisons between the predicted and measured data are also in favorable agreement except that for temperature and OH concentration.

Figure 5 shows the radial profile for the flame at x/D = 50. At this axial location, the centerline temperature has increased to 1970 K and the centerline H_2 decreases to 0.065. One of the OH peaks has shifted toward the centerline of the jet, while the other is located at r/D = 1.6 where maximum temperature (T = 2161 K) occurs. Comparisons of the predicted and measured data indicate that the flamelet model under-predicts the H_2O and over-predicts the OH mole fractions at this axial position.

Figure 6 shows the axial profile along the centerline of the flame. The measured maximum temperature and OH concentration locate at x/D = 60, where is close to the axial position of the stoichiometric contour. Note that the predicted major species concentrations are in good agreement with the measured values. However, the flamelet model over-predicts the temperature and OH concentrations.

In order to verify the two reaction zones measured at x/D = 25 and 50 (Figures 4 and 5), the qualitative 2-D OH imaging is taken for the entire flame as shown in Figure 7. Figure 7 is an average of 20 single-pulse images and composes of 4 segments. The first segment is taken at 1 mm above the jet exit to reduce Mie scattering from the tube. Because the OH intensity reaches a maximum value in the flame front, the measured 2-D imaging of OH indicates the instantaneous shape of the reaction zone. The OH distribution in Figure 7 shows that two reaction zones exist in the flame; one is in the mixing layer between the fuel stream and the ambient air, and the other locates in the central flame from x/D = 20 to 45. The reaction zone formed in the mixing layer is normally found in a jet diffusion flame. High OH concentration appeared in the central portion of flame, which at first sight seems contradictory to diffusion flame structures, is due to flame quenching and subsequently air leaking from the upstream of the jet exit. In a laminar diffusion flame, with a smaller burner, the axial diffusion upstream of the burner exit is significant [19]. The flame envelope is extended to the negative direction of the jet exit and the flame can be quenched by the tube surface. As the jet exit velocity is high (Re = 330), the ambient air is sucked into the fuel stream from the contact surface of the flame and tube. The air is then mixed with fuel, convected downstream, and burned to form an inner premixed flame at x/D = 20 to 45.

CONCLUSIONS

UV Raman scattering combined with LIPF has been applied to a mesoscale hydrogen jet diffusion flame with a probe volume of $0.02 \times 0.04 \times 0.04$ mm^3. Simultaneous, temporally and spatially resolved point measurements of temperature, major species concentrations (O_2, N_2, H_2O, H_2), and hydroxyl radical concentration (OH) are measured in the radial and axial directions. In addition to obtaining an accurate and detailed mapping of temperature and species concentrations for combustion model assessment, we found that fuel has not been completely consumed up to x/D = 60. We also found that the measured maximum OH concentration coincides with the location of maximum temperature at radial and axial positions. Quantitative OH concentration measurement and qualitative 2-D OH imaging indicate that two reaction zones (diffusion and premixed) coexist in the flame, due to flame quenching and air leaking into the fuel stream. Comparisons between the measured and calculated data indicate that the flamelet approach predicts favorable results for temperature and major species concentrations except for OH radicals. The present study demonstrates that future application of this Raman/LIPF system to micro catalytic channel/tube flows is feasible.

ACKNOWLEDGEMENTS

This research was supported by the National Science Council of the Republic China under Grant

Number NSC-91-2212-E-216-010.

REFERENCES

[1] Kovacs, G. T. A. (1998) *Micromachined transducers-source book*. New York, McGraw-Hill.

[2] Epstein, A. H. et al., (1997) Micro-heat engines, gas turbines, and rocket engines. AIAA 97-1773, presented at 28th AIAA Fluid Dynamics Conference, 4th AIAA Shear Flow Control Conference, June29-July 2, Snowmass Village, CO.

[3] Wallance, A. P., Mukerjee, E. V., Yan, K., Smith, R. L. and Collins, S. D. (1999) Design, fabrication and demonstration of a vaporizing liquid attitude control microthruster. Transducers 99, Sendai, pp. 1800-1803.

[4] Lee, D. H., and Kwon, S. (2002) Heat transfer and quenching analysis of combustion in a micro combustion vessel. *J. Micromech. Microeng*. **12**, 670-676.

[5] Oran, E. S., Oh, C. K. and Cybyk, Z. C. (1998) Direct simulation Monte Carlo: recent advances and applications. *Annu. Rev. Fluid Mech*. **30**, 403-441.

[6] Eckbreth, A. C. (1996) *Laser diagnostics for combustion temperature and species*. 2nd ed., Gordon and Breach Publishers, New York.

[7] Drake, M. C., Pitz, R. W. and Lapp, M. (1986) Laser measurements on nonpremixed H_2-air flames for assessment of turbulent combustion models. *AIAA J.* **24**, 905-917.

[8] Cheng, T. S., Wehrmeyer, J. A. and Pitz, R. W. (1992) Simultaneous temperature and multi-species measurements in a lifted hydrogen diffusion flame. *Combust. Flame*, **91**, 323-345.

[9] Barlow, R. S. and Carter, C. D. (1994) Raman/Rayleigh/LIF measurements of nitric oxide in turbulent hydrogen jet flames. *Combust. Flame*, **97**, 261-280.

[10] Magre, P. and Dibble, R. W. (1988) Finite chemical kinetic effects in a subsonic turbulent hydrogen flame. *Combust. Flame*, **73**, 195-206.

[11] Chen, Y.-C. and Mansour, M. S. (1996) Measurements of the detailed flame structure in turbulent H_2-Ar jet diffusion flames with line-Raman/Rayleigh/LIPF-OH technique. *Proceedings of the Combustion Institute*, **26**, 97-103.

[12] Dibble, R. W., Masri, A. R. and Bilger, R. W. (1987) The spontaneous Raman scattering technique applied to nonpremixed flames of methane. *Combust. Flame*, **67**, 189-206.

[13] Bergmann, V., Meier, W. and Stricker, W. (1998) Application of spontaneous Raman and Rayleigh scattering and 2D LIF for the characterization of a turbulent $CH_4/H_2/N_2$ jet diffusion flame. *Appl. Phys. B*, **66,** 489-502.

[14] Nguyen, Q. V., Dibble, R. W., Carter, C. D., Fiechtner, G. J. and Barlow, R. S. (1996) Raman-LIF measurements of temperature, major species, OH, and NO in a methane-air bunsen flame. *Combust. Flame*, **105**, 499-510.

[15] Nooren, P. A., Versluis, M., van der Meer, T. H., Barlow, R. S. and Frank, J. H. (2000) Raman-Rayleigh-LIF measurements of temperature and species concentrations in the Delft piloted turbulent jet diffusion flame. *Appl. Phys. B*, DOI 10.1107/s003400000278.

[16] Nandula, S. P., Brown, T. M., Skaggs, P. A., Pitz, R. W. and DeBarber, P. A. (1994) Multi-species line Raman measurements in H_2-air turbulent flames, AIAA 32nd Aerospace Science Meeting, January 10-13, Reno, NV, AIAA Paper No. 94-0227.

[17] Cheng, T. S., Chao, Y.-C., Wu, D.-C., Yuan, T., Lu, C.-C., Cheng, C.-K. and Chang, J.-M. (1998) Effects of fuel-air mixing on flame structures and NO_x emissions in swirling methane jet flames. *Proceedings of the Combustion Institute*, **27**, 1229-1237.

[18] Agrawal, A. K., Al-Ammar, K., Gollahalli, S. R. and Griffin, D. (1999) Effects of buoyancy in hydrogen jet diffusion flames. *5th International Microgravity Combustion Workshop, NASA CP-208917*, pp. 109-112.

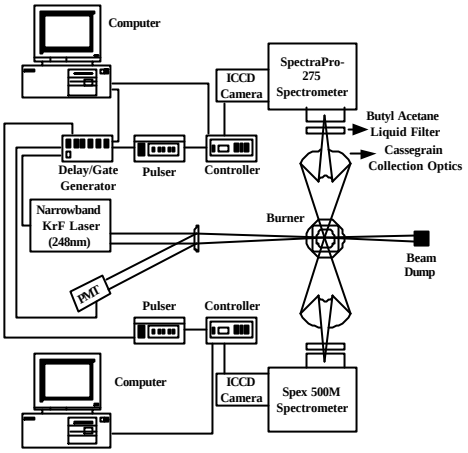

Figure 1. Schematic diagram of UV Raman.

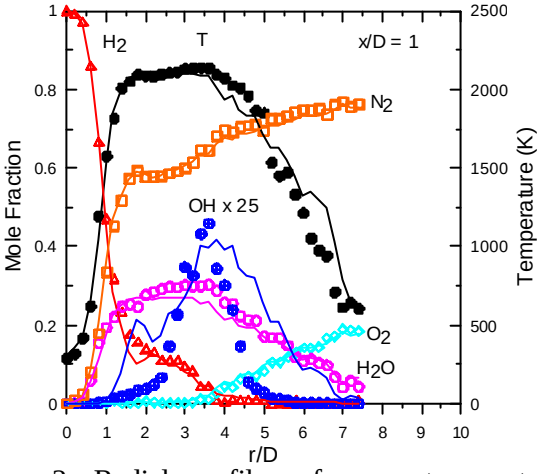

Figure 2. Radial profiles of mean temperature, major species, and OH mole fractions at $x/D = 1$.

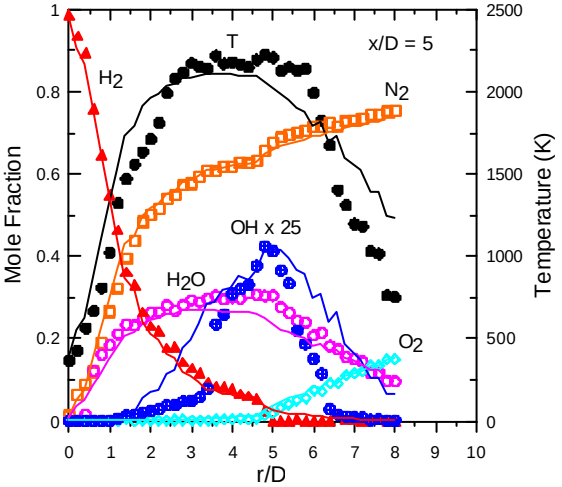

Figure 3. Radial profiles of mean temperature,

major species, and OH mole fractions at $x/D = 5$.

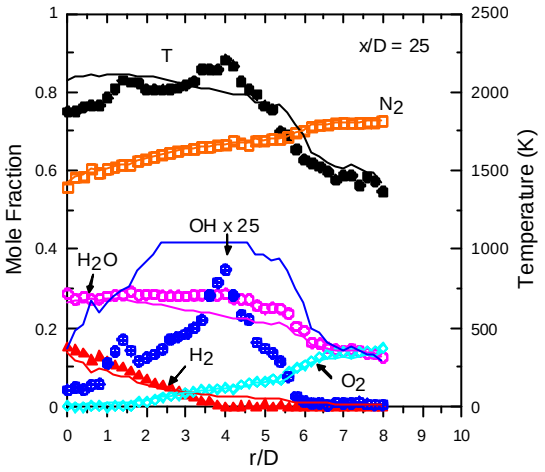

Figure 4. Radial profiles of mean temperature, major species, and OH mole fractions at $x/D = 25$.

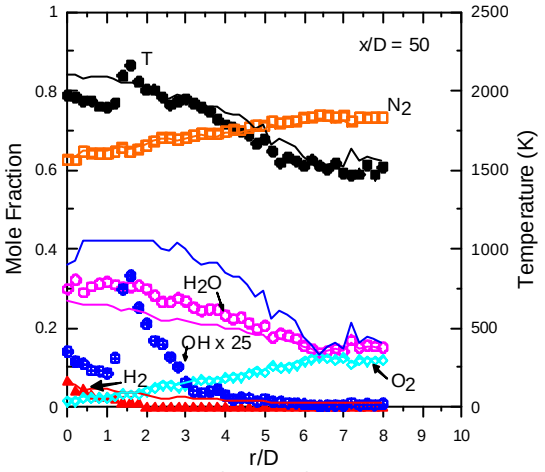

Figure 5. Radial profiles of mean temperature, major species, and OH mole fractions at $x/D = 50$.

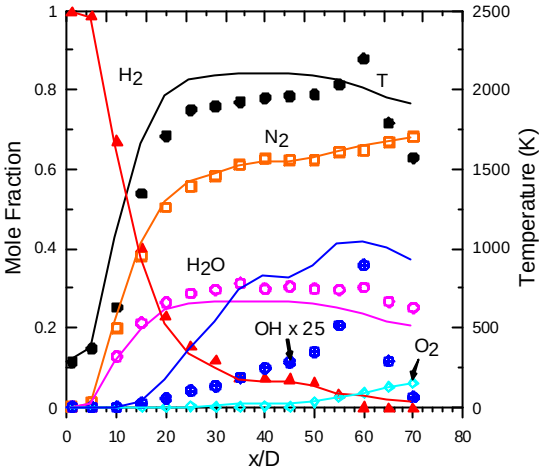

Figure 6. Axial profiles of mean temperature, major species, and OH mole fractions along the centerline of flame.

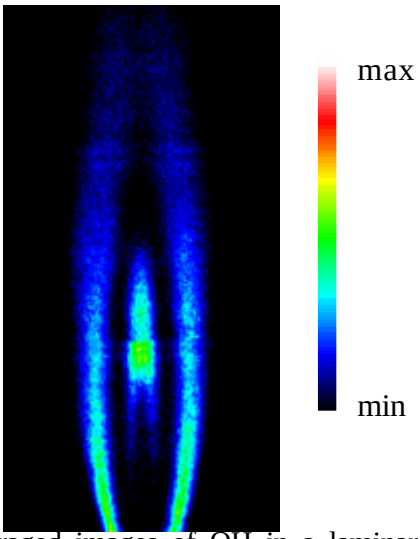

Figure 7. Averaged images of OH in a laminar hydrogen diffusion flame. The flow is upward. Intensity range, low → high: blue → green → yellow → red → white.

PROCI 34
12 August 2004 Disk Used
ARTICLE IN PRESS
No. of Pages 9; 4C: 5, DTD = 5.0.1
Jaya (CE) / Jayanthi (TE)

Available online at www.sciencedirect.com
SCIENCE DIRECT®

Proceedings of the Combustion Institute xxx (2004) xxx–xxx

Proceedings of the Combustion Institute

www.elsevier.com/locate/proci

Experimental and numerical investigation of microscale hydrogen diffusion flames

T.S. Cheng[a,*], Y.-C. Chao[b], C.-Y. Wu[b], Y.-H. Li[b], Y. Nakamura[c], K.-Y. Lee[b], T. Yuan[b], T.S. Leu[b]

[a] *Department of Mechanical Engineering, Chung Hua University, Hsinchu, Taiwan, ROC*
[b] *Institute of Aeronautics and Astronautics, National Cheng Kung University, Tainan, Taiwan, ROC*
[c] *EcoTopia Science Institute, Nagoya University, Nagoya, Japan*

Abstract

Characteristics of microscale hydrogen diffusion flames produced from sub-millimeter diameter ($d = 0.2$ and 0.48 mm) tubes are investigated using non-intrusive UV Raman scattering coupled with LIPF technique. Simultaneous, temporally and spatially resolved point measurements of temperature, major species concentrations (O_2, N_2, H_2O, and H_2), and absolute hydroxyl radical concentration (OH) are made in the microflames for the first time. The probe volume is $0.02 \times 0.04 \times 0.04$ mm^3. In addition, photographs and 2-D OH imaging techniques are employed to illustrate the flame shapes and reaction zones. Several important features are identified from the detailed measurements of microflames. Qualitative 2-D OH imaging indicates that a spherical flame is formed with a radius of about 1 mm as the tube diameter is reduced to 0.2 mm. Raman/LIPF measurements show that the coupled effect of ambient air leakage and pre-heating enhanced thermal diffusion of H_2 leads to lean-burn conditions for the flame. The calculated characteristic features and properties indicate that the buoyancy effect is minor while the flames are in the convection–diffusion controlled regime because of low Peclet number. Also, the effect of Peclet number on the flame shape is minor as the flame is in the convection–diffusion controlled regime. Comparisons between the predicted and measured data indicate that the trends of temperature, major species, and OH distributions are properly modeled. However, the code does not properly predict the air entrainment and pre-heating enhanced thermal-diffusive effects. Therefore, thermal diffusion for light species and different combustion models might need to be considered in the simulation of microflame structure.

Keywords: Microflames; Raman scattering; LIPF; Numerical simulation

1. Introduction

Recently, with increasing demands on microdevices such as microsatellite and microaerial vehicle, needs for a micropower source to activate these systems have significantly increased [1]. These microsystems require high-density power source to provide long periods of time of operation. Generally, the energy density of typical hydrocarbon fuels is about 100 times higher than that of batteries. Even regarding the heat losses in the process of extracting power

* Corresponding author. Fax: +886 3 5186521.
E-mail address: tscheng@chu.edu.tw (T.S. Cheng).

0082-0784/$ - see front matter © 2004 by the Combustion Institute. Published by Elsevier Inc. All rights reserved.
doi:10.1016/j.proci.2004.07.025

from the fuel, a microscale combustion system has been considered as a viable alternative to batteries. To develop such combustion systems, an understanding of the physics of microflames must be made.

There have been some studies of microflames experimentally, analytically, and numerically. Ban et al. [2] have performed experimental and theoretical studies on convection–diffusion controlled laminar microflames to investigate the magnitude of diffusive-transport and its effect on the microflame structure. They found that the buoyancy effect in the millimeter-size flames is negligible, while the axial diffusion is important in these flames. Ida et al. [3] conducted the extinction limit study of microdiffusion flames using microscopic shadowgraph and CH* emission imaging techniques. They reported that the quenching zone is located near the flame base, and the derived extinction curve can be described by Reynolds number times jet diameter. Matta et al. [4] used flame visualization and chemiluminescence measurement techniques along with analytical approaches to investigate the extinction process in microscale diffusion flames. They found that the measured quenching and blow-off limits are in agreement with the predicted values, and concluded that the behavior of miniature diffusion flames can be adequately modeled by the laminar jet diffusion flame theory. In addition to the experimental and theoretical studies, Nakamura et al. [5–7] have performed a series of numerical simulations to investigate the burner size effects on microflame structures using one-step and detailed reaction mechanisms. The predicted CH distribution and flame heights were in good agreement with experimental measurements.

In view of the above experimental studies, no detailed measurements of thermophysical properties of microscale diffusion flames were reported. Therefore, experimental measurements of temperature and reactive scalars are needed not only to gain a better insight into the physics but also to provide information for the input and validation of combustion models for CFD calculations. In the present study, we apply temporally and spatially resolved UV Raman scattering coupled with laser-induced predissociative fluorescence (LIPF) techniques to measure the thermophysical properties of microscale hydrogen diffusion flames. The results represent what we believe to be the first simultaneous measurements of temperature, major species (O_2, N_2, H_2O, and H_2), and OH concentrations in microscale hydrogen diffusion flames. Furthermore, numerical simulations of the microflames are performed and comparisons between the measured and predicted data are made to evaluate the capability of the CFD codes and to gain a better understanding of the characteristics of microflames.

2. Experimental setup

The microscale hydrogen diffusion flames investigated here are stabilized on vertical straight stainless-steel tubes with inner diameters (d) of 0.2 and 0.48 mm, and the corresponding wall thicknesses 0.09 and 0.17 mm. Fuel is introduced through the tube into the quiescent atmospheric air with mass flowrates of 0.043 and 0.107 mg/s corresponding to the bulk velocity of 16.48 and 7.16 m/s for $d = 0.2$ and 0.48 mm, respectively. The Reynolds number, based on the exit conditions of fuel, is $Re = 30$ for both flames. The jet is mounted on a precision 3-D translation stage while the optical system remains fixed. The resolution of the translation stage is 1 μm. For Raman/LIPF measurements, the scanning step is 50 and 100 μm for $d = 0.2$ and 0.48 mm, respectively.

The schematic diagram of the UV Raman/LIPF system is shown in Fig. 1. A narrowband KrF excimer laser (Lambda Physik LPX-250T) produces UV light that is tunable from 247.9 to 248.9 nm with a bandwidth of 0.003 nm. The maximum pulse energy is 450 mJ with a pulse duration of 20 ns. For the present experiment, the laser pulse energy is reduced to avoid laser-induced air breakdown. The laser wavelength is tuned to 248.56 nm to minimize fluorescence interference from OH and O_2, and two-photon H_2O photodissociation. Light scattered by the 200 mm focusing lens is measured by a photomultiplier tube (PMT) to provide a relative measure of the laser pulse energy. The laser is focused toward the multi-element, uncooled, flat-flame diffusion "Hencken" burner or the jet. The "Hencken" burner produces a homogeneous laminar post-flame zone that is used for evaluation and calibration of the Raman/LIPF system. The laser beam is focused by a single 200 mm spherical lens to a 0.02×0.04 mm profile in the sample volume where the largest dimension is parallel to the direction of the jet flow. The dimension of the focal point is marked on a sensitive paper and measured by a microscope. The probe length as determined by the magnification ratio of collection optics (2.34) and the opening slit of spectrometer (100 μm) is 0.04 mm in the direction of beam propagation. Stokes Raman and fluorescence signals emanating from the sample volume are collected and focused by a Cassegrainian optics (magnification ratio 2.34) through a 10 mm thick butyl acetate liquid filter and relayed to the entrance slit of a 0.275 m, f/3.8 spectrometer (Acton Research, SpectraPro-275) with a 1200 grooves/mm grating (3 nm/mm dispersion) and a 0.5 m, f/4 spectrometer (SPEX-500M) with a 1800 grooves/mm grating (1.1 nm/mm dispersion) for dispersion and separate measurements. An intensified CCD camera (Princeton Instruments, 576×384 array, 22×22 μm pixels) is aligned at the exit plane of the spectrometer for monitoring

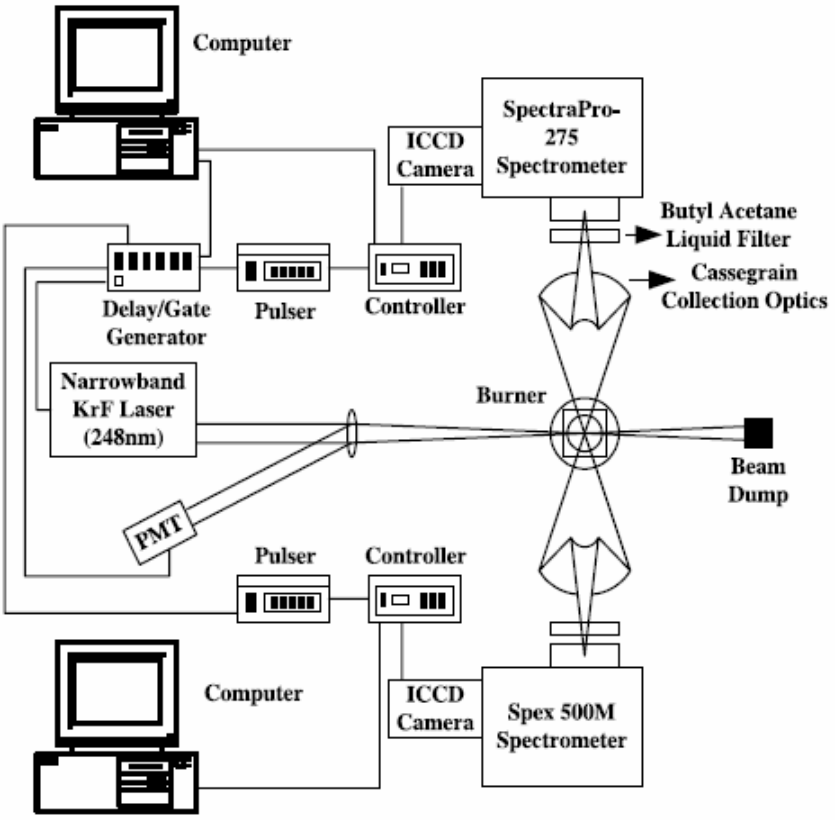

Fig. 1. Schematic diagram of UV Raman/LIPF system.

the Stokes Raman and fluorescence signals. The Raman and fluorescence signals are digitized with a 14-bit A/D card connected to a personal computer for data reduction. The spectral coverage of the 0.5 m spectrometer is 13.8 nm, which is used for the O_2 (258.4 nm) and N_2 (263.7 nm) Raman and O_2 fluorescence (267 nm) signal measurements. The spectral coverage of the 0.275 m spectrometer is 36.3 nm, which is used to measure H_2O (273.2 nm) and H_2 (277.1 nm) Raman signals as well as OH (297.5 nm) fluorescence in hydrogen flames. Both the 0.5 and 0.275 m spectrometers are aligned by placing a 100 μm wire at the center of the probe volume and centering the image onto the respective slits. This procedure ensures that Stokes Raman and fluorescence signals are measured from the same sample volume.

For hydrogen flame measurements, the Raman system is calibrated with the flat-flame "Hencken" burner operated at several known equivalence ratios from lean to rich. The calibration procedure for major species (N_2, O_2, H_2, and H_2O) and OH concentration measurements is similar to that described elsewhere [8,9]. The perfect gas law is used to arrive at the temperature measurement by adding the number densities of the major species. The experimental relative standard deviation for single-shot N_2 concentration measurements is 3% at room temperature and 7% in a stoichiometric flame at 2300 K. The relative standard deviation for temperature and OH concentration measurements is 9% and 19% in the stoichiometric flame, respectively. Typical single-shot relative standard deviations in this range are comparable to other UV Raman systems [10,11]. The well-calibrated Raman system is then capable of analyzing microscale hydrogen jet flames.

In addition, the qualitative 2-D OH imaging is also employed to visualize the flame structure [12]. For the OH imaging, the laser wavelength is tuned to 248.46 nm to excite the $P_2(8)$ rotational line of the A–X (3,0) transition. The laser beam is formed to a thin sheet of 34 mm height and 0.2 mm thick by a single cylindrical lens ($f = 1000$ mm) and intersected vertically through the flame axis. Only the 20 mm portion of the laser sheet, where the laser intensity is high and uniform, is used for imaging. The OH fluorescence signal is imaged onto an intensified CCD camera with a UV camera lens (Nikkor, $f = 105$ mm, f/4.5). A 10-mm-thick butyl acetate liquid filter is placed in front of the camera to reject the Rayleigh light.

3. Numerical simulations

To numerically model microscale hydrogen diffusion flames, the time-dependent ordinary sets

of conservation equations (mass, momentum, energy, and species) are solved with the finite volume method in a staggered grid system. Axisymmetric 2-D plane (r–x) is considered as the computational domain because of the axisymmetry of the jet. A schematic illustration of computational domain coupled with boundary conditions is shown in Fig. 2, which is similar to the one used in previous numerical studies [5–7]. Co-axial Poiseuille flow of the pure hydrogen fuel is ejected upward into a quiescent atmospheric air (101 kPa, 300 K, 21%/79% of oxygen/nitrogen mixture). As seen in the figure, the burner is placed inside the computational domain, and hence the property located inside as well as outside the burner is calculated. This takes into account the back-diffusion of species into the tube. Far-field boundary conditions are imposed to the open boundaries as shown in the figure. Non-slip, non-catalytic reaction, and constant temperature (300 K) conditions are applied on the burner surface. Normal gravity is considered as the external force. Burner specifications (inner/outer diameter, etc.) and volumetric flowrate for the corresponding burner are set to meet the current experiments. Detailed transport and multi-step reaction mechanisms including nine species (H_2, O_2, N_2, H_2O, H, O, OH, HO_2, and H_2O_2) and 21 reversible reactions for hydrogen–air mixture [13] are adopted for this study. Thermal properties for species are given by CHEMKIN database [14], while transport properties are determined by Smooke's simplified transport model [15]. Radiation heat loss from the H_2O is included based on the simplified optically thin model [16].

Central difference scheme is applied to the flux terms on the grid cell surface and the Euler implicit method is used for the time integration. In each time step, numerical iteration using the line-by-line successive over-relaxation (SOR) method is conducted. SIMPLE algorithm is employed for the pressure term in the Navier–Stokes equation [17]. Total number of meshes is 81 for the radial and 141 for axial direction. Entire region of the calculation is about 40d and 60d for the radial and axial direction, respectively. Stretched meshes are applied in both the directions; a minimal grid size of d/10 is placed near the burner and an enlarged grid size is set toward the outer boundaries. Calculation is started from an initial time step of 1.0×10^{-4} s and continuous until steady-state condition is reached. Solution in steady-state condition is checked by increasing the time step to show no dynamic response.

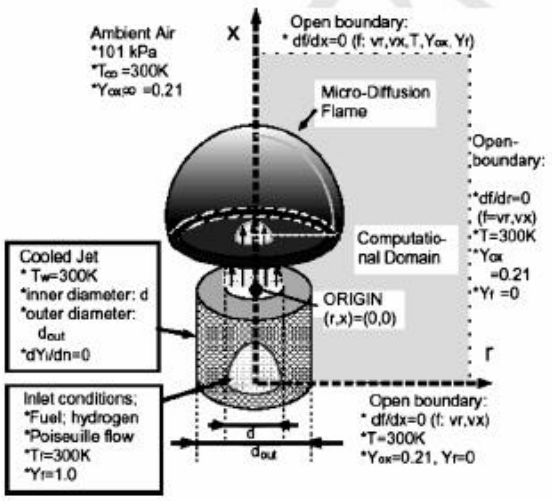

Fig. 2. Schematic illustration of numerical model.

4. Results and discussion

4.1. Flame visualization and OH imaging

Photographs and LIPF-OH images of the microscale hydrogen diffusion flames with tube diameters of 0.2 and 0.48 mm are shown in Fig. 3 for a fixed Reynolds number (Re = 30). Direct photographs are taken (using Sony color CCD camera with macrolens) with long exposure time due to weak luminosity from hydrogen flames. Photographs show that the microflames are egg-shaped and extend upstream of the burner port. The bright-yellow color of the burner port indicates significant heat loss from the flame to the burner. The measured burner port temperature, using an IR camera (Raytek MA2SC), is 943 and 1017 K for d = 0.2 and 0.48 mm flame, respectively. The qualitative single-pulse 2-D OH image corresponding to each flame is also shown in Fig. 3. Each image is taken at 0.1 mm above the burner port to reduce Mie scattering from the burner surface. Because the OH intensity reaches a maximum value in the flame front, the measured 2-D imaging of OH indicates the shape of the reaction zone. For the d = 0.48 mm flame, the shape of the OH imaging is quite similar to that observed by photograph. However, as the tube diameter is reduced to 0.2 mm, the reaction zone is spherical-shaped with a radius of about 1 mm, which is different from the photographic observation. This fact suggests that photographs may misinterpret the reaction zone, similar to conventional flames. A previous study with C_2 class of hydrocarbon fuels indicated that the flame is in convection–diffusion controlled regime as it is spherical-shaped [2]. Further analysis will be made to verify whether the flames studied here are in this regime once we proceed to discuss Raman results.

4.2. Thermophysical properties of the microflames

Simultaneous point measurements of temperature, major species (O_2, N_2, H_2O, and H_2), and OH concentrations are made in the radial direc-

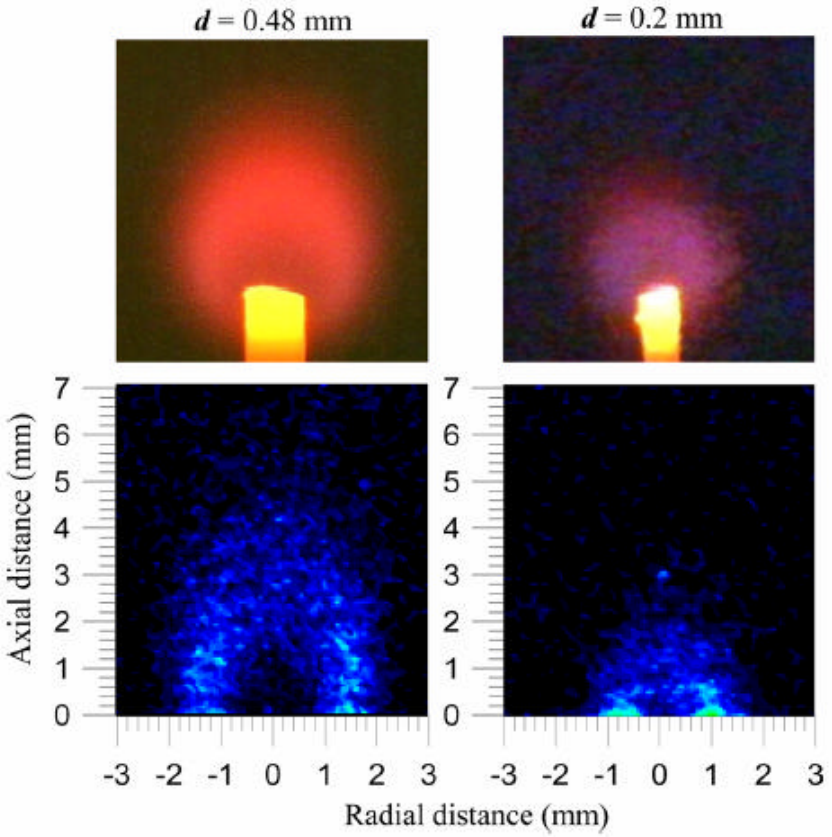

Fig. 3. Photographs and single-pulse LIPF-OH images of the microscale hydrogen diffusion flames with tube diameters of 0.2 and 0.48 mm.

tion at three axial locations (x = 0.1, 1, and 2 mm) of the microflames. At each measurement location, 200 independent Raman/LIPF-OH spectra are recorded and evaluated. For each single laser shot, the thermodynamic state properties are measured in the flame. Other quantities such as density and mixture fraction can be derived from the measured species concentrations. Figs. 4–6 show the comparison of measured radial profiles of the mean temperature, major species (O_2, N_2, H_2O, and H_2), and OH concentrations with the calculated results using detailed reaction mechanisms for the d = 0.2 mm flame. The measured mixture fractions (f) are also shown in the figures. The experimental data are indicated by symbols, and solid lines denote those from the simulation. Fig. 4 details the radial profile across the flame at x = 0.1 mm. The temperature rapidly rises from the center of the jet to 1786 K, where it decreases across the reaction zone and then has a sudden drop across the flame edge. The O_2 and N_2 appear at the center of the jet indicating leakage of ambient air into the flame. Recall that the microflame envelops the tube (Fig. 3) and could be quenched by the tube-wall, and consequently heating the burner port temperature up to 943 K. Therefore, a quenching gap may be produced between the flame and the wall surface. It has been reported that ambient air entrainment through this gap could modify the combustion status [18], and it has been experimentally observed in a mesoscale hydrogen diffusion flame (d = 1 mm, Re = 330)

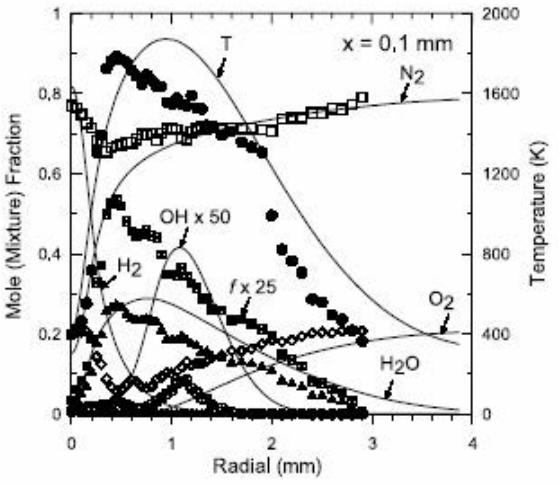

Fig. 4. Comparison of measured mean temperature, major species, and OH mole fraction with calculated radial profile for d = 0.2 mm flame at x = 0.1 mm. (•): T, (◇): O_2, (□): N_2, (▲): H_2O, (△): H_2, (⊕): OH × 50, (⊠): f × 25, and (—): calculation.

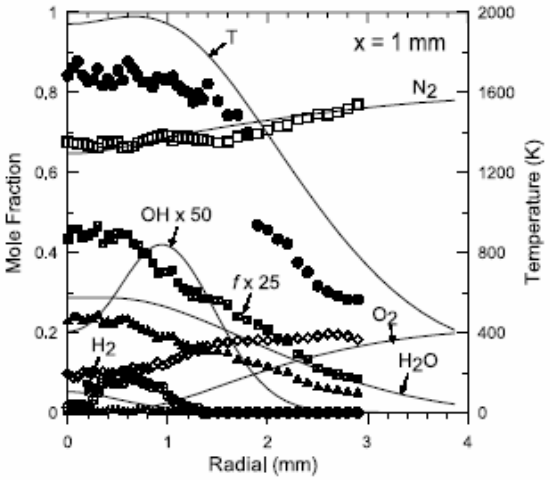

Fig. 5. Comparison of measured mean temperature, major species, and OH mole fraction with calculated radial profile for $d = 0.2$ mm flame at $x = 1$ mm. •: (T), ◇: O_2, (□): N_2, (▲): H_2O, (△): H_2, (⊕): OH × 50, (⊠): $f \times 25$, and (—): calculation.

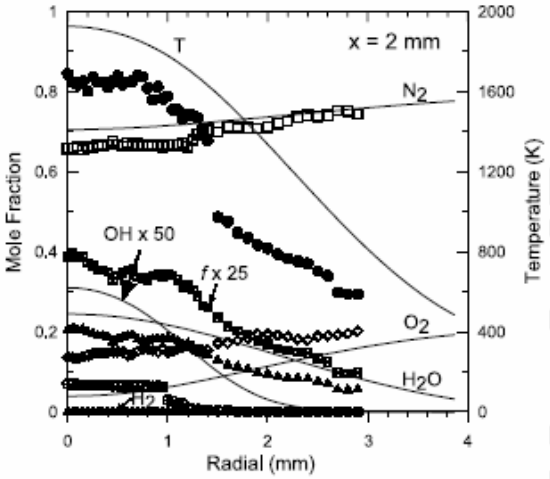

Fig. 6. Comparison of measured mean temperature, major species, and OH mole fraction with calculated radial profile for $d = 0.2$ mm flame at $x = 2$ mm. (•): T, (◇): O_2, (□): N_2, (▲): H_2O, (△): H_2, (⊕): OH × 50, (⊠): $f \times 25$, and (—): calculation.

[9]. Indeed, we found that the penetrated air has been heated up to 400 K, and no H_2O and H_2 are measured at the center of the jet. The disappearance of H_2 at the axial position near the burner exit in a microflame has never been reported for a normal laminar flame. We have examined the averaged (200 shoots) H_2 spectra across the radial direction at $x = 0.1$ mm and compared to those from the calibration burner in rich flame conditions. The maximum integrated H_2 intensity at the center of the jet is only comparable to the intensity corresponding to the equivalence ratio ranges of 1.05–1.2, which has a maximum equilibrium value of H_2 mole fraction of 0.065. The experimental uncertainties (15%, due to a small amount of H_2) may cause the measured mixture fraction to be slightly shifted to the lean side due to a large amount of O_2 and N_2 observed at the same location. The experimental uncertainty coupled with pre-heating enhanced thermal diffusion of H_2, and ambient air leakage could be the cause of no H_2 appearance around the center of the microflames. In addition, the calculated heat transfer rate from the tube to the hydrogen jet is 57 W, and the amount of heat required to raise the H_2 temperature to 400 K is 0.045 W. This means that most of the heat is dissipated by conduction through the tube, but not to initiate reaction at the nozzle outlet or inside the nozzle. Two OH peaks are found at the radial positions of $r = 0.45$ and 1.15 mm. This indicates that two reaction zones are formed at this downstream location in the flame. The flame structure measured at this axial location contradicts to a general concept that only one reaction zone exists in a laminar hydrogen diffusion flame. Comparisons between the predicted and measured data indicate that the trends of temperature, major species, and OH distributions are properly modeled. However, the code does not properly predict the air entrainment and hence results in an underprediction of O_2 and N_2 near the jet centerline. Moreover, the assumption of 300 K for the tube wall temperature, and the chemical kinetic mechanism as well as simplified transport model used in this simulation may lead to the overprediction of H_2 near the burner exit. We have tried heated surface condition and found that the discrepancy between experiment and simulation is remained. This could be due to the fact that kinetic and transport models used in the present study might be inadequate for the H_2 microflame simulation. Mosbacher et al. [19] have reported that flame curvature focusing could enhance H_2 diffusion, and the calculated flame structure is very sensitive to the chemical kinetic mechanism and molecular transport data. Therefore, thermal diffusion for light species and different combustion and transport models might need to be considered in the simulation of microflame structure.

Figs. 5 and 6 show the radial profiles for the flame at $x = 1$ and 2 mm, respectively. At these two axial locations, the temperatures distribute in a bell shape around the center of the jet and have a mean temperature of 1650 and 1600 K, respectively. The two OH peaks start to merge into one broad peak at $x = 1$ mm, indicating a transition of reaction zones at this axial position. Reaction occurred at the center of the jet resulting in an increase of H_2O and a decrease of O_2 and N_2. Comparisons of the predicted and measured data at these two axial locations also indicate that the model properly predicts the trends of temperature, major species, and OH distributions. How-

ever, the higher prediction of temperature results in an overprediction of H_2O and OH and underprediction of O_2 and N_2.

As the tube diameter is increased to 0.48 mm, comparisons of measured radial profiles of the mean temperature, major species (O_2, N_2, H_2O, and H_2), and OH concentrations with the calculated results are shown in Figs. 7–9 for $x = 0.1$, 1, and 2 mm, respectively. The distributions of temperature and species concentrations measured in this flame are similar to those observed in $d = 0.2$ mm flame at the same axial position except that the flame is larger. At $x = 0.1$ mm, the mean temperatures at the jet centerline ($T = 784$ K) and within the reaction zone ($T = 1780$ K) are higher than those of the $d = 0.2$ mm flame. The higher centerline temperature indicates significant heat loss from the flame to the entrained ambient air and the tube. The calculated heat transfer rate from the tube to the hydrogen jet is 111 W, and the amount of heat required to raise H_2 temperature to 784 K is 0.543 W. Again, most of the heat is dissipated by conduction through the tube, not to initiate reaction at the nozzle outlet. Preheating of the entrained ambient air results in higher flame temperature and OH concentration. The OH distribution also indicates two reaction zones existing at this downstream position (Fig. 7). Overall comparisons between the predicted and measured data also reveal that the model predicts a broader flame and much higher temperature as well as OH concentration.

Several important features are identified from the detailed measurements of microflames. The coupled effect of air entrainment and disappearance of H_2 near the jet exit leads to lean-burn conditions for the flame (mixture fraction less than 0.0283). Moreover, the flame extends upstream of the burner port, suggesting that molecular diffusive-transport would dominate over the buoyant effect. A simple calculation, as suggested by Ban et al. [2], is performed to verify whether the flames studied here are convection–diffusion or buoyancy controlled. Ban et al. reported that the spherical flame occurs when the ratio of the mean exit velocity, u_e (flowrate/burner port area), to the diffusion velocity, $u_D = D/l_D$ (D is the mass-diffusion coefficient, and l_D is a characteristic diffusion length in the flame), is less than 5 ($Pe = u_e/u_D = u_e l_D/D$) for the C_2 class hydrocarbon fuel.

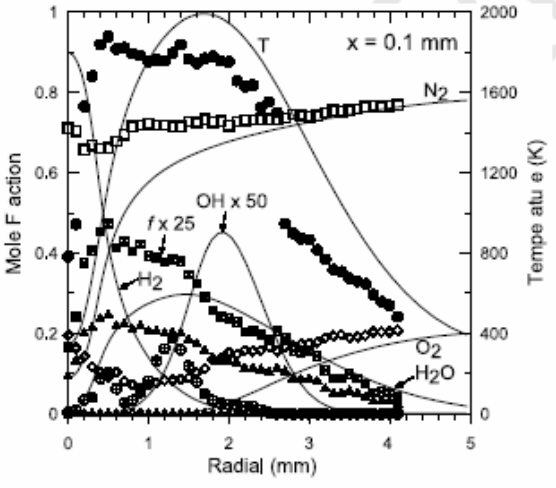

Fig. 7. Comparison of measured mean temperature, major species, and OH mole fraction with calculated radial profile for $d = 0.48$ mm flame at $x = 0.1$ mm. (•): T, (◇): O_2, (□): N_2, (▲): H_2O, (△): H_2, (⊕): OH × 50, (⊠): $f \times 25$, and (—): calculation.

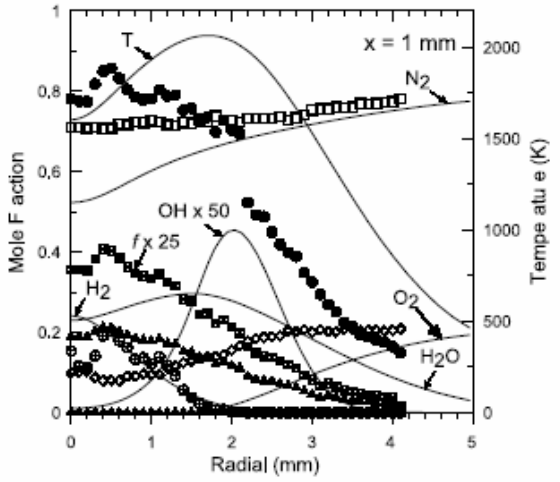

Fig. 8. Comparison of measured mean temperature, major species, and OH mole fraction with calculated radial profile for $d = 0.48$ mm flame at $x = 1$ mm. (•): T, (◇): O_2, (□): N_2, (▲): H_2O, (△): H_2, (⊕): OH × 50, (⊠): $f \times 25$, and (—): calculation.

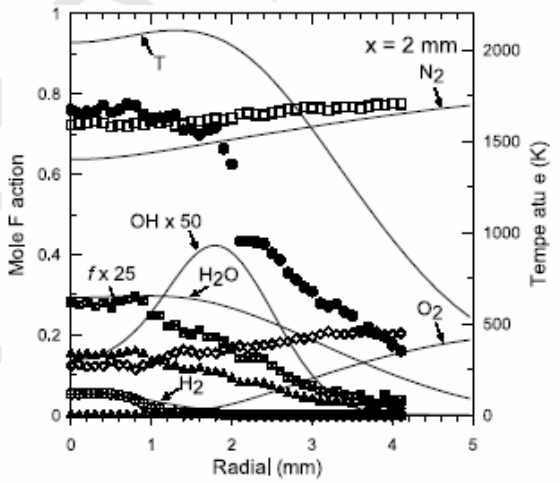

Fig. 9. Comparison of measured mean temperature, major species, and OH mole fraction with calculated radial profile for $d = 0.48$ mm flame at $x = 2$ mm. (•): T, (◇): O_2, (□): N_2, (▲): H_2O, (△): H_2, (⊕): OH × 50, (⊠): $f \times 25$, and (—): calculation.

Table 1
Summary of calculated flame characteristics and properties

Burner diameter (mm)	0.20	0.48
u_e (m/s)	16.48	7.16
Re	30	30
Fr	1.39×10^{5}	1.09×10^{4}
T_{mea} (K)	1786	1879
l_D (m)	2.6×10^{-4}	9×10^{-5}
D (m^2/s)	6.02×10^{-4}	6.49×10^{-4}
u_D (m/s)	2.32	7.21
t_D (s)	1.12×10^{-4}	1.25×10^{-5}
Pe	7	1

For the present hydrogen flames, l_D is defined as the characteristic diffusion length from the inner tube wall to the first OH peak from the jet centerline at $x = 0.1$ mm (Figs. 4 and 7). The characteristic diffusion time, t_D, is the ratio of l_D to u_D. The calculated characteristic features and properties are summarized in Table 1. The calculated results indicate that the buoyancy effect is insignificant compared to the momentum of jet, due to large Fr in these flames. Also, the flames are convection–diffusion controlled because of low Peclet number. It is noted that the value of Pe for the spherical flame ($d = 0.2$ mm) is seven times larger than that of an egg-shaped flame ($d = 0.48$ mm). This fact suggests that the effect of Pe on the flame shape is insignificant as the flame is in the convection–diffusion controlled regime.

5. Conclusions

Characteristics of microscale hydrogen diffusion flames produced from sub-millimeter diameter ($d = 0.2$ and 0.48 mm) tubes are investigated using non-intrusive UV Raman scattering coupled with LIPF technique. Simultaneous, temporally and spatially resolved point measurements of temperature, major species concentrations (O_2, N_2, H_2O, and H_2), and absolute hydroxyl radical concentration (OH) are made in the microflames for the first time. In addition, photographs and 2-D OH imaging techniques are employed to illustrate the flame shapes and reaction zones. Photographs show that both flames are egg-shaped. However, qualitative 2-D OH imaging indicates that a spherical flame is formed with a radius of about 1 mm as the tube diameter is reduced to 0.2 mm. Raman/LIPF measurements show that ambient air leaks into the flames, and no H_2 molecules are detected at $x = 0.1$ mm. The coupled effect of ambient air leakage and pre-heating enhanced thermal diffusion of H_2 leads to lean-burn conditions for the flame. Farther downstream ($x = 1$ and 2 mm), the temperature profiles become bell-shaped. The calculated characteristic features and properties indicate that the buoyancy effect is insignificant while the flames are in the convection–diffusion controlled regime because of low Peclet numbers. Also, the effect of Pe on the flame shape is insignificant as the flame is in the convection–diffusion controlled regime. Comparisons between the predicted and measured data indicate that the trends of temperature, major species, and OH distributions are properly modeled. However, the code does not properly predict the air entrainment and pre-heating enhanced thermal-diffusive effects. The inability of the numerical simulations to correctly predict flame structure in diffusion H_2 microflames, where air entrainment and thermal-diffusive effects are dominant, suggests that a more detailed investigation of the chemical kinetic mechanism and molecular transport data is warranted.

Acknowledgments

This research was supported by the National Science Council of the Republic of China under Grant Nos. NSC92-2212-E-216-001 (TSC), NSC92-2212-E-006-004 (YCC), and by the Kurata Memorial Hitachi Science and Technology Foundation (YN). The financial supports are gratefully acknowledged.

References

[1] G.T.A. Kovacs, *Micromachined Transducers-Source Book*, McGraw-Hill, New York, 1998.
[2] H. Ban, S. Venkatesh, K. Saito, *J. Heat Transfer* 116 (1994) 954–959.
[3] T. Ida, M. Fuchihata, Y. Mizutani, in: *Microscopic Diffusion Structures with Micro Flames. Proceedings of the third International Symposium on Scale Modeling*, ISSM3-E3, 2000.
[4] L.M. Matta, Y. Neumeier, B. Lemon, B.T. Zinn, *Proc. Combust. Inst.* 29 (2002) 933–939.
[5] Y. Nakamura, H. Ban, K. Saito, T. Takeno, in: *Structures of Micro (Millimeter Size) Diffusion Flames. Proceedings of the third International Symposium on Scale Modeling*, ISSM3-E7, 2000.
[6] Y. Nakamura, A. Kubota, H. Yamashita, K. Saito, in: *Numerical Study on Methane Micro-Diffusion Flames. Proceedings of the 19th International Colloquium on the Dynamics of Explosion and Reactive Systems*, Paper No. We2-2-1(#105), 2003.
[7] Y. Nakamura, A. Kubota, H. Yamashita, K. Saito, in: *Near Extinction Flame Structure of Micro-Diffusion Flames. Proceedings of the International Symposium on Micro-Mechanical Engineering*, ISMME2003-11, 2003.
[8] T.S. Cheng, J.A. Wehrmeyer, R.W. Pitz, *Combust. Flame* 91 (3/4) (1992) 323–345.
[9] T.S. Cheng, Y.-C. Chao, C.-Y. Wu, G.-B. Chen, T. Yuan, T.S. Leu, in: *Experimental and Numerical Study of a Laminar Nonpremixed Hydrogen Flame. Proceedings of the 19th International Colloquium on*

the Dynamics of Explosion and Reactive Systems, Paper No. We1-1-4(#27), 2003.

[10] S.P. Nandula, T.M. Brown, P.A. Skaggs, R.W. Pitz, P.A. DeBarber, in: *Multi-Species Line Raman Measurements in H_2–Air Turbulent Flames, AIAA 32nd Aerospace Science Meeting*, AIAA Paper No. 94-0227, 1994.

[11] Y.-C. Chen, M.S. Mansour, *Proc. Combust. Inst.* 26 (1996) 97–103.

[12] T.S. Cheng, Y.-C. Chao, D.-C. Wu, T. Yuan, C.-C. Lu, C.-K. Cheng, J.-M. Chang, *Proc. Combust. Inst.* 27 (1998) 1229–1237.

[13] E. Gutheil, G. Balakrishnan, F.A. Williams, in: N. Peters, B. Rogg (Eds.), *Reduced Kinetics Mechanisms for Applications in Combustion System*, Springer-Verlag, New York, 1993, pp. 177–195.

[14] R.J. Kee, F.M. Rupley, A.J. Miller, *The C HEMKIN Thermodynamic Database*, Report No. SAND87-8215, Sandia National Laboratories, 1987.

[15] M. D. Smooke, in: *Reduced Kinetic Mechanisms and Asymptotic Approximations for Methane–Air Flames*, Lecture Notes in Physics, vol. 384, Springer-Verlag, New York, 1991, pp. 1–28.

[16] Available from: <http://www.ca.sandia.gov/TNF/radiation.html>.

[17] S.V. Patankar, *Numerical Heat Transfer and Fluid Flow*, McGraw-Hill, New York, 1980.

[18] K. Saito, A.S. Gordon, F.A. Williams, *Combust. Sci. Technol.* 47 (1986) 117–138.

[19] D.M. Mosbacher, J.A. Wehrmeyer, R.W. Pitz, C.-J. Sung, J.L. Byrd, *Proc. Combust. Inst.* 29 (2002) 1479–1486.